Atomic structure of capped In(Ga)As and GaAs quantum dots for optoelectronic devices

vorgelegt von
Diplom-Physikerin
Andrea Lenz
aus Kappeln

Von der Fakultät II – Mathematik und Naturwissenschaften
der Technischen Universität Berlin
zur Erlangung des akademischen Grades

Doktorin der Naturwissenschaften
- Dr. rer. nat. -
genehmigte Dissertation

Promotionsausschuss:

Vorsitzender: Prof. Dr. Erwin Sedlmayr
Berichter: Prof. Dr. Mario Dähne
Berichter: Prof. Dr. Dieter Bimberg

Tag der wissenschaftlichen Aussprache: 11. Februar 2008

Berlin 2008
D 83

Abstract

Devices based on In(Ga)As/GaAs and GaAs/AlGaAs quantum dots are promising for various applications in optoelectronics, such as low threshold lasers at emission wavelengths of about 1.3 μm. In this work, cross-sectional scanning tunneling microscopy (XSTM) is used to investigate the atomic structure of buried In(Ga)As and GaAs quantum dots grown by several groups using different growth techniques. In particular the influence of the overgrowth process is studied, which is required for applications in devices.

The results of a detailed XSTM investigation on capped InAs/GaAs quantum dots are compared with existing top-view STM results of uncapped quantum dots. Since both samples were grown in the same chamber and under identical growth conditions, this comparison offers a unique possibility to analyze the influence of the overgrowth process, observing considerable changes of the atomic structure and stoichiometry. It is found that the formerly pyramidal quantum dots, mainly characterized by {137} side facets, are modified during capping. The large lattice mismatch between the InAs material of the quantum dot apex and the GaAs capping material results in strong segregation effects leading to a truncation of the quantum dots together with a steepening of their side facets. In addition, the probably pure uncapped InAs quantum dots become intermixed, and also for the wetting layer strong segregation effects are observed.

Several strategies to reach luminescence at 1.3 μm were studied, such as to offer Sb during InAs growth, the overgrowth of InGaAs quantum dots with a strain-reducing InGaAs layer, or the growth of InAs quantum dots embedded within InGaAs quantum wells. Antimony supply during the quantum dot growth prevents segregation, although no antimony incorporation is observed at the quantum dots, but only at the wetting layer. This leads to an increase of the quantum dot size and the average indium content and therewith to the desired longer emission wavelengths. In the two cases using InGaAs layers an increased quantum dot size was observed as well, but also defective quantum dots are found, characterized by a material hole or so-called nanovoid. The mechanisms of the nanovoid formation depends on details of the growth sequence, but occurs in each case during the capping process due to the large local strain. Nanovoid formation thus represents an important limit of larger quantum dot growth.

Finally hierarchically grown unstrained GaAs/AlGaAs quantum dots are examined. In this first XSTM investigation a decomposition of the AlGaAs layers and a variation of the GaAs quantum well thickness is observed. Additionally the expected quantum dot height is confirmed, while their lateral size is found to be smaller, providing an incentive to further investigations.

In summary, this work presents a detailed investigation on the atomic scale of the strain-induced segregation processes occurring during the different stages of In(Ga)As quantum dot growth and overgrowth.

Zusammenfassung

Bauelemente basierend auf In(Ga)As/GaAs- und GaAs/AlGaAs-Quantenpunkten sind vielversprechend für eine Vielzahl von optoelektronischen Anwendungen, wie Laser mit niedrigen Schwellströmen und Wellenlängen um 1.3 μm. In dieser Arbeit wird Rastertunnelmikroskopie an Querschnittsflächen (XSTM) dazu benutzt, die atomare Struktur von vergrabenen In(Ga)As/GaAs- und GaAs/AlGaAs-Quantenpunkten zu untersuchen, die von verschiedenen Gruppen mit unterschiedlichen Wachstumsmethoden hergestellt wurden. Dabei wurde besonders der Einfluss des Überwachsens untersucht, das notwendig für die Anwendung in Bauelementen ist.

Die Ergebnisse einer detaillierten XSTM-Untersuchung von InAs/GaAs-Quantenpunkten werden mit bereits bestehenden STM Ergebnissen verglichen. Da beide Proben mit derselben Apparatur und unter identischen Wachstumsbedingungen hergestellt wurden, bietet dieser Vergleich eine einmalige Möglichkeit den Einfluss des Überwachsens zu untersuchen, wobei beträchtliche Veränderungen der atomaren Struktur und der Stöchiometrie beobachtet werden. Es wird herausgefunden, dass ehemals pyramidale Quantenpunkte, die sich durch {137}-Seitenfacetten auszeichnen, sich während des Überwachsens verändern. Aus der großen Gitterfehlanpassung zwischen der aus InAs bestehenden Quantenpunktspitze und der GaAs-Deckschicht resultiert ein starker Segregationseffekt, der zu einer Abflachung der Quantenpunkte und zu steileren Seitenflächen führt. Außerdem durchmischt der unbedeckt vermutlich reine InAs-Quantenpunkt, und auch für die Benetzungsschicht werden starke Segregationsprozesse beobachtet.

Verschiedene Methoden, um Lumineszenz bei 1.3 μm zu erreichen, sind z.B. die Zugabe von Antimon während des InAs-Wachstums, dem Überwachsen von InGaAs-Quantenpunkten mit verspannungsreduzierenden InGaAs-Schichten oder das Wachstum von InAs-Quantenpunkten in InGaAs-Schichten. Die Beigabe von Antimon während des Quantenpunktwachstums verhindert Segregation, obwohl ein Einbau von Antimon nur in die Benetzungsschicht und nicht in die Quantenpunkte beobachtet wird. Dies führt zu einem Anstieg der Quantenpunktgröße und des mittleren Indium-Gehaltes und damit zu der erwünschten längeren Wellenlänge. In den beiden Fällen, in denen InGaAs-Schichten verwendet werden, wird ebenfalls ein Anstieg der Quantenpunktgröße beobachtet, allerdings auch Quantenpunkte mit Defekten in Form eines Hohlraumes, der als Nanovoid bezeichnet wird. Die Bildung der Nanovoids hängt dabei von den jeweiligen Wachstumsschritten ab, tritt aber jeweils während des Überwachsens aufgrund der hohen lokalen Verspannung auf. Die Entstehung von Nanovoids stellt deshalb eine wichtige Grenze des Wachstums großer Quantenpunkte dar.

Abschließend wurden noch stufenweise prozessierte unverspannte GaAs/AlGaAs-Quantenpunkte untersucht. Bei dieser ersten XSTM Untersuchung konnte eine Entmischung der AlGaAs-Schicht und eine variierende Schichtdicke des GaAs-Quantengrabens beobachtet werden. Zusätzlich bestätigt sich die erwartete Quantenpunkthöhe, während eine kleinere laterale Ausdehnung gefunden wurde, die einen Anreiz für weitere Untersuchungen liefert.

Zusammenfassend wird in dieser Arbeit eine detaillierte atomare Untersuchung der verspannungsinduzierten Segregationsprozesse präsentiert, die während der verschiedenen Stadien des In(Ga)As-Quantenpunktewachstums und des Überwachsens auftreten.

Parts of this work have been published in

- *Structure of InAs quantum dots-in-a-well nanostructures,*
  A. Lenz, H. Eisele, R. Timm, L. Ivanova, H.-Y. Liu, M. Hopkinson, U. W. Pohl, and M. Dähne, Physica E, accepted (2007).

- *Structure of InAs/GaAs quantum dots grown with Sb surfactant,*
  R. Timm, H. Eisele, A. Lenz, T.-Y. Kim, F. Streicher, K. Pötschke, U. W. Pohl, D. Bimberg, and M. Dähne, Physica E **32**, 25 (2006).

- *Structural investigation of hierarchically self-assembled GaAs/AlGaAs quantum dots,*
  A. Lenz, R. Timm, H. Eisele, L. Ivanova, D. Martin, V. Voßebürger, A. Rastelli, O. G. Schmidt, and M. Dähne, phys. stat. sol. (b) **243**, 3976 (2006).

- *Nanovoids in InGaAs/GaAs quantum dots observed by cross-sectional scanning tunneling microscopy,*
  A. Lenz, H. Eisele, R. Timm, S. K. Becker, R. L. Sellin, U. W. Pohl, D. Bimberg, and M. Dähne, Appl. Phys. Lett. **85**, 3848 (2004).

- *Segregation effects during GaAs overgrowth of InAs and InGaAs quantum dots studied by cross-sectional scanning tunneling microscopy,*
  H. Eisele, R. Timm, A. Lenz, Ch. Hennig, M. Ternes, S. K. Becker, and M. Dähne, phys. stat. sol. (c) **0**, 1129 (2003).

- *Atomic structure of InAs and InGaAs quantum dots studied by cross-sectional scanning tunneling microscopy,*
  H. Eisele, A. Lenz, R. Timm, Ch. Hennig, M. Ternes, F. Heinrichsdorff, A. Krost, R. Sellin, U. W. Pohl, D. Bimberg, T. Wehnert, E. Steimetz, W. Richter, and M. Dähne, Inst. Phys. Conf. Series **171**, P199 (2003).

- *Atomic structure of InAs and InGaAs quantum dots determined by cross-sectional scanning tunneling microscopy,*
  H. Eisele, A. Lenz, Ch. Hennig, R. Timm, M. Ternes, and M. Dähne, J. Crystal Growth **248**, 322 (2003).

- *Reversed truncated cone composition distribution of $In_{0.8}Ga_{0.2}As$ quantum dots overgrown by an $In_{0.1}Ga_{0.9}As$ layer in a GaAs matrix,*
  A. Lenz, R. Timm, H. Eisele, Ch. Hennig, S. K. Becker, R. L. Sellin, U. W. Pohl, D. Bimberg, and M. Dähne, Appl. Phys. Lett. **81**, 5150 (2002).

Contents

Chapter 1

Introduction

Optoelectronic devices are nowadays used in everyday life e.g. in several computer components, in traffic light systems, photovoltaic systems, or in the wide field of telecommunication, where signals are transmitted over large distances in optical fibers. Such devices, as light detectors, solarcells, light emitting diodes (LEDs), or semiconductor lasers [1, 2], are based on electronic components interacting with light of various wavelengths.

The development of semiconductor lasers as one field of optoelectronics starts at the beginning of the 20^{th} century with the theory of A. Einstein on the stimulated emission of light [3]. First steps of realization followed by Ch. Townes in 1954 with the development of a laser working in the microwave regime [4], and 1960 by T. H. Maiman with the construction of a ruby crystal laser with emission in the visible spectral range [5]. Shortly after experimental studies on LEDs, the first semiconductor laser based on GaAs in 1962 followed [6–8].

The progress in the telecommunication industry later lead to optical fibers with an optimized design to guide light of wavelengths between 1.3 and 1.55 μm, since the silicate based fibers have a dispersion minimum at 1.3 μm and an absorption minimum at 1.55 μm. Consequently laser structures emitting at this spectral range became very important, in order to act as an amplifier or repeater. A fundamental step towards low threshold semiconductor laser structures emitting in this wavelength regime was the discovery of the growth of self-organized three-dimensional nanostructures in 1985, which were later called quantum dots [9]. The advantages of self-organized quantum dot growth are the distinctive size and shape uniformity as well as a low defect density, leading to a narrow spectral range and therewith to an high optical quality of the arising device.

A very simple illustration of the quantum dot size and its special electronic behavior is shown in Fig. 1.1. The length reduction factors from the Kiel bay via a sail boat to a compass needle are comparable to the decrease from a volume semiconductor via a waveguide to a quantum dot with nanometer size. Consequently the quantum dot dimension is in the order of the de Broglie wavelength of the electrons and thus quantum mechanical effects become more relevant.

One important property of nanostructures is the change of the electronic density of states with the spatial dimension. It changes from square root like for the volume semiconductor towards discrete energies with delta-like shape for quantum dots (red box in

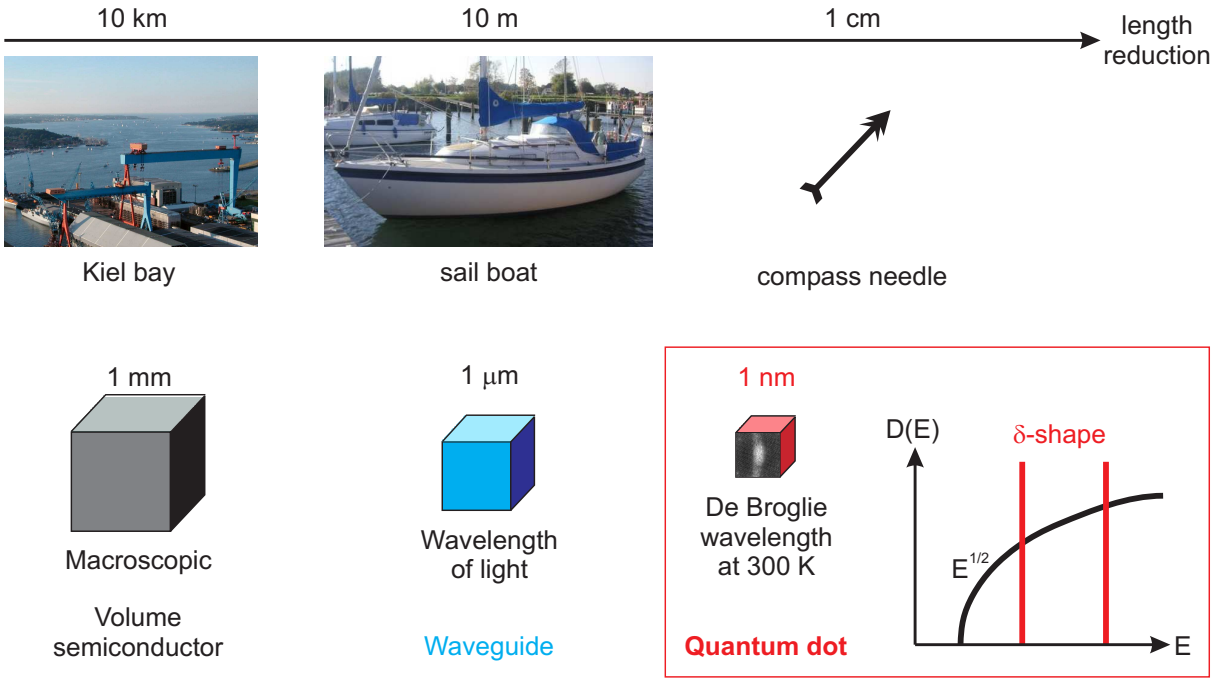

FIGURE 1.1: Scaling factors in nautics (above) and semiconductors (below). In the red box the electronic density of states with a $E^{1/2}$ dependence of the volume semiconductor and discrete energies with delta-like shape for quantum dots are compared. Photos taken from Refs. [10, 11].

Fig. 1.1). These size quantization effects were investigated over several years [12–14], and especially for semiconductor laser structures quantum dots have raised high importance in the last 15 years, leading to further developments in optoelectronics [1, 2, 15–20].

After these initial years of research the commercial production of quantum dot lasers is now at its beginning [21]. Thus reproducible growth becomes even more important, so that the understanding of the growth and overgrowth processes has to be further improved. Theoretical calculations of the electronic and optical properties [22] are always based on structural parameters, so consequently the characterization of size, shape, and stoichiometry of the nanostructures are of high importance. It was found that only little changes in the size or composition of the quantum dots may lead to significant changes in their optical behavior [23–25].

The main structural characterization methods of quantum dot laser structures are atomic force microscopy, transmission electron microscopy and scanning tunneling microscopy (STM). The latter one can easily achieve atomic resolution. Figure 1.2 shows the main difference between top-view or plane-view STM and cross-sectional STM (XSTM), which is used in this work. In the top-view STM experiment the uncapped quantum dot structure can be examined on the growth surface, while in the XSTM experiment the sample is cleaved and thus the capped quantum dot structures can be studied. Such an investigation of the buried nanostructures is of high importance, since all optoelectronic quantum dot devices are capped and furthermore it turned out in the last years that during capping quantum dot size, shape and stoichiometry may change considerably [26–30].

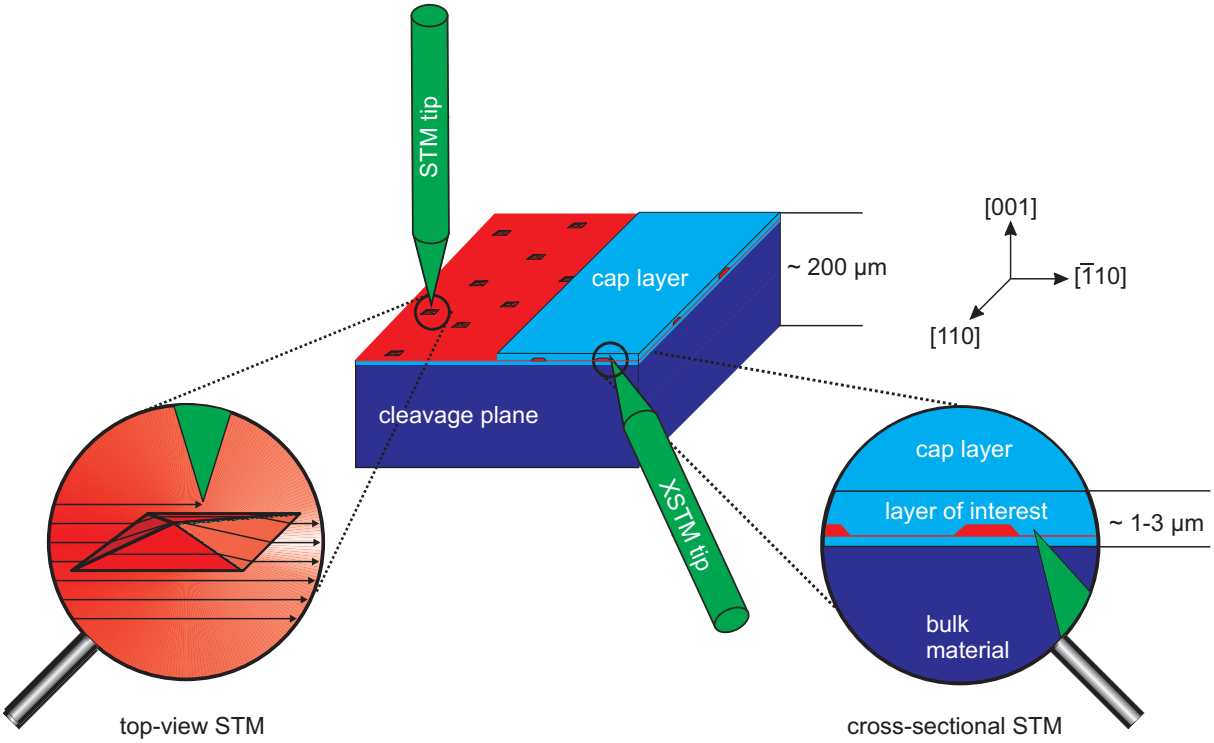

FIGURE 1.2: Top-view and cross-sectional scanning tunneling microscopy.

In this work the influence of the overgrowth process on the resulting buried nanostructures is investigated on an atomic scale for a variety of In(Ga)As and GaAs quantum dot samples provided by several groups. This includes the examination of samples already studied using top-view STM and of samples grown for the important wavelength of 1.3 μm.

After an introduction to the general growth methods (chapter 2) and the characterization methods used in this work (chapter 3), the description of the experimental setup and the later on used data analysis follows (chapter 4). The results of different quantum dot samples will then be presented in chapters 5−8.

Chapter 5 focuses on a direct investigation of the changes during overgrowth. Therefore InAs/GaAs quantum dots are investigated with cross-sectional STM and compared with existing top-view STM results on identically grown samples. From the comparison of the uncapped and capped quantum dots an atomistic overgrowth model is developed, taking the structural and stoichiometric changes during capping into account.

In chapter 6 and 7 quantum dots grown as laser devices with emission wavelengths up to 1.3 μm are examined. In order to reach this wavelength large quantum dots are required, which are grown using different growth strategies. One possibility is to offer antimony during the quantum dot growth. In chapter 6 the results on InAs/GaAs quantum dots grown with antimony supply during different growth stages are presented and its influence on the quantum dot size and stoichiometry is analyzed. In chapter 7 growth methods based on strain-reducing InGaAs layers for larger quantum dots are investigated. In addition to an increase in the emission wavelength due to larger quantum dot sizes, also defects

in the quantum dots are observed, reducing the optical quality of the samples. These observations are discussed in the framework of growth models considering strain-induced segregation during quantum dot growth and overgrowth.

Furthermore, initial investigations on unstrained GaAs/AlGaAs quantum dots are presented in chapter 8. These quantum dots are designed to emit light within the visible spectral range, and recently performed optical investigations show promising narrow linewidths, indicating a high quantum dot homogeneity [31–33].

The influences of specific sample parameters such as the amount of quantum dot material, the use of strain-reducing layers, or the introduction of growth interruptions during capping on the resulting sample structure will be summarized in chapter 9.

Chapter 2

Growth of III-V semiconductor quantum dots

Semiconductor quantum dots can be obtained either by lithography and etching processes [16, 34–37] or using a self-organized growth [1, 18]. Since etching processes induce defects, they lead to a low quantum efficiency and thus to a high threshold current density. In contrast, the advantages of self-organized quantum dot growth are the possibility of size and shape uniformity, the high quantum dot density, and the low defect density, all leading to a high optical quality. The mostly utilized growth techniques for self-organized quantum dots are vapor phase epitaxy (VPE) and molecular beam epitaxy (MBE). For VPE of III-V quantum dots a special modification is used, called metal-organic chemical vapor phase epitaxy (MOVPE) or metal-organic chemical vapor deposition (MOCVD). The latter abbreviation will be used in the following. Several variations of these basic techniques have been developed for specific needs. The samples investigated in this work were grown using MBE and MOCVD. Therefore this chapter gives an introduction to the principal growth mechanisms of these techniques, in reference to the samples investigated later on. For additional information about different growth techniques see e.g. Refs. [38, 39].

2.1 Growth techniques

Quantum dots are called self-organized, if they form during epitaxial growth without any external support. The growth of these three-dimensional structures occurs due to the minimization of the strain and surface energies of the system [40]. In the case of thin film growth one generally distinguishes between three growth modes depending on surface, interface, and film energies. The layer by layer growth mode is called Frank-van der Merwe [41], the Volmer-Weber mode is characterized by island growth without a wetting layer [42], and the Stranski-Krastanow (SK) mode is a combination of both mechanisms [43, 44].

In the SK mode growth initially occurs layer by layer, but with increasing layer thickness also the film energy increases, e.g. the strain energy in case of a lattice mismatch. The system can lower the strain energy by a faceting of the growth surface, leading to

the formation of islands and thus to a strain relaxation [45]. However, a larger surface is created due to the three-dimensional (3D) island growth, leading to an increases of the surface energy. Consequently the SK growth mode occurs due to a balance between strain and surface energy [46].

In the InAs/GaAs system the SK mode leads to quantum dot growth. The first 1−1.5 monolayer (ML) InAs are grown as a two-dimensional (2D) wetting layer, then the morphology of the growth surface changes abruptly, and at a coverage of about 1.6−1.7 ML InAs islands are formed [17, 47]. The strain-induced SK growth mode is caused by the large lattice mismatch between the substrate and the deposited material, amounting to about 7% for InAs on GaAs. Due to this lattice mismatch the elastic energy of the system increases upon formation of a pseudomorphic film, meaning that the deposited material matches the substrate. When this deformation energy becomes too high it relieves e.g. in a misfit dislocation or in 3D island growth. These 3D islands may include undesirable dislocations, but under appropriate growth conditions they are dislocation-free (coherent). If the 3D islands forming during SK mode are coherent, with sizes below the de Broglie wavelength of the electrons, and embedded in a material with a higher bulk bandgap, as it is the case for the InAs/GaAs system, they are called quantum dots.

The transition of an epitaxial flat surface to three-dimensional island evolution can be controlled during the growth e.g. by reflection high-energy electron diffraction (RHEED) or reflectance anisotropy spectroscopy (RAS). With these methods, also the film thicknesses can be determined with an accuracy of about one monolayer.

The main difference between the MOVPE and MBE growth technique is the precursor state of the deposited material. A sketch of both processes is shown in Fig. 2.1. In MBE

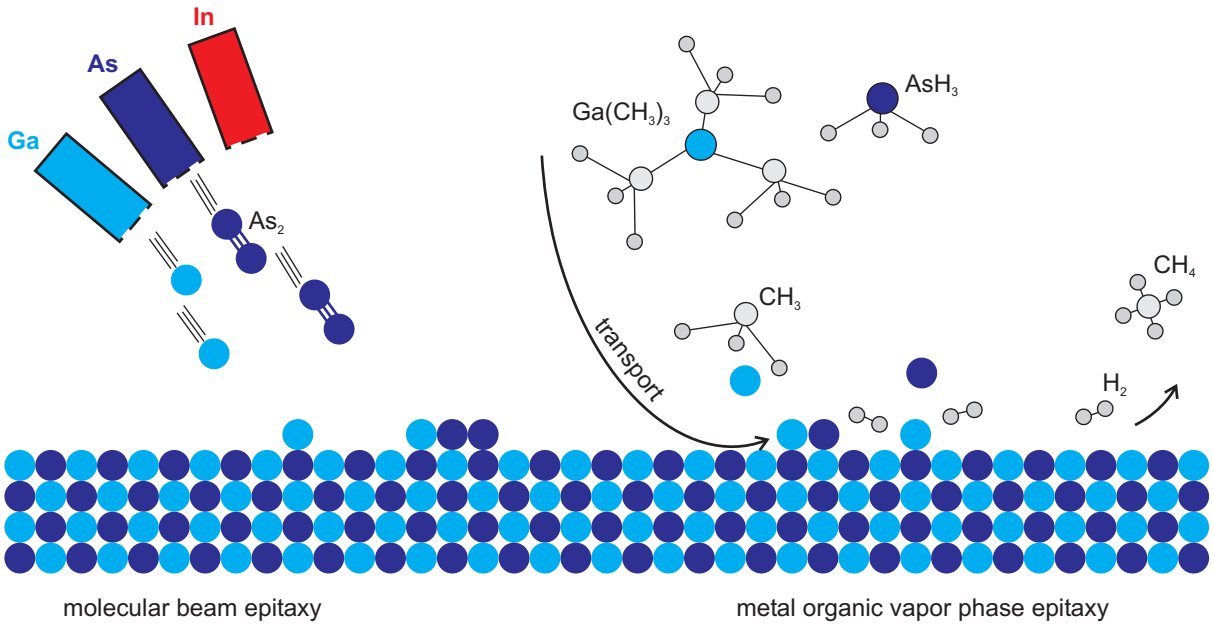

FIGURE 2.1: Comparison of the MBE and MOVPE growth process.

the atomic or molecular beams are created by evaporation from solid sources, and the impinging beam fluxes react with the atomic layers of the substrate. In MOVPE the atoms are introduced as part of organic compounds within a carrier gas such as H_2 or N_2 flowing over the heated substrate, where gas phase reactions and reactions at the gas-solid interface take place, leading to epitaxial growth of the semiconductor layers. In the special case of InAs/GaAs quantum dot growth, precursors such as trimethylgallium, trimethylindium, arsin or tertiarybutylarsine are typically used.

2.1.1 Molecular beam epitaxy

The molecular beams of a solid source MBE are generated in so-called Knudsen effusion-cells. By choosing appropriate cell and substrate temperatures, epitaxial layers of the desired chemical composition may be obtained with typical growth rates up to 1 ML s^{-1}, corresponding to about 1 μm h^{-1}. Often the substrate is rotated in order to reduce growth rate variations across the sample due to the asymmetric arrangement of the effusion cells.

On the way to the rotating and heated substrate the molecular beams intersect each other, but due to the long mean free path of the molecules no interactions between the different species occur before reaching the heated substrate. Afterwards epitaxial growth is realized on the substrate surface, as shown schematically in Fig. 2.2. The most important surface processes involved in MBE growth are the following:

- Adsorption of the atoms or molecules impinging on the substrate surface
- Surface diffusion and dissociation of the adsorbed atoms, as well as interdiffusion of already incorporated atoms
- Incorporation of the atoms into the crystal lattice at the growth surface
- Thermal desorption of the species not being incorporated into the crystal

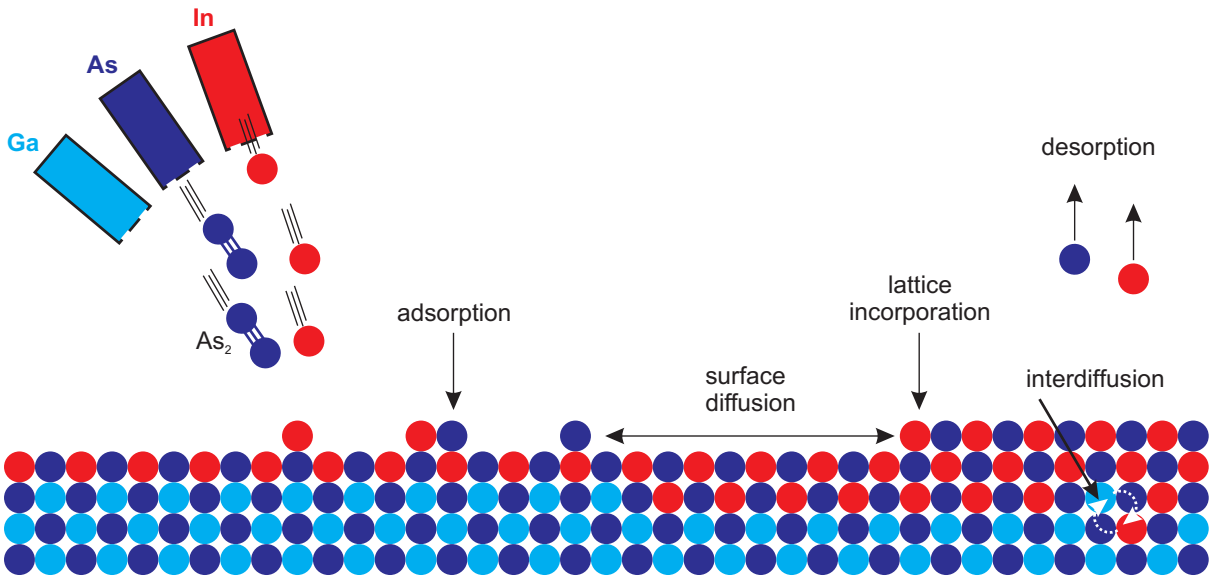

FIGURE 2.2: Schematic processes occurring during MBE growth.

The correct adjustment of the substrate temperature is one principal task for MBE growth. While low-temperature growth is limited by insufficient surface diffusion processes, the high-temperature growth is limited by the required balance between adsorption and desorption processes. Generally MBE growth is performed near the low-temperature limit, where surface diffusion is faster than the adsorption processes and desorption is negligible.

In the case of InAs quantum dot growth on GaAs, typically a GaAs layer with a $\beta 2(2\times4)$ surface reconstruction is first grown on the GaAs(001) substrate at temperatures between 480°C and 610°C [48, 49]. Then the temperature is reduced for the formation of a GaAs−c(4×4) surface. Afterwards InAs quantum dot growth takes place between 420°C and 510°C [30, 49, 50]. The MBE-grown samples discussed in chapter 5 and section 7.2 were grown in this way, with growth rates of 0.02−0.10 ML s^{-1} for InAs and 0.2−0.5 ML s^{-1} for GaAs.

2.1.2 Metal-organic chemical vapor deposition

In MOCVD the metal-organic precursors flow over the heated substrate within a carrier gas like H_2 or N_2. The growth takes place as shown schematically in Fig. 2.3. The important processes are:

- Homogeneous gas-phase reaction or surface reaction, resulting in the components for the crystal lattice growth
- Transport of the growth relevant atoms towards the surface
- Adsorption, surface diffusion, and interdiffusion
- Incorporation of the growth relevant atoms into the lattice structure
- Desorption of the atoms and molecules not being incorporated into the crystal

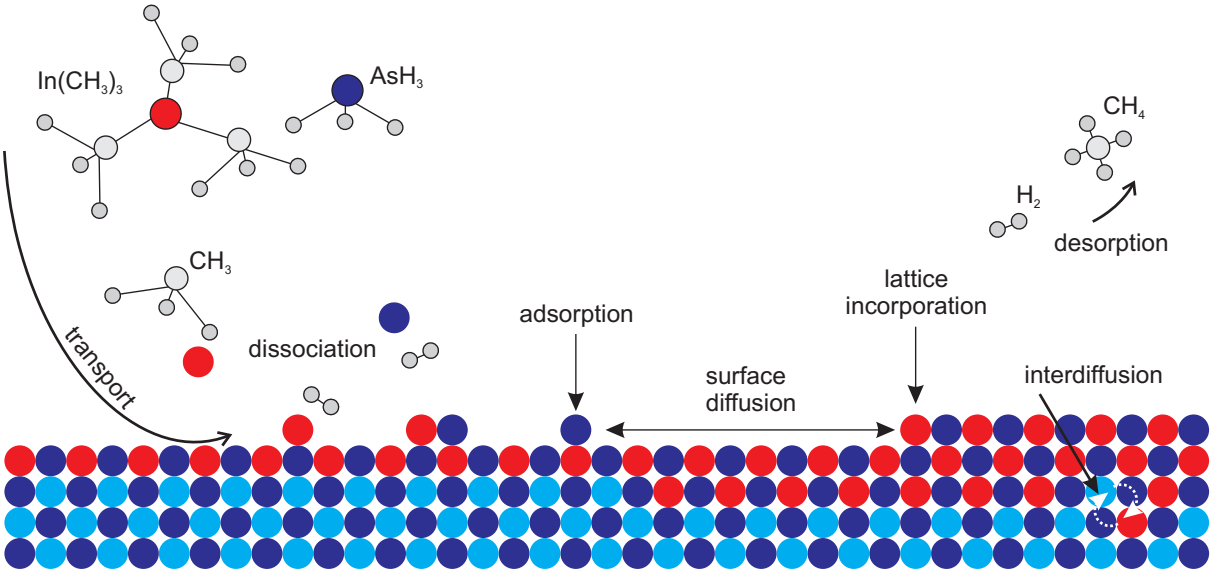

FIGURE 2.3: Schematic processes occurring during MOCVD growth.

Compared with MBE growth, the growth rates in MOCVD are generally faster. Thus on the one hand the growth of very small structures like quantum dots requires higher accuracy, but on the other hand increased growth rates are more favorable for thick layers, as e.g. required for laser devices and used in industrial facilities. Additionally, the growth temperature varies over a larger temperature range and is typically between 500°C and 800°C [51]. For samples investigated in this work (chapter 6 and section 7.1) GaAs is grown at 600°C and the In(Ga)As(Sb) quantum dots are grown at 480−500°C [52, 53]. The InAs growth rate amounts to about 1 ML s^{-1} and is thus clearly larger than in MBE growth, while GaAs overgrowth varies between 11 and 21 ML s^{-1} and is therewith considerably faster.

2.2 Capping procedure for devices

The growth processes described above are just the major ones, and detailed growth on the atomic scale is still not completely understood. Nevertheless, growth of high quality quantum dot structures for laser devices is possible and has been performed for several years, even for industrial application [15, 54, 55].

For all devices it is necessary to cap the self-organized quantum dot structures with the matrix material. During the overgrowth process several steps are introduced for high quality device production. These steps may be the change of temperature, the introduction of growth interruptions, and material or composition variations. It is still under intense investigation, in which way these parameters influence the structure and composition of the buried quantum dots [27–30, 56]. Thus in this thesis structural changes of quantum dots occurring during the capping process will be investigated.

A well-suited configuration for analyzing the change of quantum dots during capping is a cross-sectional investigation of the capped nanostructure. A frequently used tool is cross-sectional transmission electron microscopy (cross-sectional TEM), also with its more detailed modification called high-resolution TEM (HRTEM). In this work an alternative method is used, namely cross-sectional scanning tunneling microscopy (XSTM). XSTM has atomic resolution and is therewith an excellent tool for the structural investigation of buried nanostructures. In the following chapter XSTM, TEM, and other structural and optical characterization methods will shortly be explained, discussing their benefits and disadvantages.

Chapter 3

Characterization methods

The main methods to investigate the spatial structure of quantum dots are atomic force microscopy (AFM), transmission electron microscopy (TEM), and scanning tunneling microscopy (STM). This chapter gives an introduction to these methods with the main focus on STM. Furthermore photoluminescence spectroscopy (PL) will be introduced, since it is the frequently used optical characterization method. For a more detailed description of the different techniques, however, it is referred to relevant literature [2, 57–60].

3.1 Conventional and cross-sectional scanning tunneling microscopy

First experimental results using scanning tunneling microscopy were published by Binnig, Rohrer, Gerber, and Weibel in 1981−82 [61, 62]. Since that time STM has become the major tool for structural surface characterization, as it is displayed by many textbooks about STM, see for example Refs. [59, 63, 64]. The wide field of scanning probe methods is still in progress, e.g. developing methods using the tip of an STM as a local detector in optical spectroscopy [65].

The first cross-sectional investigations of cleaved III−V semiconductor samples with STM were performed 1986/87 by Muralt et al. [66] and Feenstra et al. [67]. For XSTM experiments typically a layered semiconducting sample is cleaved in an ultra-high vacuum (UHV) system. Many atomically resolved data of heterostructures have been published using XSTM [68–72] and since 1997 also quantum dot structures have been examined [73–76].

In an STM experiment, a sharp conducting tip is brought into a distance d of only a few Ångstrøm (1 Ångstrøm = 1 Å = 0.1 nm) to the cleavage surface, as shown in Fig. 3.1. Hence, electrons have a certain probability to *tunnel* from the surface to the tip or vice versa, which is called *tunneling effect* in quantum mechanics. If in addition a sample bias V_S between tip and sample is applied, a tunneling current I_T can flow, which is typically in the pA to nA range. Using this effect, the tip is scanned across the sample surface, and at each point of the grid the value of the tunneling current is evaluated. The

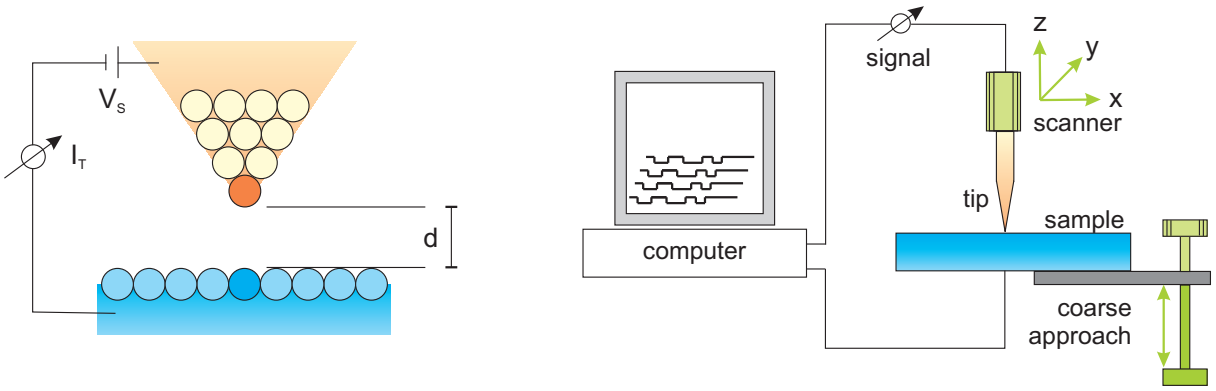

FIGURE 3.1: Principal function of an STM. On the left: Ideal configuration of tip and sample. On the right: Tip and sample coarse positioning, scanner for x-y-z movement, and the computer control system.

measured signals are transferred to a computer and converted into a topographic image of the sample surface.

For the x-y-z scanner a piezo tube is used and with an additional electronic feedback circuit the distance between tip and sample can be controlled. The coarse approach of the sample is usually realized by a shear piezo system. The whole STM setup is isolated from vibrations by springs and an additional damping.

For the remarkable local resolution the exponential dependence of the tunneling current on the separation d between tip and sample is important. A height variation of the tip of 1 Åresults in a change of the tunneling current of about one order of magnitude. This strong dependence of the current on the distance makes the STM to the most powerful surface probe technique in *real space*, providing atomic resolution in most cases.

Either the tip height or the measured tunneling current can be used as STM signal. In the first case the current value is kept constant by an electronic feedback circuit, which keeps the local distance between tip and sample and thus the tunneling current constant. The method is called *constant-current* mode and is shown in Fig. 3.2 (a). The second method keeps the distance between sample and tip globally constant, and the

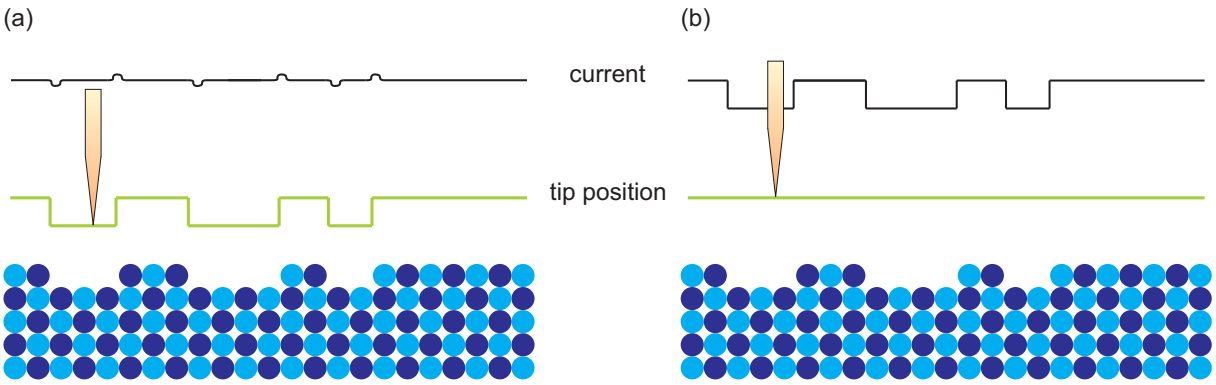

FIGURE 3.2: Schematic principles of (a) constant-current mode and (b) constant height mode. In both cases the influence of the tip radius is neglected.

varying current value is recorded. This technique is called *constant-height* mode and can preferentially be used for flat surfaces [Fig. 3.2 (b)].

In this work the *constant-current* mode is used, since the cleavage surface frequently has steps of up to some nm height, so that only in this mode the tip can be prevented from collisions. The disadvantage of this mode is a slower scan rate due to the timescale of the electronic feedback circuit. A theoretical description of the tunneling current and examples of STM setups are given in Refs. [59, 77] and the references therein.

3.2 Atomic force microscopy

A further development of the scanning tunneling microscopy is the scanning or atomic force microscopy. It was as well invented by Binnig et al. in 1986 [78].

The AFM works comparably to the STM, regarding the coarse positioning mechanism, the piezoelectric scanner, the feedback electronics, the computer control system, and the vibration isolation system. The major difference is that the tunneling tip is replaced by a mechanical tip, reacting on mechanical forces like van der Waals interaction of atoms. The detection of the tunneling current is replaced by the detection of the deflection of a cantilever. The AFM tip is mounted on the cantilever spring and the weak force interaction between the sample and the tip causes the cantilever to bend, according to Hooke's law. The resulting deflections can be monitored by optical detection methods. A topographic map of a sample surface is obtained when keeping the force constant by varying the tip-sample distance while scanning across the surface.

The AFM can be operated in the non-contact regime, in the contact regime, or in a combination of both called tapping mode. In the non-contact mode, the van der Waals force, the magnetic force, or the electrostatic force is detected. For high-resolution imaging the tapping mode is applied, additionally using the repulsive Coulomb force of the contact mode.

In contrast to STM, which needs a metallic or semiconducting material to measure the tunneling current, the advantage of the AFM technique is to use it also for investigations of insulators. The acting forces in AFM can be measured for any solid surface exposed to vacuum, air, or even a liquid, leading to a broad field of research areas. It is nowadays frequently used in chemistry and biology e.g. for imaging DNA molecules [79].

The AFM technique is additionally often used for the ex-situ characterization of quantum dot growth, since an analysis of quantum dot density can be easily achieved also after sample oxidation in air [80, 81]. The size of quantum dots can also be measured with almost atomic resolution, but the necessary effort is considerably higher than using the STM technique.

3.3 Transmission electron microscopy

Transmission electron microscopy and high-resolution TEM give important structural information on the atomic scale of semiconductor heterostructures. TEM experiments can be performed in plan-view and in cross-sectional geometry. In both cases the sample has to be thinned down to dimensions of 10 to 100 nm, such that the electron beam may be transmitted.

TEM is used in two basic modes: Imaging the diffraction pattern or projecting real space images. Images can be obtained using the directly transmitted electrons or selective scattered ones, depending on the chosen aperture. In a bright-field image the undeviated electron beam is taken into account, while in the dark-field modus only diffracted beams without the primary beam are monitored, see e.g. Refs. [57, 82] and references therein. Usually the chemically sensitive (002) reflex or the more strain sensitive (004) reflex are used in dark-field and bright filed images for InAs/GaAs quantum dot investigation [2, 83–85]. The strain sensitive images show the quantum dot positions, while chemically sensitive images can be used to determine the size and shape of quantum dots. Furthermore the indium content of the quantum dots can be derived from the ratio of the amplitudes of the (002) and (004) reflections [83].

In high-resolution TEM even the atomic structure can be resolved, but it must be emphasized that the contrast seen in such images is not directly related to single atoms. Instead, rows of atoms are imaged and an involved theoretical analysis, which takes into account details of the electron scattering process, is necessary for a detailed interpretation of the spots in terms of atomic positions.

Nevertheless, data obtained by TEM can have a spatial resolution in the order of 0.1 nm, but this signal is integrated over the thickness of the sample, which is typically a few ten nanometers. However, this averaging may also be an advantage, since using this method statistics of the average size of the quantum dots may be easier to achieve than in XSTM experiments. Recent investigations using HRTEM techniques were e.g. in the field of indium and gallium segregation, indium and gallium composition variation, and strain contrast in the InGaAs/GaAs system [25, 86, 87].

3.4 Photoluminescence spectroscopy

Optical experiments are particularly well suited to reveal the unique electronic properties of zero-dimensional systems [88]. Excited single quantum dots emit very narrow spectral lines due to the δ-shaped density of states. In photoluminescence (PL) and PL excitation (PLE) experiments, the excitation occurs via the absorption of photons, creating electron-hole pairs. When these electron-hole pairs recombine again, the newly generated photons can be detected.

For the characterization of quantum dots with PL usually a photon energy larger than the bandgap of the matrix material is used for excitation, so that the photoinduced carriers can relax into the quantum dot and afterwards recombine radiantly. With increasing

excitation density, additional exited quantum dot states contribute to the luminescence spectra. In PLE experiments the photon energy of the excitation source is varied, while the emission from quantum dots at a specific photon energy is monitored. The coincidence between the excitation energy and existing energy states leads to an absorption process generating an exciton, which recombines again after relaxation. Thus in PLE spectra the absorption energies of a samples can be determined giving information on the energies of the quantum dot states.

PL techniques are frequently used for a rapid characterization of quantum dots, since luminescence intensity, peak position, and peak width are connected to the quantum dot density, size and size distribution. Also a more detailed analysis of quantum dot subensembles or single dot spectroscopy are possible [89–91].

Chapter 4

Setup and data analysis

The investigated quantum dot samples are analyzed using two home-built scanning tunneling microscopes. The corresponding systems are introduced in this chapter, explaining the setup as well as tip and sample preparation. Furthermore the investigated GaAs(110) surface structure and the contrast mechanisms important for XSTM image interpretation are presented. In the last part of this chapter the data analysis is described regarding quantum dot size, shape, and density, as well as the stoichiometry determination of a quantum dot and the wetting layer.

4.1 Microscope chambers

Both microscope chambers contain a home-built scanning tunneling microscope. The one originally designed for top-view investigations is called STM chamber. In this design the sample has a fixed position and the tunneling tip is located on a walker for coarse approach, which can be moved with a shear piezo system. Up to twelve replacement tips can be stored in the STM chamber. The STM is used with a control electronics and scan software, which are both home-built. The cleavage of the sample is performed in a preparation chamber by pushing the sample on a magnetic transfer against a fixed object. After the cleavage the sample is transferred into the STM chamber. For a more detailed description of the STM chamber see e.g. Refs. [92, 93].

The other microscope chamber, being called XSTM, is specially designed for cross-sectional investigations. The main design difference compared with the STM chamber is a fixed tip position, while the sample is moved for coarse positioning. The XSTM is used with an RHK Technology SPM 1000 control system, an SPM 100 control electronics as well as an XPM Pro^{TM} scan software. In addition to the RHK software, also CM Utility^2 [94] and WSXM [95] are used for image processing. The sample is cleaved in the XSTM chamber by pulling the sample holder against the scan block. Until now only six tips can be stored in the XSTM chamber, but up to 32 additional tips are positioned in the preparation chamber [96]. A detailed description of the XSTM setup can be found e.g. in Refs. [97, 98]. For a general description of scanning tunneling microscope designs see e.g. Ref. [59].

Both microscopes operate in ultrahigh vacuum (UHV) with a base pressure below 1×10^{-10} mbar (1 mbar = 100 Pa), so that sample cleavage in the UHV results in a (110) cleavage surface, remaining clean for several days. After approaching tip and sample and testing the tip quality, the layers of interest have to be found. They are located almost next to the edge of the cleavage surface, so that the following strategy for finding the relevant structures is used [68, 97, 99]: Prior to the microscopic search of the layers, the edge of the sample has to be found. For this purpose, the tip is retracted from tunneling position and moved towards the sample edge in large steps. After each step only the tunneling contact is controlled by shortly enabling the feedback control. This procedure is repeated until no tunneling current is measured and therewith the cleavage edge is detected. The tip is then moved back a little more than the extension of the epilayer thickness. Afterwards large images are taken to locate the quantum dot layers and to perform structural investigations. A photograph of the tip and sample setup is shown in Fig. 4.1 (a).

4.2 Tip and sample preparation

For both microscope setups a tungsten wire is used to produce the tunneling tips. The wire is electro-chemically etched in NaOH [93, 100]. After etching, the tips are fixed on the tip holder and transferred into the UHV system. In the preparation chamber the tips are cleaned by electron bombardment for 2−3 minutes. Therefore a high voltage of about 350 V is applied between tip and filament. An additional heating current through the filament of about 1−3 A is leading to the used emission current of about 0.5−3 mA, depending strongly on the tip and filament geometry.

The sample preparation starts with mechanical polishing down to a wafer thickness of 150−200 μm. It turned out that thicker samples cleave worse and thinner samples are more difficult to handle. The thinned sample is cut into pieces of about 4.5×5 mm^2, and parallel to the smaller side an approximately 1.5 mm long scratch is made in order to

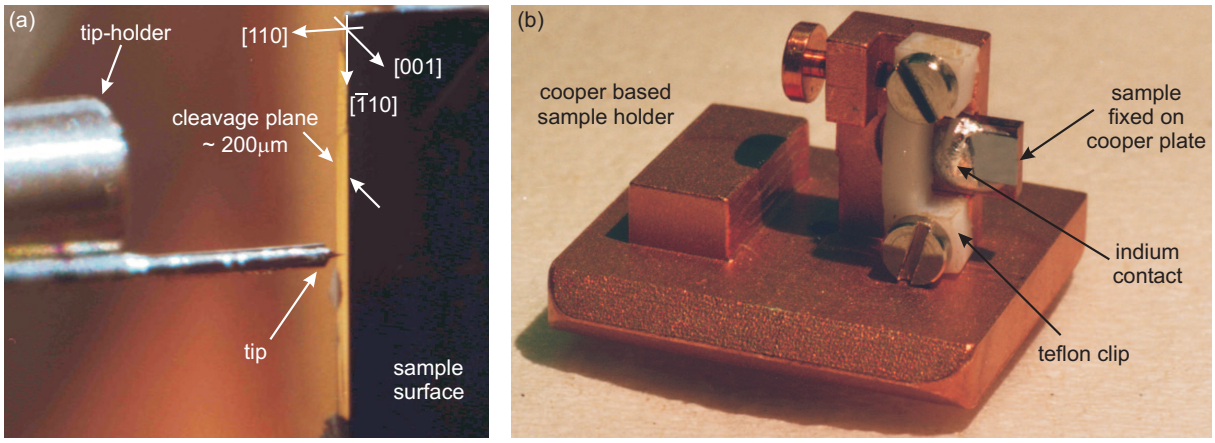

FIGURE 4.1: Photograph of (a) tip and cleaved sample, and (b) a sample holder used in the XSTM chamber.

predefine the cleavage of the sample. The mounted and electrically contacted sample is transferred into the UHV system. A photograph of a cleaved sample on an XSTM sample holder is shown in Fig. 4.1 (b).

4.3 GaAs(110) surface structure

In the present work the investigated nanostructures are all grown on GaAs wafers. GaAs has a cubic zincblende structure and cleaves mainly along its non-polar {110} planes. The {110} surfaces have an equal number of group-III cations (e.g. Al, Ga, In) and group-V anions (e.g. As, Sb), and the cleavage results in two *dangling bonds* in each surface unit cell. The ideal bulk surface is unstable and thus the surface lowers its energy by displacing the surface anions outward, while the cations move inward [101], which is called *buckling* of the GaAs(110) surface. This relaxation of the atoms relative to the ideal truncated bulk position does not change the lateral size of the unit cell, but after the relaxation the dangling bond of the group-III atom is empty and the one of the group-V atom contains both electrons.

Figure 4.2 shows the relaxed GaAs(110) surface. The topmost layer consists of chains of alternating gallium and arsenic atoms, the so-called *zigzag chains*, indicated by slightly

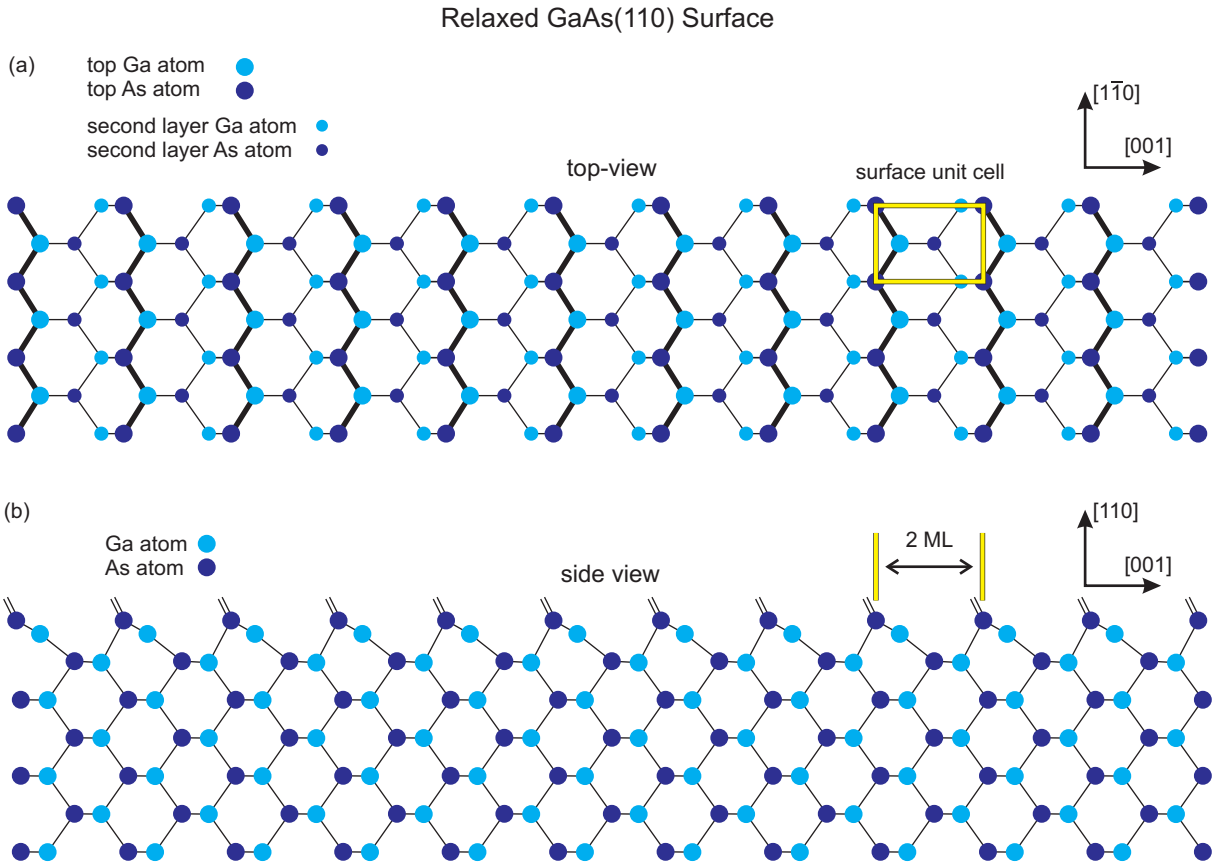

FIGURE 4.2: Schematic view of the relaxed GaAs(110) surface, after Ref. [97]. (a) Top view image with surface unit cell and (b) side view of the surface.

broader lines in Fig. 4.2 (a). The dimensions of the unit cell along [001] direction is the bulk lattice constant $a_0 = 0.565$ nm, along $[\bar{1}10]$ direction it is $\frac{a}{\sqrt{2}} = 0.400$ nm, and the monoatomic step height amounts to 0.200 nm. It should be noted here, that in XSTM images only every second monolayer can be imaged, which corresponds to the topmost atoms in the side-view image of Fig. 4.2 (b).

4.4 Contrast mechanisms in XSTM

For an interpretation of constant-current mode XSTM images different contrast mechanisms have to be taken into account, especially the electronic and topographic contrast. The electronic contrast can be divided into atom-selective, uncharged adsorbate, and charged defect contrast, whereas the topographic contrast contains step-height and strain-relaxation contrast. Some of these mechanisms are exemplarily shown in different STM images in Fig. 4.3, and in the following a brief description of these contrast mechanisms is given. For a more detailed description see the respective literature.

- **Atom-selective contrast:** Depending on the sample bias polarity different atoms are imaged, e.g. gallium or arsenic atoms in the case of GaAs(110) [Fig. 4.3 (a)]. At negative sample bias mainly the occupied states of the arsenic atoms can be seen, whereas at positive sample bias the unoccupied states of the gallium atoms are imaged [67, 102].

- **Uncharged impurity contrast:** The different bond lengths of uncharged impurities in the matrix change the local density of states, leading to a different tip position at the adsorbate position [Fig. 4.3 (b)], e.g. single indium atoms in GaAs [103, 104] or InAs/InGaSb structures [105].

- **Charged defect contrast:** Charged dopant atoms or defects lead to a contrast variation with spherical symmetry due to the locally different charge density [106–108]. A similar behavior is observed next to charged steps [Fig. 4.3 (c, e)] [109].

- **Spatial contrast from terraces, steps, and adsorbates:** Direct topographic contrast from the height differences at terraces, steps, or adsorbates lead to a height variation of the tunneling tip [Fig. 4.3 (d)].

- **Strain relaxation:** Buried semiconductor nanostructures like quantum dots are often highly strained. After sample cleavage compressively strained objects relax outwards, resulting in a topographic contrast [97]. An example of this mechanism together with a simulated images is shown in Fig. 4.4 for an InAs/GaAs quantum dot stack.

In XSTM data the electronic and topographic contrast mechanisms often occur in a combination. For clarification images can be taken at different bias polarities and different bias voltages, since low bias images are dominated by electronic effects, while high bias images almost only show the spatial contrast.

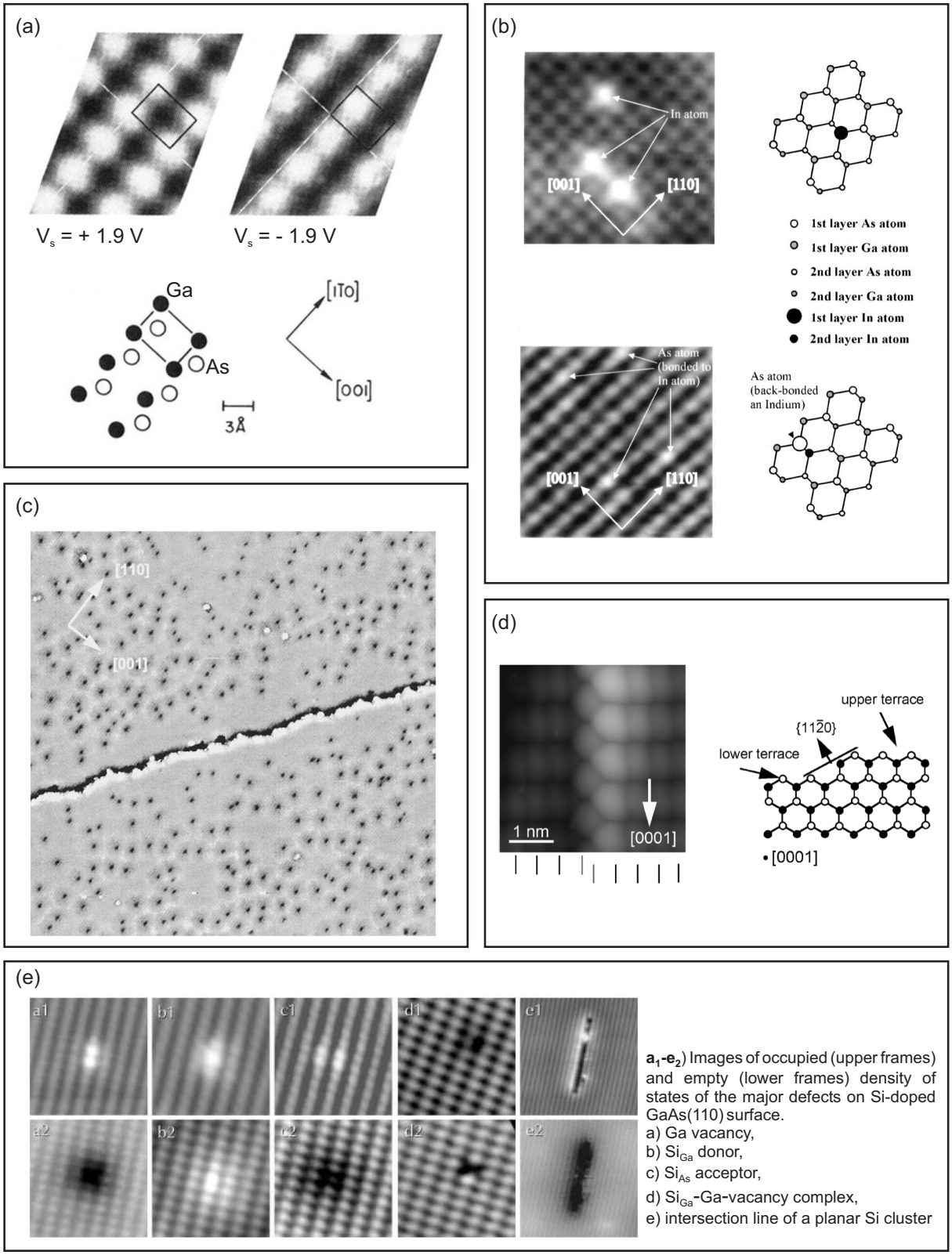

FIGURE 4.3: XSTM images as examples for different contrast mechanisms: (a) Atom-selective imaging of the GaAs surface [67]. (b) Indium incorporation in a GaAs matrix as an example for uncharged impurity contrast [104]. (c) Charged surface step on InP(110) after annealing [109]. (d) Topographic contrast of a step on the CdSe(10$\bar{1}$0) surface [110]. (e) Different defects occurring on highly Si-doped GaAs(110) surfaces [106, 108].

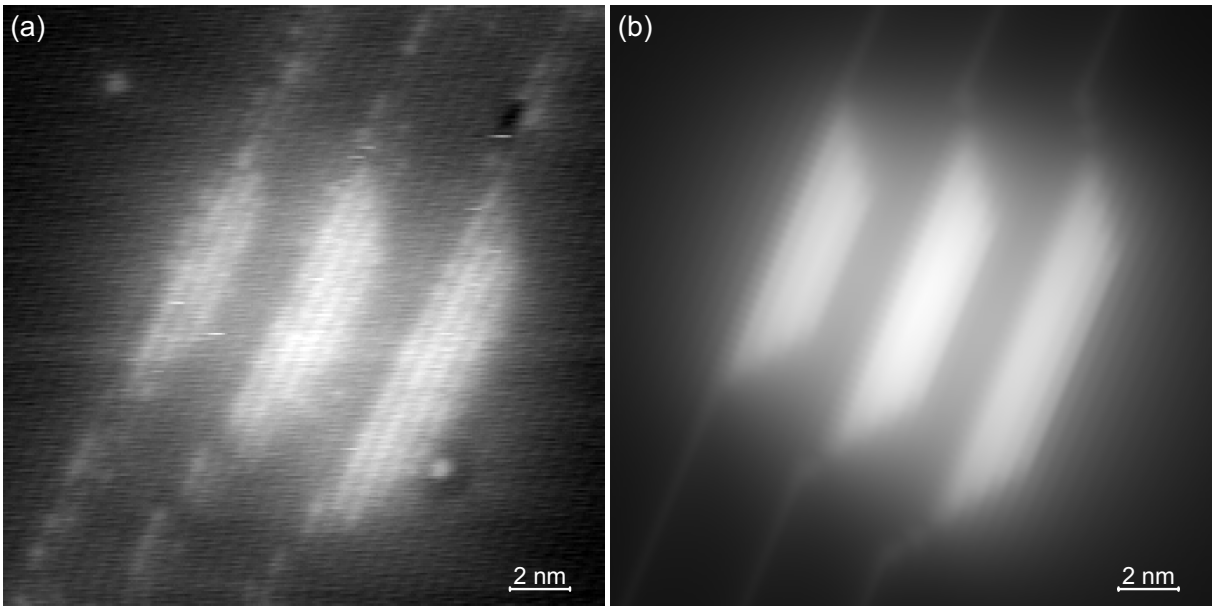

FIGURE 4.4: (a) Filled-state XSTM image and (b) simulated strain relaxation image of an InAs/GaAs quantum dot stack [97].

4.5 Structural and chemical characterization of quantum dots

In this section the analyzing tools for XSTM images used later on are described. In order to compare the spatial structure of uncapped and capped quantum dots, the identification of the size and shape including side facets is very important. This can be done from XSTM images with good accuracy using the atom-selective contrast [111]. After size identification also the quantum dot density can be determined. Another often-used tool is the examination of the stoichiometry of the quantum dot and the wetting layer. In some cases the composition distribution of a quantum dot can be estimated directly from the image. For more detailed information on the local stoichiometry the observed atomic distances in growth direction are compared with the lattice constant of the GaAs matrix.

4.5.1 Quantum dot size

The correct measurement of the size and shape of a quantum dot strongly depends on the quality of the atomic resolution of the XSTM image. Most images presented in this work show clear atomic resolution along [001] growth direction. As shown in Fig. 4.5, for the case of GaAs(110), the chain-distance along the [001] direction is equal to the lattice constant a, and thus the height of a quantum dot in [001] direction can be determined by directly counting the atomic zigzag chains (see section 4.3). In the perpendicular direction the extension of the surface unit cell only amounts to $\frac{a}{\sqrt{2}}$, which frequently is below the resolution of the STM. In both cases a direct counting of the unit cells is leading to the quantum dot extension with an accuracy of half a surface unit cell.

One has to notice that although the calibration of the STM setup is done carefully,

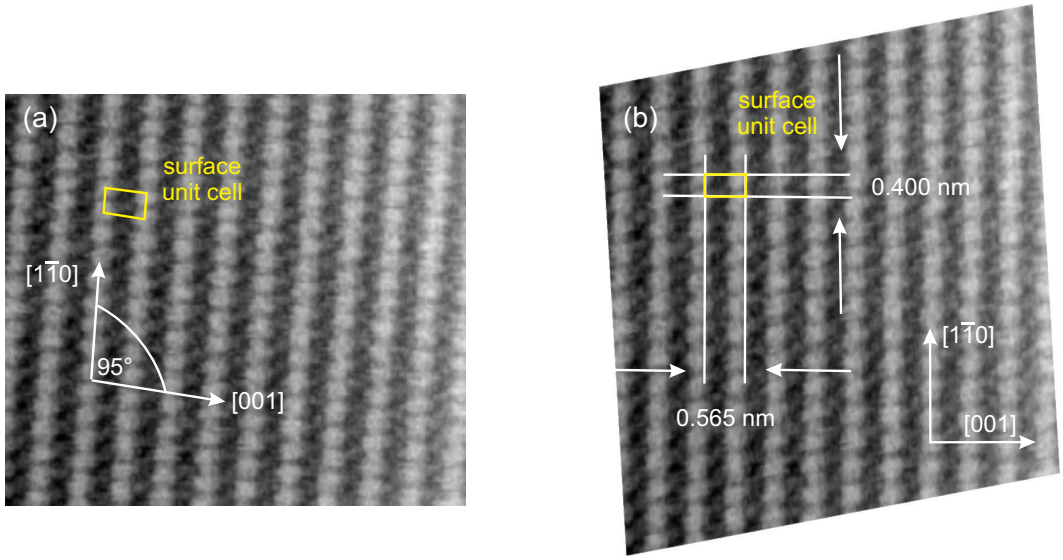

FIGURE 4.5: Atomic resolved XSTM images showing the surface unit cell. (a) Original data and (b) after image correction.

thermal expansion due to temperature variation leads to a thermal drift between tip and sample. This effect changes the actual size of scanned areas as compared with the nominal value of the image. Due to the drift a smaller or larger image size value is obtained. Since this effect is time dependent, it has a larger influence perpendicular to the scanning direction, which is usually in [001] direction. Consequently, if no surface unit cells can be counted in [110] or [1$\bar{1}$0] direction, the size of the quantum dot baselength can just be approximated. Depending on the STM chamber and especially on the used scanning piezo, the error of the baselength determination typically varies between 10 and 20% [112].

A further effect to consider is the so-called piezo creep. If a high bias change is applied suddenly to the piezo it takes some time, until the piezo has actually reacted on the bias change. This time interval has to be taken into account, otherwise considerable creep effects remain, which are similar to thermal drift and complicate the later analysis. In the case of starting acquisition of a large image, one should e.g. wait a few seconds or even better start and stop the image several times, until the piezo has actually reached the specified starting position. For smaller images or with faster scan rates the creep effect is less crucial.

4.5.2 Shape and side facets of a quantum dot

Data with atomic resolution along both directions can be displayed undistortedly by correcting the drift and creep effects using the known aspect ratio of the rectangular surface unit cell. After image correction the size of the object, their actual aspect ratio (height to baselength), and the boundary line of the facets can directly be determined. An example for such an image correction is shown in Fig. 4.5. In the original image (a) the [1$\bar{1}$0] direction does not appear perpendicular to the [001] direction and also the aspect

ratio of the surface unit cell (indicated as a yellow box) has to be corrected. The same image after correction by shearing, rotating, and stretching is shown in Fig. 4.5 (b).

The aspect ratio and the boundary lines of the facets are very important for accurate quantum dot shape determination. If the image is compressed or stretched and cannot be equalized, the accuracy of the measured angle between the side facet and bottom line of the quantum dot is limited to $10-15°$.

For the determination of the quantum dot shape one has to further consider that in XSTM images only cross-sections of the quantum dots are visible. Thus in principle only a two-dimensional cut through the quantum dot shape can be examined. However, the contrast from strained quantum dots in XSTM images also allows to determine in which depth the quantum dot is cleaved, and to derive the correlated shape of quantum dots. Such an analysis, however, requires detailed strain simulations of the images [97].

Quantum dot density

In XSTM images also quantum dots underneath the cleavage surface can be seen due to their strain field. This is important for the calculation of the quantum dot density, as it can be assumed that even a quantum dot, which is located at a depth of about 25% of its diameter underneath the surface, can still be identified, resulting in an STM perception depth of 5/4 of the quantum dot diameter. In this way the quantum dot density can be calculated under consideration of a homogeneous and stochastic distribution at the growth surface. Thus the quantum dot density is equal to the quotient of the number of observed quantum dots divided by the specific scanned distance times the perception depth.

Side facets

The determination of the side facets is of particular importance with regard to possible structural changes of quantum dots during capping. Recently observed and atomically resolved quantum dot shapes derived from top-view STM [113, 114] will be compared here with XSTM images of the same structures after capping. The change of the side facets thereby gives direct evidence for structural changes during overgrowth.

The determination of the side facets from XSTM data are demonstrated in the following [97]: A quantum dot with a truncated pyramidal shape is assumed, which is sketched for different cleavage geometries in Fig. 4.6 (a). The angle α between the facet boundary direction $\underline{b}$ and the quantum dot baseline can be calculated under consideration of simple vector analysis. It should be noted that for most high-index facets $\underline{f}$ the angle α depends on the cleavage surface plane. A good example is the later discussed {137} side facet, whose angle towards the $(\bar{1}10)$ surface amounts to 22° and towards the (110) surface to 11°. Further discussed side facets of InAs/GaAs quantum dots [115] and their respective angles are listed for both cleavage surfaces in Fig. 4.6 (b).

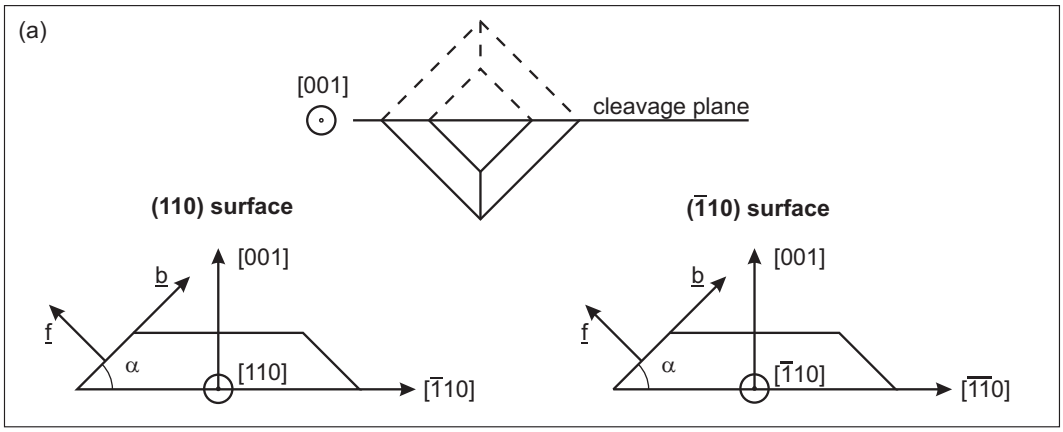

(b)

(110) surface			(1̄10) surface		
side facet f	boundary direction b	angle α	side facet f	boundary direction b	angle α
(101)	[1̄11]	35.3°	(101)	[11̄1]	35.3°
(111)	[1̄10]	0°	(111)	[11̄2]	54.7°
(1̄11)	[11̄2]	54.7°	(1̄11)	[11̄0]	0°
(11̄2)	[222]	35.3°	(112)	[22̄2]	35.3°
(11̄3)	[332]	25.2°	(113)	[33̄2]	25.2°
(11̄4)	[442]	19.5°	(114)	[44̄2]	19.5°
(124)	[44̄1]	10.0°	(124)	[44̄3]	27.9°
(125)	[55̄1]	8.0°	(125)	[55̄3]	22.9°
(135)	[55̄2]	15.8°	(135)	[55̄4]	29.5°
(136)	[66̄2]	13.3°	(136)	[66̄4]	25.2°
(137)	[77̄2]	11.4°	(137)	[77̄4]	22.0°
(2 5 11)	[11̄ 11 3̄]	10.9°	(2 5 11)	[11̄ 11̄ 7]	24.2°
(3 7 15)	[15̄ 15 4̄]	10.7°	(3 7 15)	[15̄ 15̄ 10]	25.2°

FIGURE 4.6: (a) Sketch of the facets and associated angles at the (110) and (1̄10) cleavage surface, after Ref. [97]. (b) List of typical side facets and their respective angles.

4.5.3 Stoichiometry of quantum dot and wetting layer

Shape, size and composition of a quantum dot have a strong influence on its electronic properties [22, 24, 25]. Theoretical calculations show that a change of the InGaAs composition of only 30% causes an energy shift of some tens of meV, while a change of the composition profile affects the energy even stronger by a shift of up to 150 meV [22]. For that reason the accurate determination of the quantum dot stoichiometry and the composition distribution is very important for the calculation and interpretation of electronic properties. Moreover, the composition distribution is important for the understanding of the growth and capping process and thus for improving the growth for device applications.

The composition of InGaAs nanostructures can be determined from XSTM data due to the lattice mismatch between InAs and GaAs, resulting in a correlation between the local lattice constant and the stoichiometry [97, 111, 116–118]. Thus the local lattice constant is evaluated, which is given by the distance between neighboring atomic chains. Figure 4.7 shows the main steps of the stoichiometry determination procedure. It starts with taking a height profile parallel to the growth direction, averaged for better statistics perpendicular to it over the area indicated by the cyan box (a). The height profile data are plotted in Fig. 4.7 (b), showing undulations due to the atomic chains superposed by

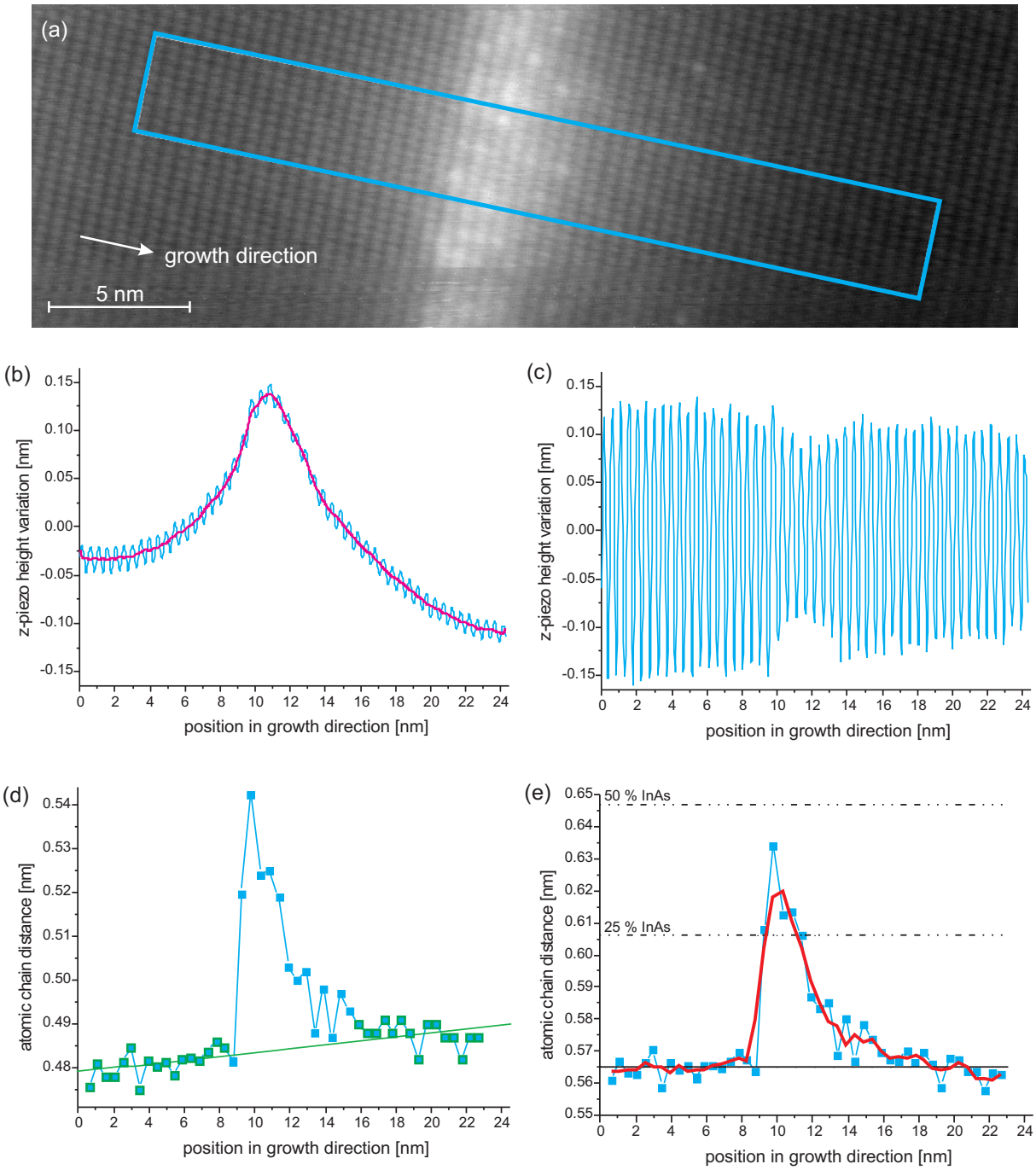

FIGURE 4.7: Evaluation of the local stoichiometry of an InGaAs wetting layer: (a) XSTM image with the height profile position indicated by the cyan box. (b) Height profile (cyan) and smoothed background curve (magenta). (c) Difference curve from (b), representing atomic chain positions. (d) Atomic chain-to-chain distance without calibration (line + symbols) and linear fit of GaAs chains (green). (e) Calibrated atomic chain-to-chain distance (line + symbols) and three-point averaged curve (red). Simulated chain-to-chain distance values for 25% and 50% InAs in GaAs are indicated by the dotted-dashed lines.

a broader bump due to the strain induced relaxation of the quantum dot material, the latter represented by the smoothed curve (magenta). This background is subtracted from the height profile data and the resulting corrugation is shown in (c), containing only the

information of the local chain positions. This process may lead to a small error, because the lateral position of the imaged dangling bond of a surface atom in a cleaved quantum dot is slightly shifted from the actual atomic position due to the strain-induced surface curvature [98].

During the next step, for every positive maximum of the atomic corrugation a Gaussian fit is performed and its center position is registered. Then these values from neighboring positions are subtracted from each other. The resulting differences, corresponding to the atomic chain-to-chain distances, are shown by the cyan line and symbols in (d). In a last step, the atomic chain-to-chain distances corresponding to the GaAs chains of the matrix (green-framed symbols) are fitted with a linear or quadratic function and are calibrated with the nominal GaAs bulk lattice constant of 0.565 nm. This final result of the local lattice constant is shown by the cyan line and symbols in Fig. 4.7 (e), while the red line shows the three-point average of these data. The reference values for 25% and 50% InAs in GaAs obtained from strain relaxation calculations of thin InGaAs films [97] are indicated by the dotted-dashed lines.

It should be noted that the actual indium concentration in a quantum dot is slightly higher than the plotted data, since the dot is stronger compressed than a quantum well, and the compression leads to lower atomic chain distances. A smaller, but contrary effect for the quantum dot center is the error introduced by the surface curvature mentioned above. At the quantum dot baseline the dangling bonds of two neighboring atoms are bent towards each other, leading to an apparently smaller chain-to-chain distance, while it is larger at the dot center. Considering both effects the indium concentration calculated at the quantum dot center is slightly higher than the plotted data.

The determination of the local lattice constant value as described above is frequently achieved with two interacting software tools, developed by Becker and Lenz [94, 119]. In the first software the position of the height profile and the averaging area are selected, while the second one is used for the automatic determination of the chain-to-chain distance. A requirement for the determination are images of high atomic resolution, negligible surface adatoms, and with a considerably extension into the GaAs substrate and overlayer for accurate calibration.

The example shown in Fig. 4.7 belongs to an InGaAs wetting layer. The atomic resolution is clearly visible in the XSTM image, and the InGaAs layer shows an inhomogeneous indium distribution (a). The growth direction is to the right, and especially in the first 3−4 chains containing InGaAs, the indium concentration is relatively high. This visible impression is confirmed by the result shown in Fig. 4.7 (e), where the value of the atomic chain distance increases abruptly at the wetting layer bottom and than decreases in growth direction over 5−6 nm. The highest indium concentration amounts to about 40%. It should be noted that the indium concentration can also be derived by simple counting of the bright indium atoms observed in the image, leading to the same result. This demonstrates the high accuracy of the stoichiometry determination from the chain distances.

Chapter 5

Structural changes of InAs quantum dots during capping

In this chapter a comparison of top-view STM and XSTM images of InAs/GaAs quantum dots will be presented. The samples are grown under equal growth conditions in the same MBE chamber and are hence well comparable. It is demonstrated that the quantum dot structure considerably changes during capping. A model for the overgrowth process is presented.

5.1 InAs sample structure

The investigated samples were grown by MBE on GaAs(001) substrates by the group of Prof. Jacobi at the Fritz-Haber-Institut Berlin, as partly described in Refs. [49, 113]. After a GaAs buffer layer was grown at a temperature of 550−560°C, the sample was cooled down followed by a growth interruption of 600 s until the GaAs(001) c(4x4) diffraction pattern was observed with RHEED. Different sample preparation conditions were then chosen for the quantum dots in different samples, as shown in Fig. 5.1.

For sample I (a) 1.8 ML InAs were deposited at a growth temperature of 450°C and a growth rate of 0.017 ML s^{-1}. For the top-view STM images, sample I (a) was immediately transferred after growth under vacuum conditions to the STM chamber, where it was cooled down to room temperature before STM examination. For PL measurements [sample I (b)] a 50 nm thin GaAs cap layer was grown with a growth rate of 0.16 ML s^{-1} on top of the quantum dot layer.

Sample I (c) for XSTM and TEM experiments contains four additional quantum dot layers with increasing amount of InAs material separated by spacer layers and grown on top of the first quantum dot layer. Each dot layer was grown as follows: First a 600 s long growth interruption 1 (GI 1) for surface flattening was introduced. Afterwards the InAs quantum dot material was deposited at 450°C, followed by a 10 s short growth interruption 2 (GI 2) and a deposition of about 10 nm GaAs at 450°C, and further 90 nm GaAs at a maximum temperature of 520°C. The 100 nm thick GaAs spacer layers prevent correlation between the quantum dot layers. The five InAs layers contain 1.8 ML, 2.2 ML, 2.6 ML, 3.0 ML, and 3.6 ML InAs, respectively. Finally an 800 nm thick GaAs cap layer

was grown. The samples II and III only contain one InAs layer each. For sample II 3.6 ML InAs were deposited at 450°C, and sample III contains 1.8 ML InAs, which were grown at a lower temperature of only 420°C compared to sample I.

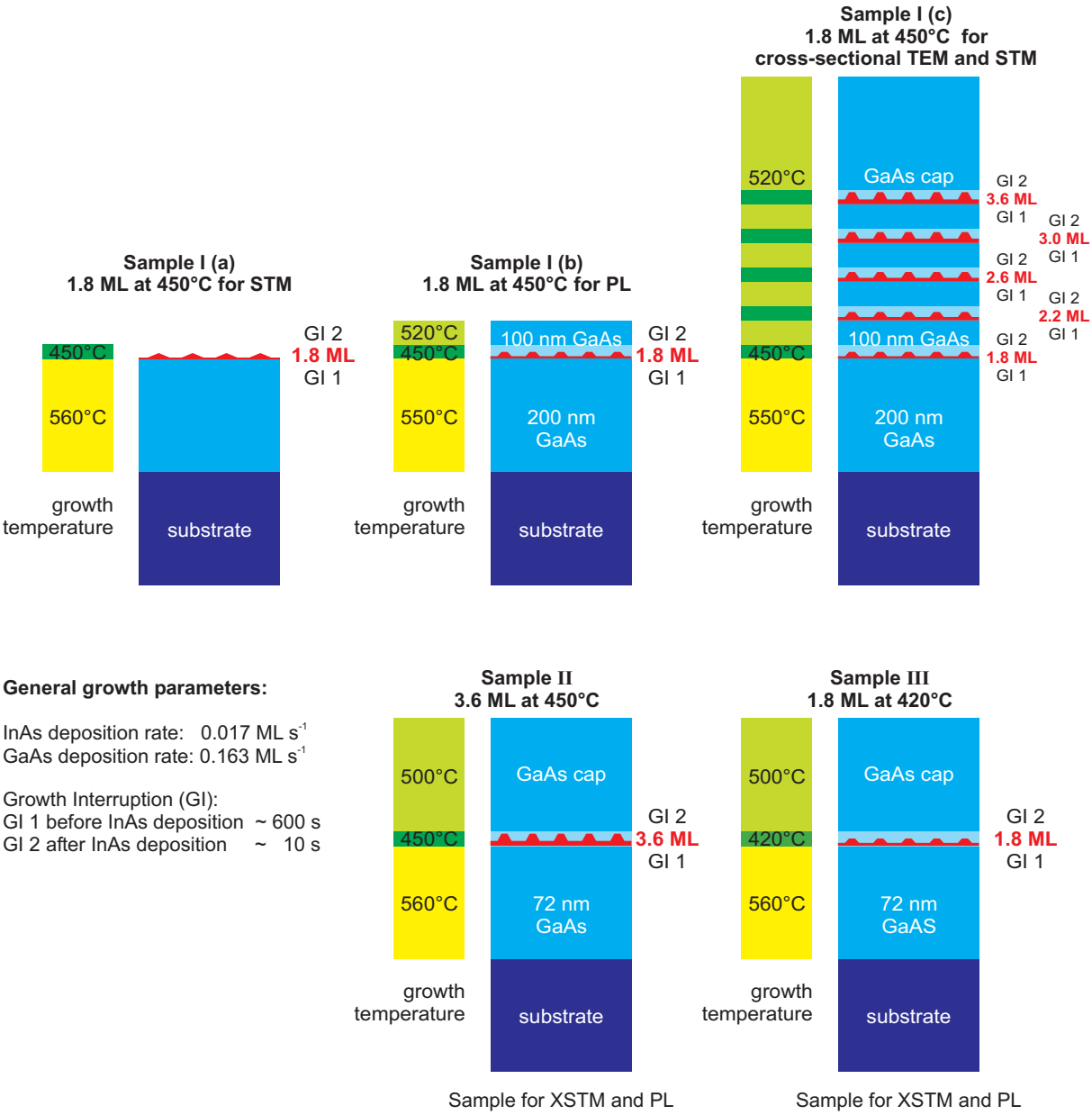

FIGURE 5.1: The InAs sample structures: Sample I contains 1.8 ML InAs grown at 450°C for comparison in (a) top−view STM experiments (b) PL measurements, and (c) XSTM/TEM experiments. The latter sample additionally contains four layers with an increasing InAs thickness of 2.2, 2.6, 3.0, and 3.6 ML. Sample II for XSTM and PL contains 3.6 ML InAs deposited at 450°C, and sample III contains 1.8 ML, grown under a lower growth temperature of 420°C as compared to sample I.

5.2 Top-view STM results

Top-view STM investigations of sample I (a) were performed by Márquez and Geelhaar, as reported in Refs. [49, 113, 120]. In a typical top-view STM image the InAs quantum dots are imaged as bright ellipses, as shown in Fig. 5.2. The quantum dot diameter or baselength varies between 5 and 20 nm and the height above the wetting layer between 2 and 3 nm. The majority of the quantum dots has baselengths around 12.5 nm and a height of 2.8 nm. The quantum dot density was derived as 1.9×10^{11} cm^{-2}, and the measured sizes agree e.g. with those found in Refs. [121–126], confirming the formation of typical MBE grown InAs quantum dots.

An atomically resolved STM image of a representative quantum dot is shown in Fig. 5.3 (a). The quantum dot has a pyramidal shape and four pronounced facets. Especially at the left side of the image atomically resolved dimer rows along the $[\bar{1}\bar{2}1]$ direction are visible. This area is shown in detail in Fig. 5.3 (b). From a comparison of the observed side-facet vectors $\vec{a}_1$, $\vec{a}_2$, and $\vec{a}_3$ with the values of several known GaAs surfaces it was demonstrated that the quantum dot sides are characterized by high index {137} facets [49, 113]. Other surfaces with similar orientations like {126} and {136} can be excluded since they would lead to other base vectors [49, 120].

Such high index facets were initially not expected. In previous theoretical studies, low-index {110} or {111} facets were considered [46]. The first indications for high-index facets were found by Hasegawa et al. [125], where {215} faceted planes were suggested based on STM images, however, without atomic resolution. Lee et al., in contrast, report on four {136} side facets on InAs quantum dots, estimated from RHEED patterns [126].

In addition to these four {137} facets, two smaller, but less resolved facets can be

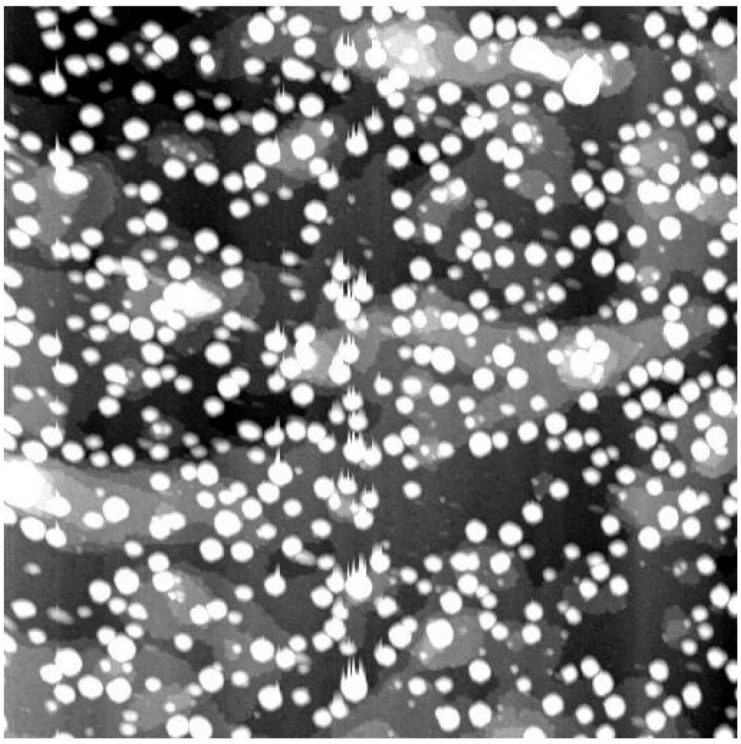

FIGURE 5.2: STM image showing InAs quantum dots as bright ellipses. Image size is 500×500 nm^2, $I_T = 0.19$ nA, $V_S = -2.25$ V, Ref. [49].

observed, leading to the shape model presented in Fig. 5.3 (c). These additional {111} facets appear more rounded than the {137} side facets, which can also be seen in the height profiles shown in Fig. 5.3 (d).

The profile along $[1\bar{1}0]$ direction has a rounded shape, which may be due to imaging limitations due to the tip apex. This would explain the discrepancy between the observed angle of about 45° and the nominal one of 54.7° for the {111} facet. The profile along the [110] direction is more triangular. In order to derive the angle between the side facet and the (001) substrate 53 quantum dots were evaluated from atomically resolved STM images scanned in alternating directions in order to prevent tip-induced effects [49]. In this way an average angle of the sides to the substrate of 21.3° was derived, which agrees with the {137} facet (nominally 22.0°). It should be noted, that due to the anisotropic shape of the quantum dots observed in top-view STM images comparisons with the XSTM results have to be performed at both cleavage surfaces.

In addition to the top-view STM results of sample I (a) also quantum dots with increasing amount of deposited material and thus with increasing size were investigated by

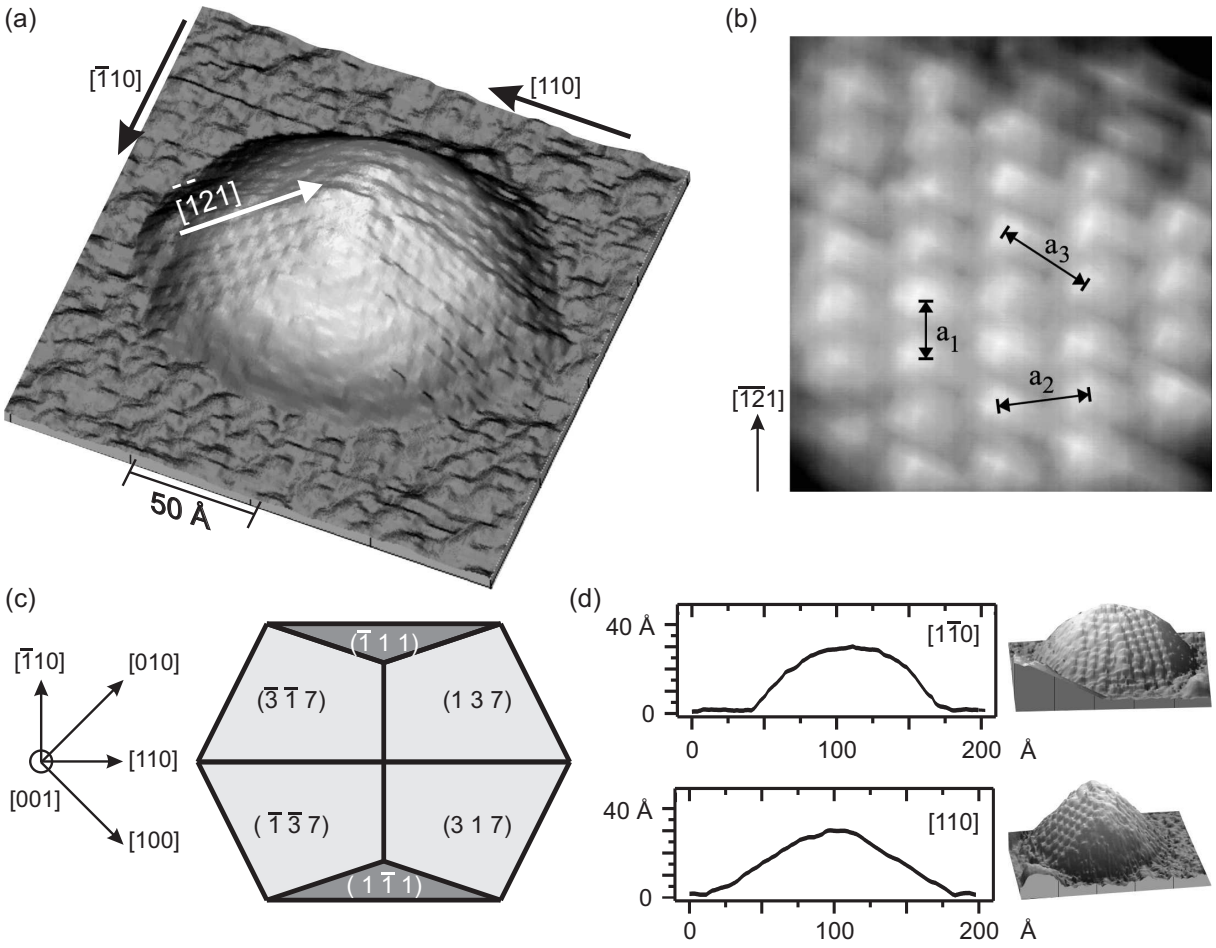

FIGURE 5.3: (a) Top-view STM image of an InAs quantum dot showing atomically resolved side facets with {137} orientation. (b) Part of the image in (a) showing the side facet in detail and (c) derived shape model [113, 127]. (d) Height profiles along the $[1\bar{1}0]$ and [110] directions. Images are taken from Refs. [49, 113].

Xu et al. [114]. Figure 5.4 presents the quantum dot evolution and the derived structural models. Small quantum dots are characterized by the four {137} side facets (a), while with increasing quantum dot size additional {$\bar{1}35$} and {$\bar{1}12$} facets develop (b−e). After a critical size steeper {110} facets start to replace the formerly flat side facets (e−g). This process continues with increasing quantum dot size, leading to large quantum dots with

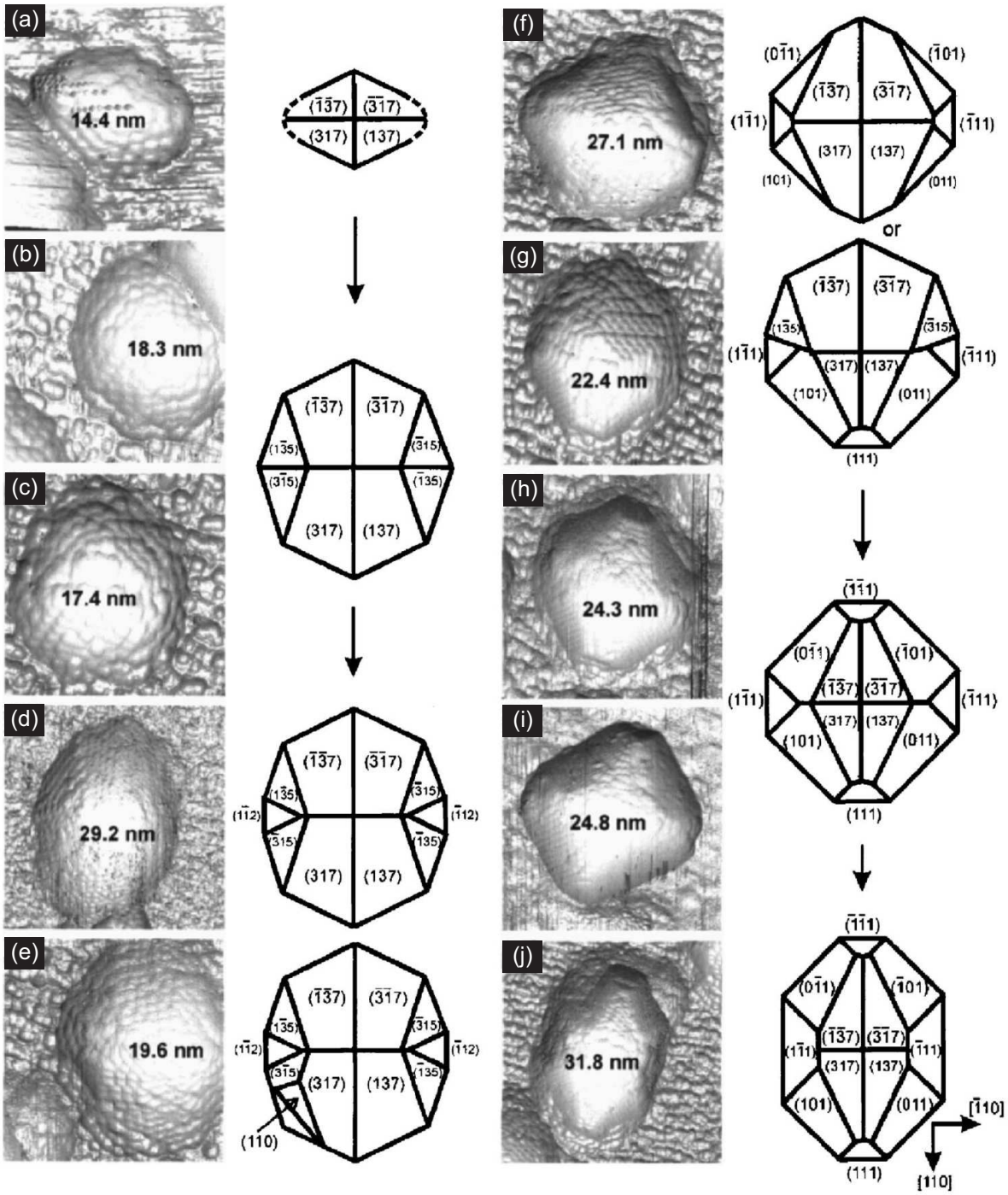

FIGURE 5.4: Top-view STM images of InAs quantum dots and their resulting structural models. (a−j) Quantum dot evolution with increasing size. The values inside the figures are the image sizes [114].

steep {101} and {$\bar{1}$11} side facets (h−j). However, one has to notice that on top of all investigated quantum dots still four {137} side facets remain (a−j), while (001) top facets are never observed.

The main mechanism leading to the shape transition is the following [114]: Quantum dot evolution starts in the Stranski-Krastanow mode. The strain energy is lowered, while the surface energy increases. As a compromise flat quantum dot shapes are formed. Growth of larger quantum dots leads to larger strain as well as to an increase in surface energy. Thus the quantum dots cannot release the strain by further lateral expansion, but by vertical growth. The corresponding steeper side facets reduce the interface area between the quantum dot base and the substrate, allowing to incorporate the larger amount of quantum dot material.

In summary quantum dot growth takes place in a shell-like mode. Small quantum dots start with a flat shape, while after a critical quantum dot diameter steeper side facets are formed at their side. Additional {137} facets on top of the quantum dot remain.

5.3 XSTM results

This section on XSTM results is divided into three parts: The first part presents the data of the first quantum dot layer in sample I (c). It contains 1.8 ML InAs grown at 450°C and is identical to sample I (a). Thus the top-view results shown above can directly be compared with the following XSTM results. The second part presents the XSTM data from samples I (c) and II, grown at the same temperature, but containing increasing InAs material amounts (2.2 ML−3.6 ML). The data of sample III, grown at slightly lower InAs growth temperature (420°C), are presented in the last part.

5.3.1 Capped InAs quantum dots

In order to investigate the influence of the overgrowth process, firstly an overview of some general image characteristics is presented, then the quantum dot density is determined. Afterwards the detailed quantum dot structure evaluation of both {110} cleavage surfaces can be compared with the above presented top-view STM results by the group of Jacobi et al. [49, 113, 120]. Finally the stoichiometry of the quantum dots and the wetting layer will be determined and discussed regarding the changes occurring during overgrowth.

Overview

Figure 5.5 (a) shows an assembly of seven overlapping XSTM images, giving an overview over the InAs wetting layer. The wetting layer is clearly visible as a bright line and at the upper end of this image assembly a single quantum dot is located. It appears with a higher contrast and is also shown in Fig. 5.5 (b) and in more detail in Fig. 5.5 (c). In the overview image some typical undesired appearances in XSTM images can be seen:

- The appearance of the wetting layer as a double line is a result of a tip artifact, which also leads to two further bright lines in the image, parallel to the atomic chains.

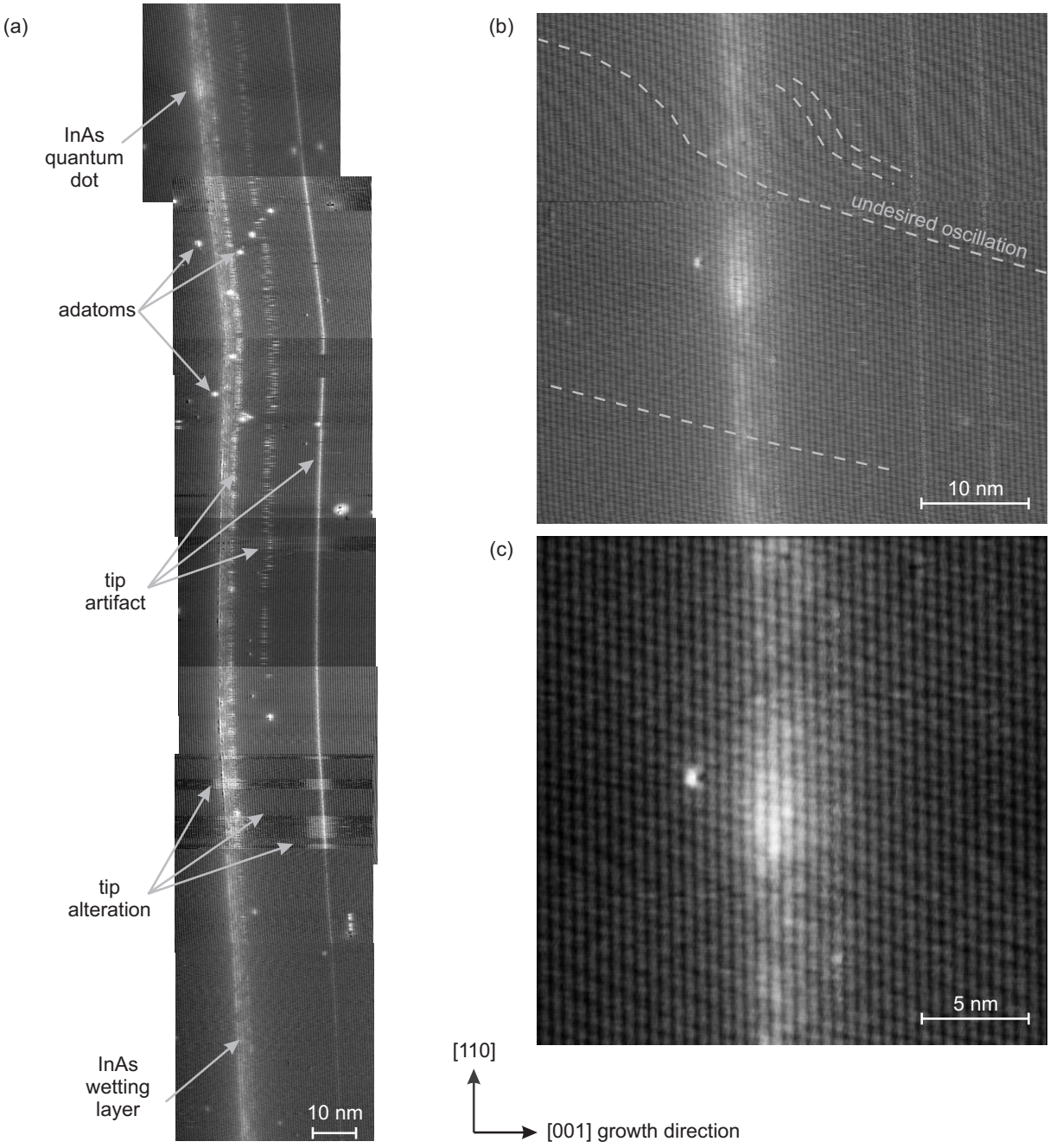

FIGURE 5.5: XSTM images of 1.8 ML InAs grown at 450°C, taken at the $(\bar{1}10)$ cleavage surface at negative sample bias between $V_S = -2.6$ and $V_S = -3.0$ V and at $I_T = 80$ pA. (a) Assembly of seven XSTM images, together extending to about 250 nm along [110] direction. The InAs wetting layer appears as a broad white stripe. At the top of the image a small quantum dot is visible. (b) The same InAs quantum dot. The image is superposed by an undesired oscillation with changing frequency. (c) Detailed and filtered XSTM image of the small indium rich quantum dot. The lines parallel to the [110] direction are the atomic chains.

- Tip alterations during the scan, leading to contrast variations parallel to the scanning direction.
- Tip artifacts due to additional adatoms at the cleavage surface. These adatoms can move along the zigzag chains due to interactions with the tip during scanning.
- Undesired oscillations as a consequence from a vibration between tip and sample. The reason for that can be a problem with the microscope vibration isolation, an unstable sample holder, or a too long and therewith easily oscillating tip. Such an oscillation in XSTM images is undesirable, but if the atomic zigzag chains perpendicular to the growth directions are still visible it is usually negligible for data analysis. An appropriate example is shown in Fig. 5.5 (b), in which the oscillation changes its frequency during the scan. Nevertheless the atomic chains parallel to the [110] direction are clearly visible.

Using assembled XSTM images such as Fig. 5.5 the quantum dot density can be calculated as described in section 4.5.2. Along the [110] direction 13 quantum dots are found within a length of 1.8 μm, and along the $[\bar{1}10]$ direction 15 quantum dots are found within 1.5 μm. For the density calculation an averaged XSTM quantum dot baselength of 12 nm is assumed, which leads to a density of about 6×10^{10} cm^{-2}.

This is more than a factor of two lower than the value observed in the top-view STM investigation, where a density of about 2×10^{11} cm^{-2} is found [113]. A reason for this discrepancy may be the following: In XSTM images also small quantum-dot like features are found, like the one shown in Fig. 5.6. The white dotted line indicates the baselength of the feature, which amounts to about 10 nm, but even smaller objects of this kind could be observed. In the image no typical quantum dot strain field is observed and therewith this object is not counted as a quantum dot, although it cannot be excluded that this may be a buried quantum dot. More probable is the evolution of a previously small quantum

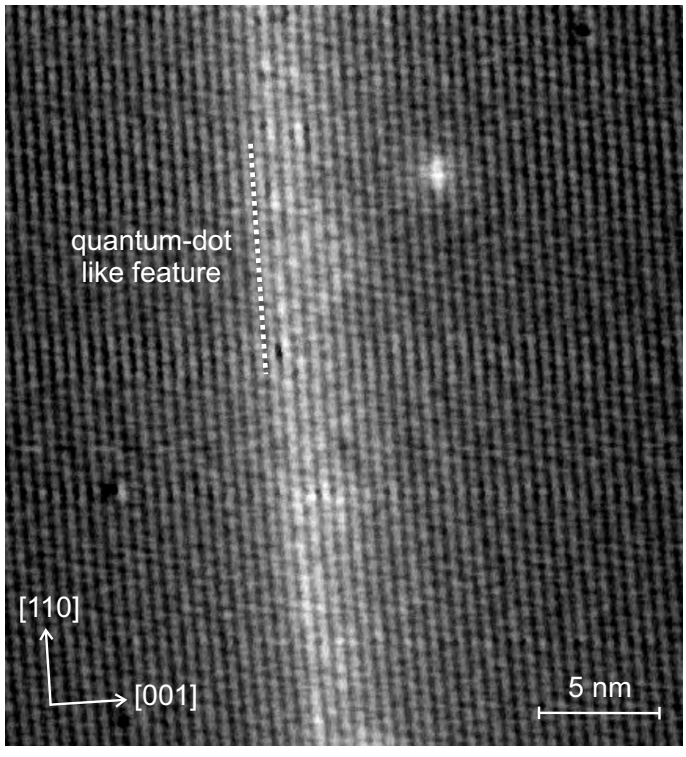

FIGURE 5.6: XSTM image of a quantum-dot like feature, taken at $V_S = -2.7$ V and $I_T = 80$ pA. The white dotted line indicates the baselength of this feature.

dot during overgrowth to such a quantum-dot like feature. This backward transformation during overgrowth is well known from the Si/Ge system, where the former large quantum dots (so-called domes) change to smaller ones called huts [128]. While doing so the germanium from the hut apex diffuses to the side facets, in this way flattening the hut. Furthermore an incorporation of silicon into the dot leads to an alloying of the island material and to a lowering of its strain. Such a quantum dot shrinking and backward shape transition has recently been observed also for the InAs/GaAs system [30].

Quantum dot size and shape

Two typical XSTM images, one for every investigated cleavage surface, are presented in Fig. 5.7. The contours of the InAs quantum dots at the $(\bar{1}10)$ surface [Fig. 5.7 (a)] and at the (110) surface [Fig. 5.7 (b)] are marked by with white dotted lines, indicating a truncated pyramidal shape. This is a typical behavior for all observed quantum dots and is in contrast to the top-view STM images, which show a non-truncated pyramidal shape. The size of the quantum dots at both cleavage directions is very similar. The height along the [001] growth direction varies between 5−6 atomic chains, which is about 3 nm, and the baselength of the observed quantum dots amounts to about 15 nm in the

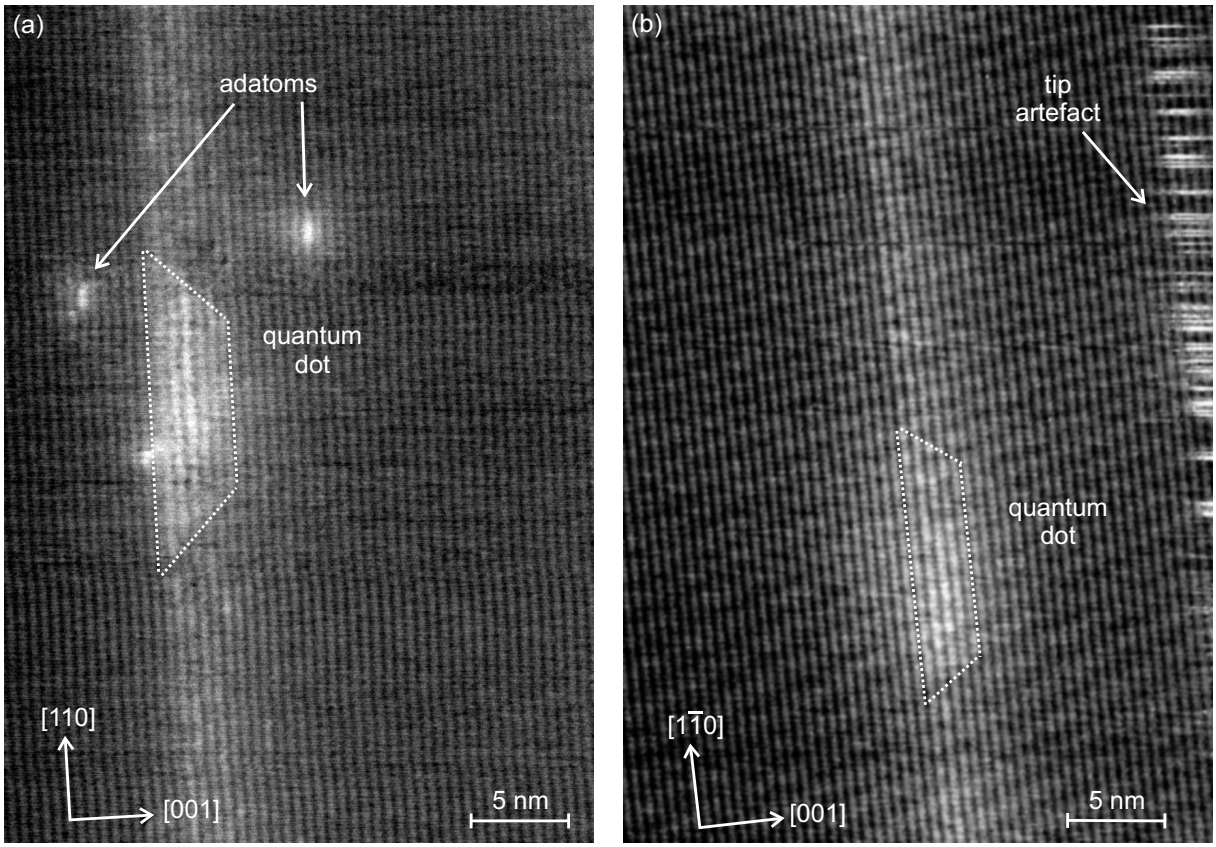

FIGURE 5.7: XSTM images taken at negative sample bias and at $I_T = 80$ pA. The white dotted lines indicate the observed contours, typical for truncated pyramidal quantum dot shapes. (a) Quantum dot observed at the $(\bar{1}10)$ cleavage surface ($V_S = -2.2$ V), and (b) quantum dot at the (110) surface ($V_S = -2.6$ V).

[110] direction (a) and to 14 nm in [$\bar{1}$10] direction (b).

The top regions of the truncated quantum dots can easily be identified as flat (001) facets for both cleavage surfaces, while the observed angles of the contours between the side facet and the baseline amount to about 45° for the quantum dot at the ($\bar{1}$10) cleavage surface and to about 53° at the (110) surface. However, it should be noted that the estimation of these angles is rather difficult, because no atomic resolution perpendicular to the [001] growth direction could be determined. Nevertheless it is clearly visible that the side facets are much steeper than the {137} facet, whose characteristic angles between the side contour line and the baseline amount to 22.0° and 11.4° for the ($\bar{1}$10) and (110) cleavage surfaces, respectively (see Fig. 4.6).

This change of the quantum dot shape during capping can also be seen at all other quantum dots, e.g. the ones shown in Fig. 5.8. The image of Fig. 5.8 (b) is taken at positive sample bias. Thus, mainly the group-III atoms are visible, leading to a strong chemical contrast, as explained in section 4.4. For each cleavage surface one quantum dot is shown in the upper images with expected nominal contours corresponding to different side facets [(a), (b)], and in the lower images with the experimentally observed contour of the quantum dot [(c), (d)], indicated by the white dotted lines, respectively. It is clearly visible that the {137} side facet (yellow), which is characteristic for the uncapped dots, is by far too flat, and that the previously pyramidal quantum dot changed to a truncated pyramidal shape. The observed side facets are considerably steeper than the {137} facet, and the angle of the contours can be estimated to about 35° for the quantum dot at the ($\bar{1}$10) cleavage surface and to about 43° at the (110) surface. Both are close to the expected values of the {101} facets (35.3°) and {111} facets (54.7°), taking into account the uncertainty due to the non-existing atomic resolution perpendicular to the growth direction as well as the inhomogeneous stoichiometry.

The height of the quantum dots in Fig. 5.8 amounts to 2−3 nm for both cleavage planes. Their baselength amounts to about 17 nm along [110] direction and 15 nm along the [$\bar{1}$10] direction, while from top-view STM images 14 nm (along [110]) and 13 nm (along [$\bar{1}$10]) were found. In contrast to top-view STM, where only the quantum dot size on top of the wetting layer can be determined, XSTM images also involve the part below the wetting layer. Thus the determined baselength of the quantum dot in XSTM is rather the extrapolation down to the wetting layer baseline, and consequently the observed slightly larger quantum dot sizes are well expected. In addition, the largest observed quantum dots in all XSTM images for each cleavage plane, as shown in Figs. 5.8 and 5.9, may be assumed to be cleaved almost through their center.

Figure 5.9 shows the expected XSTM contour lines of the InAs quantum dots investigated here, assuming that their shape does not change during capping. The left side of the image shows the situation for the ($\bar{1}$10) cleavage surface. The shape model derived from top-view images like those of Fig. 5.3 [113, 127] is shown in Fig. 5.9 (a). The expected XSTM contours are drawn for the case of a cut through the dot center as well as for more off-axis cuts (b), characterized by an angle between the contour line from the {137} side

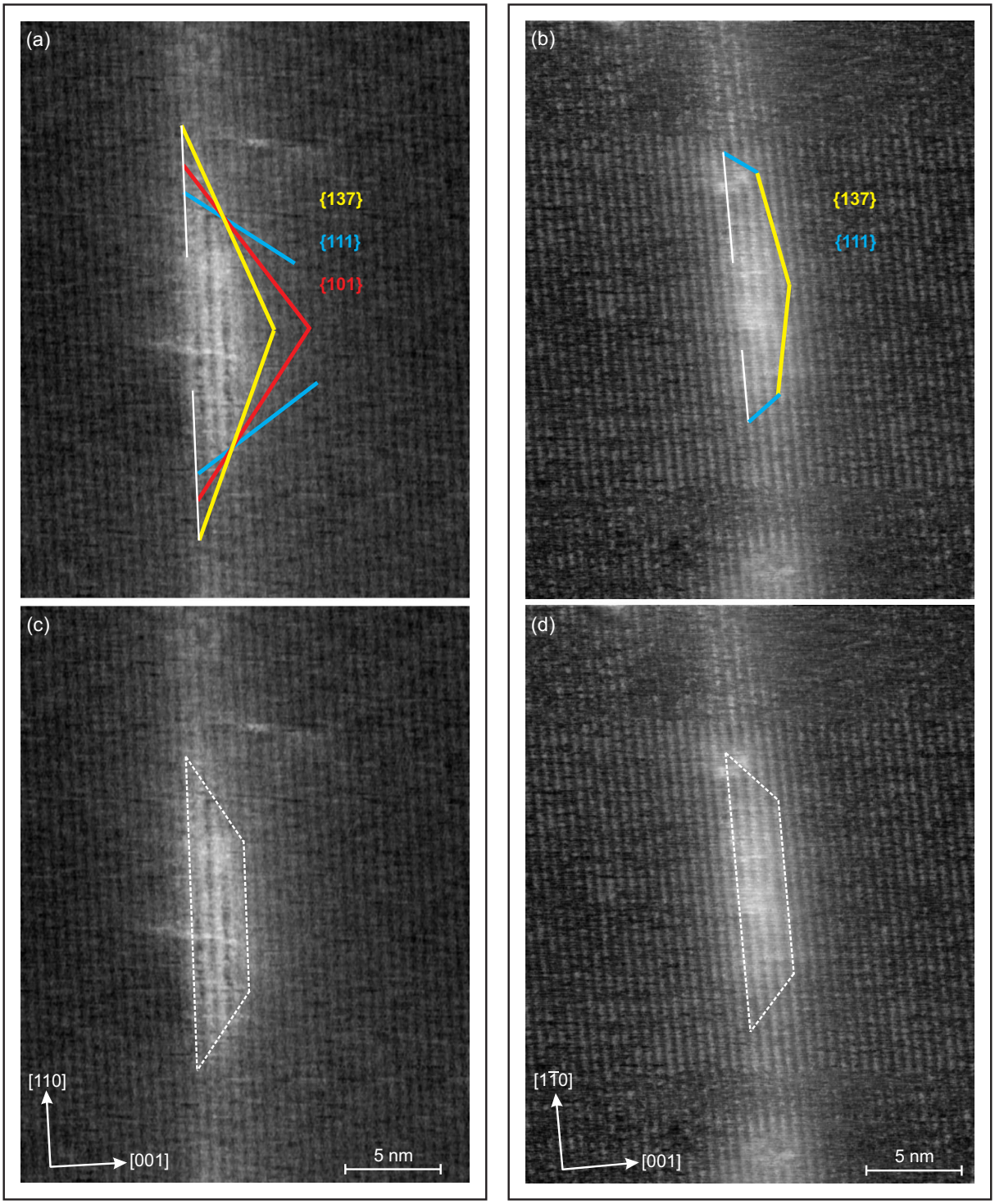

FIGURE 5.8: XSTM images, taken at $I_T = 80$ pA of (a, c) a quantum dot at the $(\bar{1}10)$ surface ($V_S = -3.0$ V) and (b, d) a quantum dot at the (110) surface ($V_S = +2.0$ V). The same images are shown with nominal contours (colored lines) of different side facets (a, b) and with the estimated actual contours (c, d), indicated by the white dashed line. Facets steeper than the {137} fit much better, and a (001) truncation of the quantum dot shape is clearly visible for both cleavage surfaces.

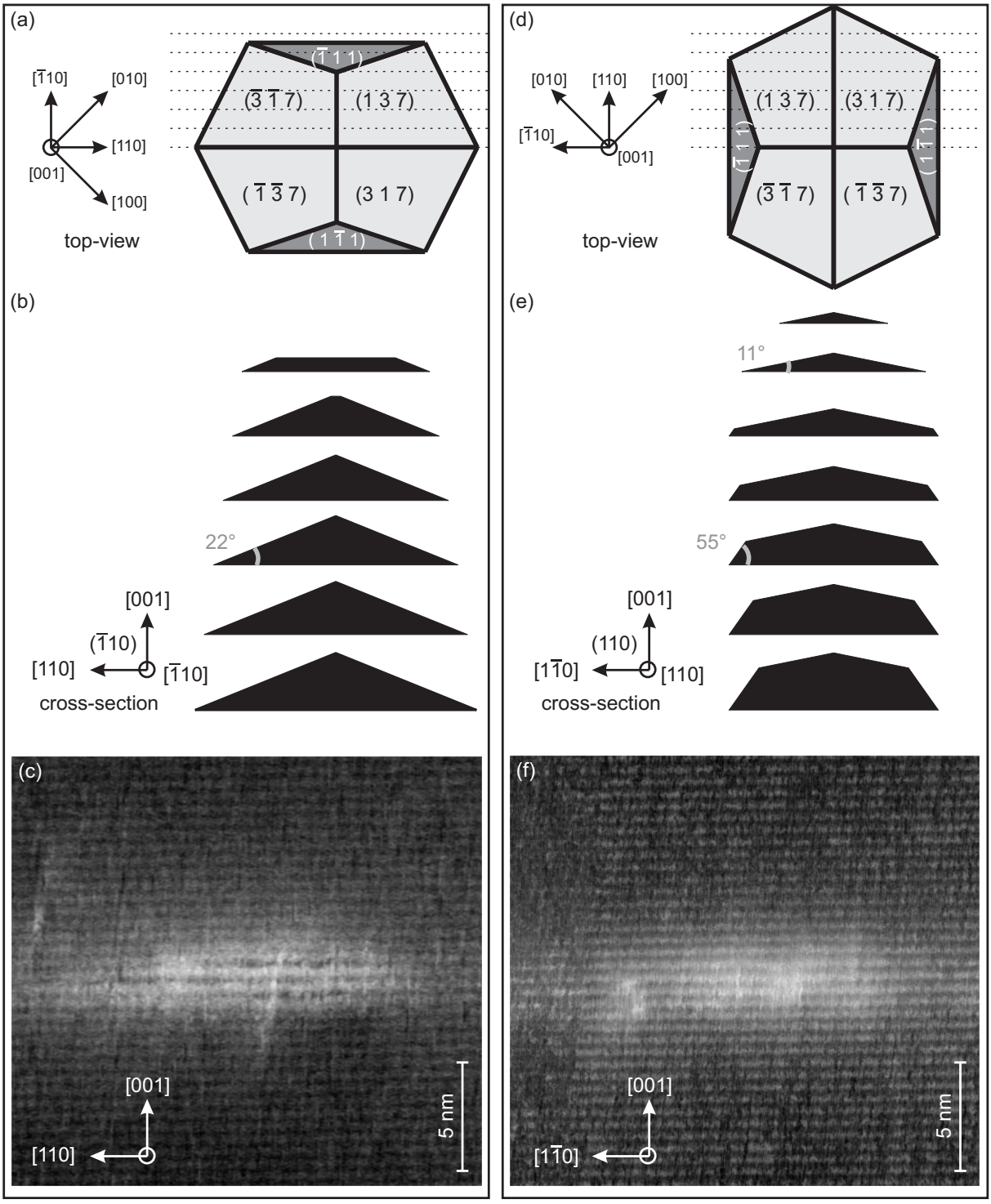

FIGURE 5.9: (a, d) Shape model after Refs. [113, 127], derived from top-view STM images as shown in Fig. 5.3, resulting in (b, e) the expected cross-sections plotted for the ($\bar{1}$10) and (110) cleavage surface, after cutting the dots shown in (a) and (d) at the positions indicated by the dashed lines. The angle between the baseline and the nominal contour of the {137} side facet amounts to 22.0° for the ($\bar{1}$10) cleavage surface to and to 11.4° for the (110) surface. (c, f) XSTM images for the ($\bar{1}$10) and (110) surface, demonstrating no agreement with the expected shapes.

facet and the baseline of 22°. The positions of the cross-sections are indicated in (a) by the dashed lines. In (c) the XSTM image of Fig. 5.8 is plotted again for comparison with the expected shapes. As mentioned above, the imaged quantum dot is cut almost through its center, so a triangular quantum dot shape is expected, according to Fig. 5.9 (b). It is obvious that the observed shape is not triangular.

For the (110) cleavage surface a similar situation is observed, as shown on the right side of Fig. 5.9. The expected contours along the dashed lines in (d) are plotted in (e). The XSTM image shown in Fig. 5.9 (f) is also cleaved next to its center, so we expect a contour with a pentagonal shape, characterized by steep {111} side facets and two additional {137} side facets on the top, with angles towards the baseline of 55° and 11°. Comparing the expected shape with the measured one, again no agreement is found.

In conclusion, pyramidal quantum dot shapes were always found with top-view STM, as shown in section 5.1, while in XSTM images all quantum dots show a flat {001} top facet and steeper side facets. Thus the shape of the quantum dots changes considerably during capping.

Stoichiometry

Information on the indium content in a quantum dot cannot be derived from top-view STM investigations, but it is important to know the incorporated amount of indium for understanding the growth and capping process. Moreover, for the calculation of the electronic properties the correct indium distribution in the quantum dot has to be known [24, 25, 129].

Figure 5.10 shows the stoichiometry determination of an atomically resolved quantum dot at the $(\bar{1}10)$ surface along the colored boxes, as explained in section 4.5.3. The evaluated variation of atomic chain distances within each box is presented in Fig. 5.10 (b) by the symbols with the respective colors. The results of the local stoichiometry for the three stripes vary only slightly. The highest indium content can be observed in the middle stripe (yellow), and thus in the quantum dot center. The black curve is the averaged stoichiometry over all three boxes and therewith over practically the whole quantum dot. From this curve a maximum indium content of up to 90% is derived, taking the compressive strain in the quantum dot and the surface bending into account. The clearly visible undershoot of the indium concentration underneath the quantum dot baseline shows the strong compressive strain at the quantum dot. At the top of the quantum dot such a compression is also visible, but much less pronounced. This behavior can be attributed to the strain in the system, which is larger at the wider quantum dot base than at its narrow top and probably also to segregation effects during capping and quantum dot truncation, leading to diluted indium above the dot.

A second stoichiometry determination of a quantum dot, in this case investigated at the (110) surface, is shown in Fig. 5.11. The maximum indium content amounts to 55%−65%. The calculation of the stoichiometry in this image was more difficult because of the lower resolution. This is manifested by the apparent fluctuation of the GaAs chain

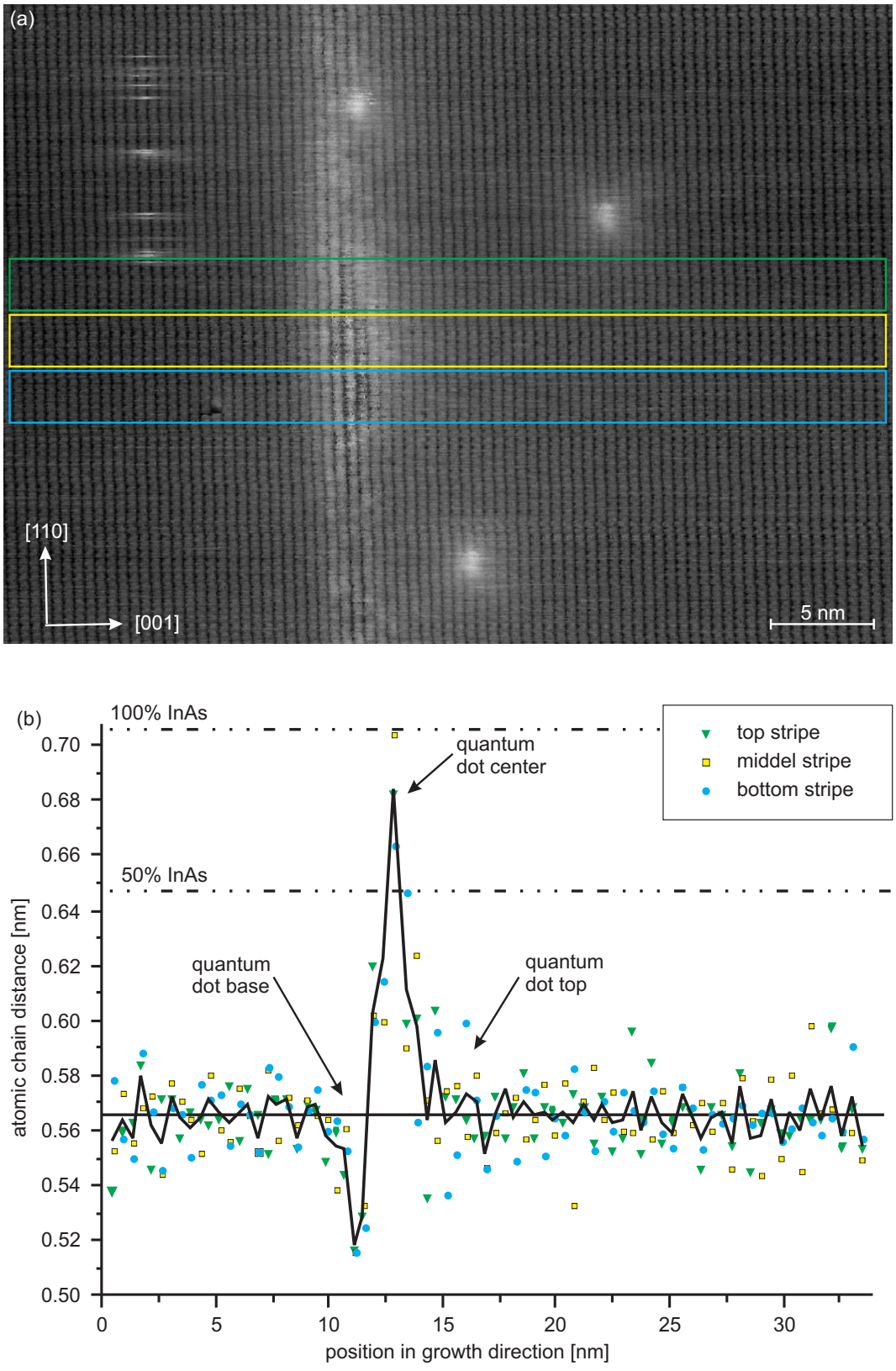

FIGURE 5.10: (a) XSTM image of a quantum dot at the $(\bar{1}10)$ surface, taken at $I_T = 80$ pA and $V_S = -1.8$ V. (b) Result of the local stoichiometry evaluation. The colored symbols belong to the three investigated stripes, indicated by the respectively colored boxes in (a). The dashed-dotted lines indicate the calculated chain distances from InGaAs layers with different indium content. The black curve represents the averaged stoichiometry over the whole quantum dot, leading to a maximum indium content of up to 90%.

distances value, which is larger than in Fig. 5.10 (b). Thus, the determination of the stoichiometry has an uncertainty amounting to about 15% in this case. For this quantum dot only a small compression is found [Figure 5.11 (b)], which confirms that the quantum dot contains less indium and is therewith also less strained.

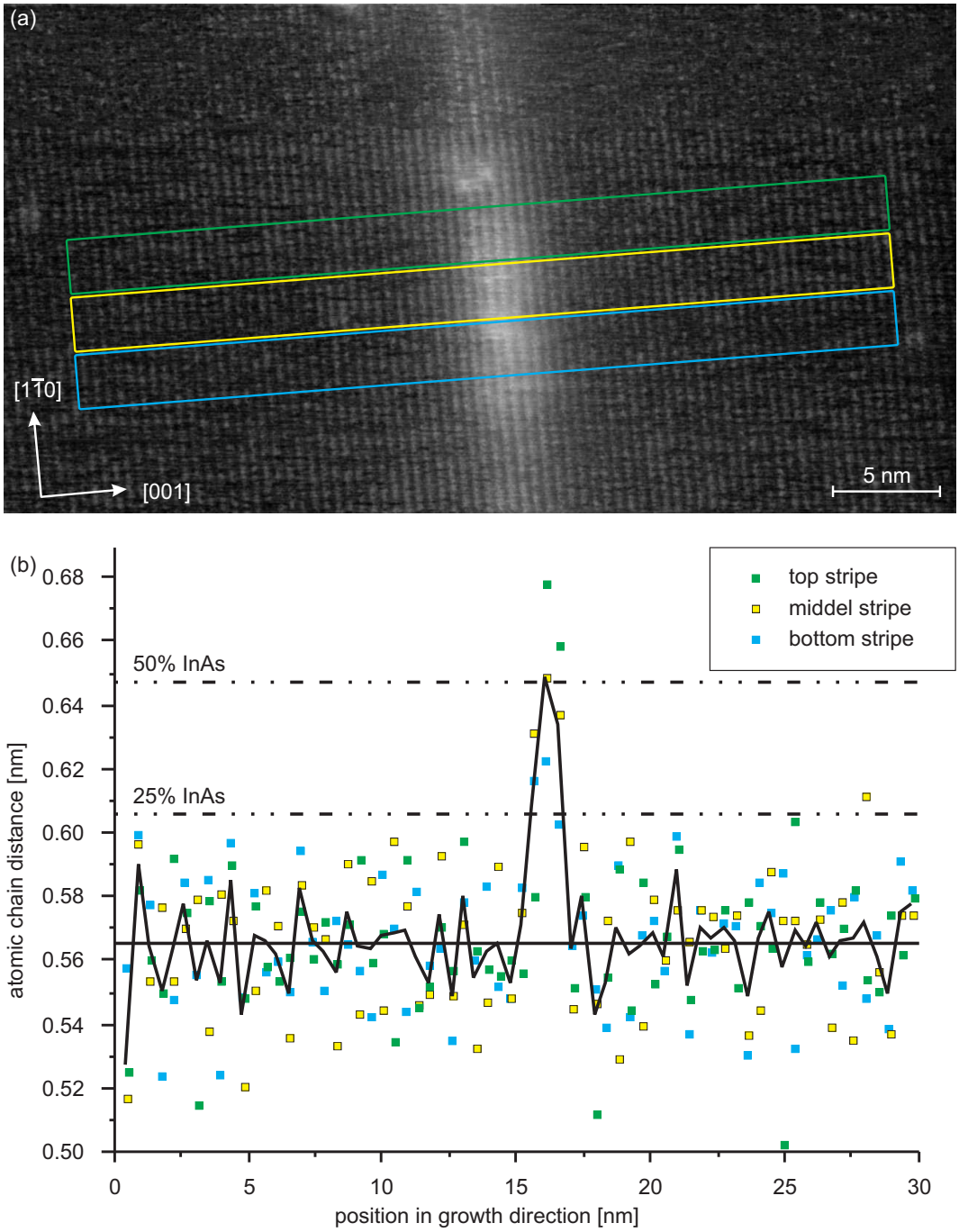

FIGURE 5.11: (a) XSTM image of a quantum dot at the (110) surface, taken at $I_T = 80$ pA and $V_S = +2.0$ V. (b) Result of the local stoichiometry evaluation. The colored symbols belong to the three investigated stripes, indicated by the respectively colored boxes in (a). The black curve represents the averaged stoichiometry over the whole quantum dot, leading to an maximum indium content of up to 55%−65%.

These two examples represent typical values of the maximum indium content. In all investigated quantum dots a variation between 55% and 90% was found, but more than one half contains a maximum indium content of about 80%. The determination of the indium distribution in the quantum dots appears to be rather complicated due to the small quantum dot heights. Considering the shapes of the averaged stoichiometry in Figs. 5.10 and 5.11 the maximum indium content seems to be located slightly above the quantum dot baseline. Furthermore, in the quantum dot image shown in Fig. 5.10 (a) unusual dark depression lines in the quantum dot center are visible, which may be connected to the high indium content in the center, leading to a bending of the atomic positions. If the distances between the atoms in the quantum dot center are slightly larger this could be imaged by the tip as a local dip in the height profile, explaining such depression lines.

A more detailed investigation on the indium distribution can be performed on the larger quantum dots and will thus be presented in the next section.

In addition, the stoichiometry determination of the wetting layer leads to a maximum indium content of about 30% near its base, as shown in Fig. 5.12. The cyan curve is the averaged stoichiometry along the box shown in the XSTM image of the inset. From the stoichiometry profile further a wetting layer thickness of about 3 nm is derived. In general the thickness varies between 3 and 4 nm, with an maximum indium content of 25% to 30% near the base, decreasing exponentially along growth direction.

Thus the stoichiometry determinations of the quantum dots leads to a reduced indium content compared to the uncapped case, and in the wetting layer strong segregation effects can be observed. Both results show that besides changes of the quantum dot shape also the stoichiometry and its distribution changes during overgrowth.

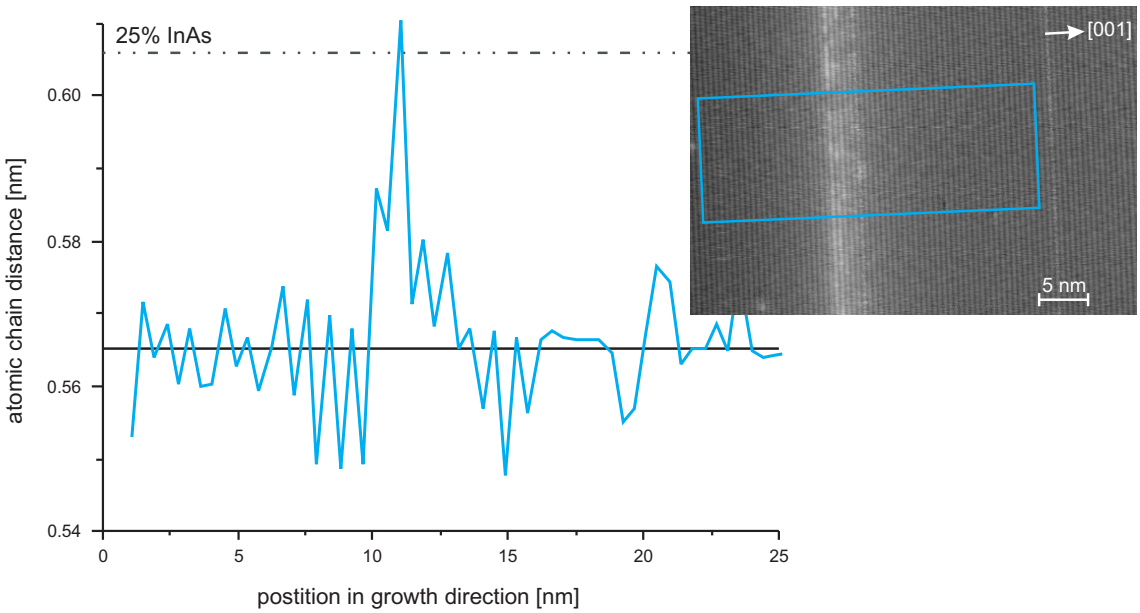

FIGURE 5.12: Local stoichiometry evaluation of the wetting layer indicated by the box shown in the XSTM inset image. The cyan curve represents the averaged stoichiometry, which amounts to about 30%.

5.3.2 Increasing amount of InAs deposition

In order to investigate if the structural changes are connected to special growth parameters, this section presents the XSTM data of the samples grown as well at 450°C, but containing increasing amounts of indium material. All XSTM images are taken at the $(\bar{1}10)$ surface, so that the expected angle between the contour of the {137} side facet of the structural unchanged quantum dot and the baseline amounts to 22°, as shown in Fig. 5.9.

Images from layers containing 1.8 ML, 2.2 ML, and 2.6 ML InAs were taken at sample I (c) (see Fig. 5.1), while the additional layers with 3.0 ML and 3.6 ML could not be examined in sample I (c), because at all measured positions these two layers were located at surface steps. A layer containing 3.6 ML InAs could be studied in sample II instead. For simplicity all layers are labeled layer 1.8, layer 2.2, layer 2.6, and layer 3.6 in the following, regarding their nominal amount of InAs MLs.

In Figure 5.13 two XSTM images show the layers 1.8, 2.2, and 2.6. In the upper image quantum dots are visible at layers 1.8 and 2.6, imaged with an unusual contrast indicated by the dark depressions. This may be connected to the high indium content in

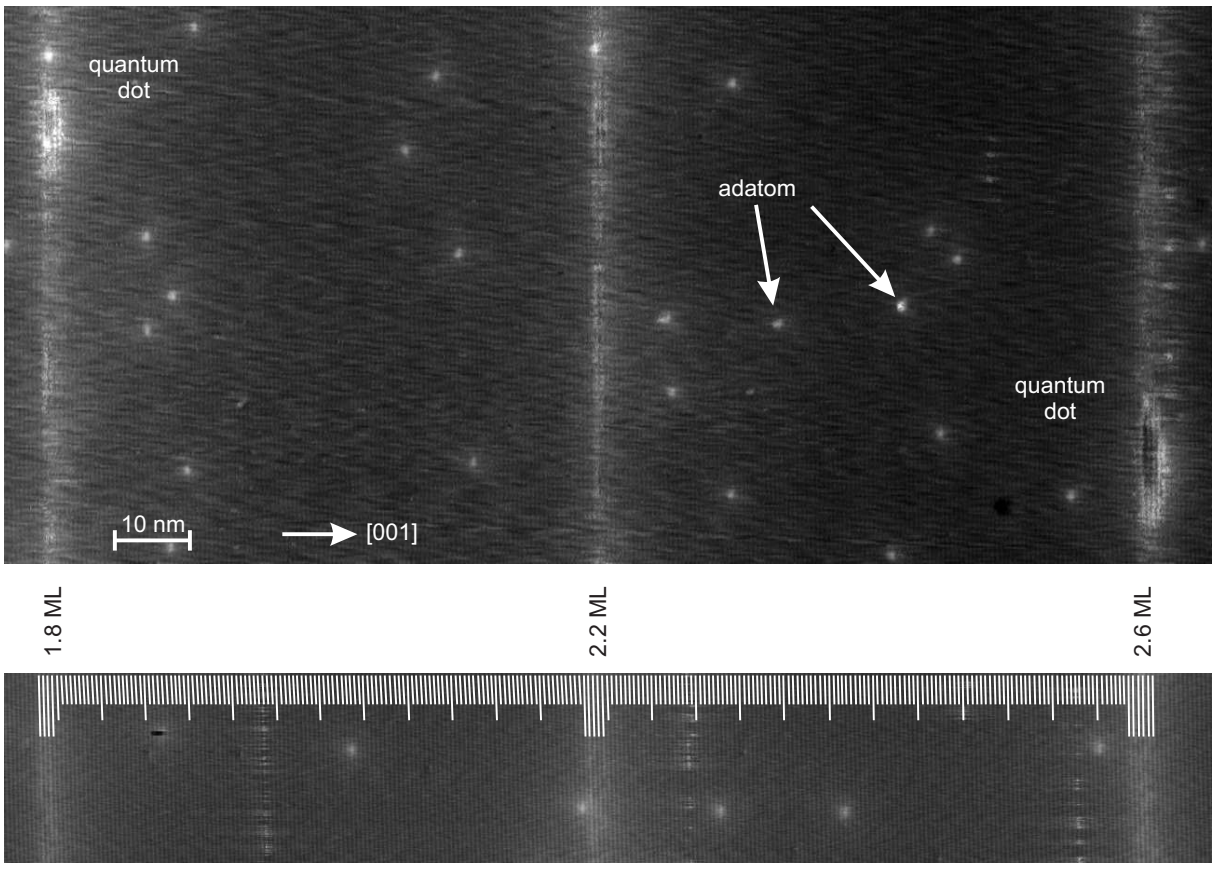

FIGURE 5.13: XSTM overview images of the layers 1.8, 2.2, and 2.6, taken at $I_T = 80$ pA. In the upper image ($V_S = -1.8$ V) quantum dots are visible in layer 1.8 and 2.6. In the lower XSTM image ($V_S = -2.0$ V) the positions of the atomic chains are indicated by the white lines in order to determine the thickness of the spacer layers and the wetting layers.

the quantum dots as discussed above for Fig. 5.10. The higher number of adatoms imaged here is due to the fact that the image is taken after several days after sample cleavage.

At layer 2.2 twelve quantum dots are found within 2.6 μm with an averaged baselength of about 17 nm, which leads to a quantum dot density of about 2.2 $\times$ 10^{10} cm^{-2}. The quantum dots imaged at layer 2.6 have an averaged baselength of 19 nm and a density of about 2.0 $\times$ 10^{10} cm^{-2}, while the averaged baselength of the quantum dots grown with 3.6 ML InAs amounts 22 nm and the density to about 1.5 $\times$ 10^{10} cm^{-2} (see table 5.1, page 69). Thus we found that with increasing indium content from 1.8 ML to 3.6 ML the averaged baselength of the quantum dot increases from about 12 nm to 22 nm and the density decreases from 6 $\times$ 10^{10} cm^{-2} to 1.5 $\times$ 10^{10} cm^{-2}. Such an increase of the average InAs quantum dot size [130] and decrease of the quantum dot density upon increasing material deposition is well known from the attempt to grow larger InAs quantum dots for longer lasing wavelengths [54, 131]. Similar observations have also been reported from experiments with varying growth rates. In the case of a high deposition rate STM investigations result in high quantum dot densities, while for the lower deposition rate the density decreases and the size of the quantum dots increases [132].

In the lower XSTM image of Fig. 5.13 the atomic chains can be seen excellently over the whole image, so it is possible to determine the thickness of the wetting layer and the spacer layers with an accuracy of one ML. For the wetting layers increasing thicknesses of four, five, and six atomic chains are derived. The imaged spacer between layer 1.8 and 2.2 amounts to 119 atomic chains or 67.3 nm, and the spacer between layer 2.2 and 2.6 to 116 chains or 65.6 nm. Regarding the nominal growth parameters shown in Fig. 5.1, a significantly larger spacer thickness of 100 nm was intended. The discrepancy may be caused by an imprecise calibration, as further discussed in section 5.3.3. However, this comparison shows that with XSTM also such structural parameters can be determined very precisely, so that this technique is useful also for the calibration of growth rates.

Layer 2.2

A high resolution image of a quantum dot at layer 2.2 is shown in Fig. 5.14. The original distortion of the XSTM image is compensated as explained in section 4.5.2, so that shape and size can be determined with high accuracy. In the filtered image of Fig. 5.14 (a) the atomic chains in both directions are indicated by white lines. The size of the quantum dot baseline amounts to 56 chains or 22.4 nm, and the height amounts to 7 chains or 4.0 nm, representing one of the largest observed quantum dots at layer 2.2. In order to pronounce the side facets, Fig. 5.14 (b) and (c) shows a relief map of the image, emphasizing the height-contours by a specific illumination. The dashed lines in (c) represent contours related to the {137} facet (yellow) and a slightly steeper side facet with about 29° (white) agreeing better with the data. At the $(\bar{1}10)$ surface this angle could belong e.g. to the {124} facet with 27.9° or to the {135} facet with 29.5°, as listed in Fig. 4.6.

From the top-view STM results of Xu et al. [114] (shown in Fig. 5.4) the {135} facets were determined as additional facets to the larger {137} top facets. Thus it would be

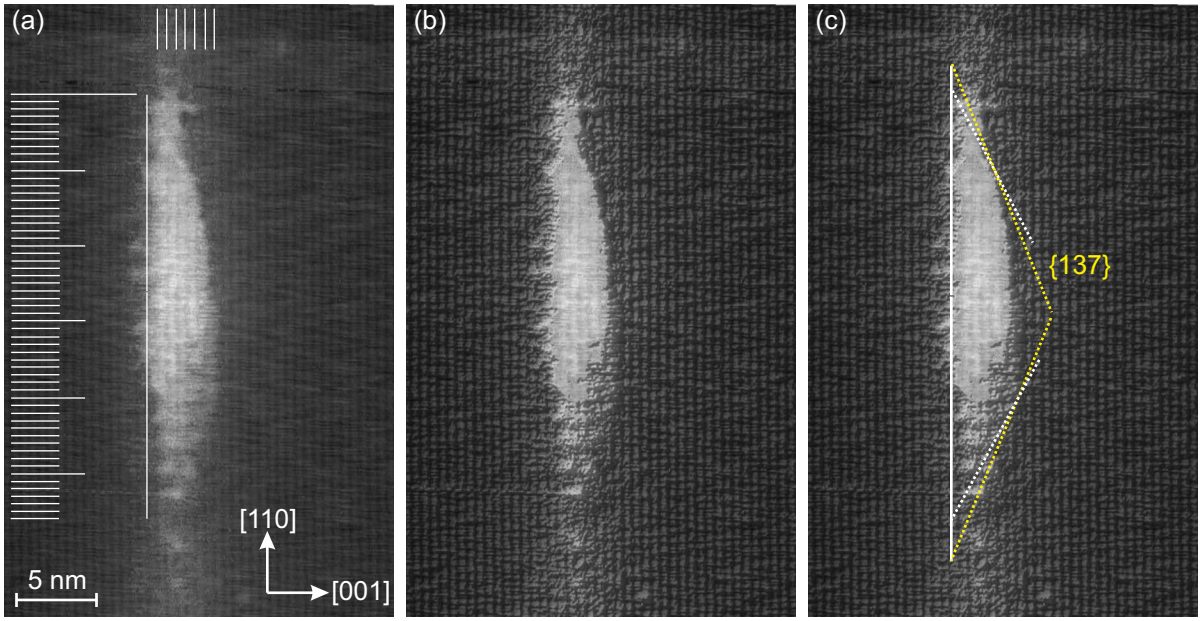

FIGURE 5.14: Undistorted XSTM image of a quantum dot at layer 2.2, taken at $I_T = 80$ pA and $V_S = -3.0$ V. (a) Filtered image with lines indicating the atomic chains in both directions. The size of the baselength and the height of the quantum dot can be determined precisely. (c, d) Relief map image in order to pronounce the side facets of the quantum dot, in (d) including possible contour lines of the side facets, indicated by dotted lines.

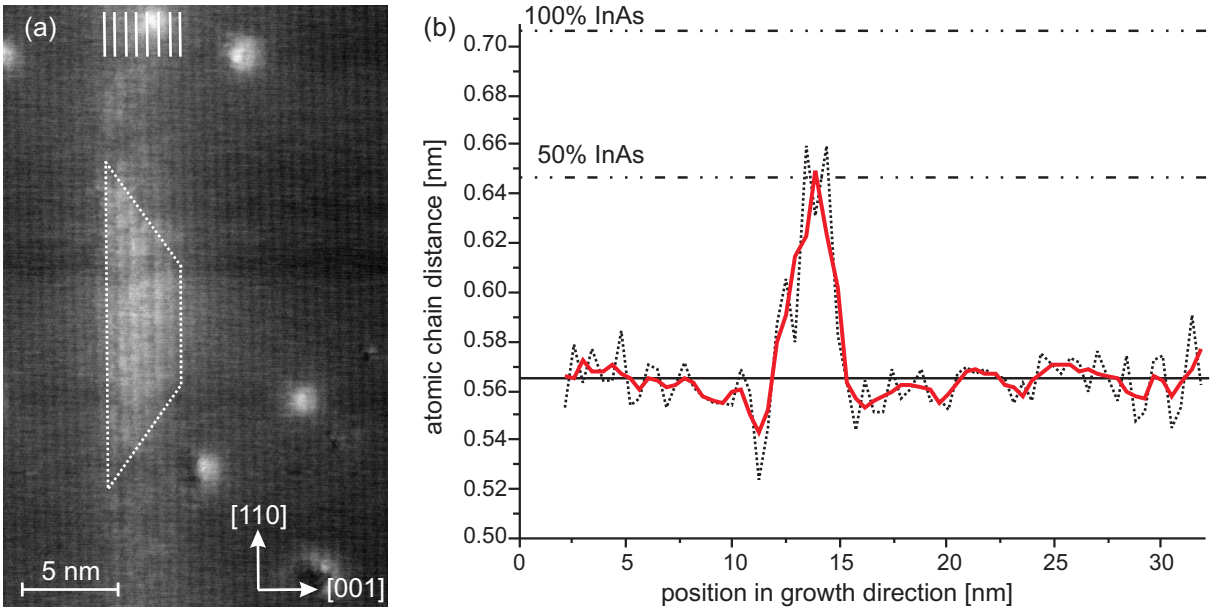

FIGURE 5.15: (a) Filtered XSTM image of a quantum dot at layer 2.2, taken at $I_T = 70$ pA and $V_S = -2.1$ V. A possible quantum dot shape is indicated by the dotted contour lines. (b) Stoichiometry profile of this quantum dot, showing a maximum indium content of about 70%.

expected that in XSTM images of the $(\bar{1}10)$ surface, cuts through the quantum dot center are characterized by {137} side facets and only in the case of more off-axis cuts by {135} side facets. Since a large quantum dot is investigated in Fig. 5.14, a cut through the quantum dot center can be assumed. Thus the observation of side facets steeper than

the {137} side facet indicates changes during overgrowth, in addition to the truncated quantum dot shape, which is in contrast to the top-view STM results [114].

Such a truncation is also found for smaller quantum dots, as shown in Fig. 5.15 (a). The baselength of this quantum dot at layer 2.2 amounts to about 17 nm and the height to about 4 nm. The possible quantum dot shape is indicated by the dotted lines. The angle of the contour lines between the side facets and the baseline is about 36° and could belong to either the {101} or the {112} side facet, which both have a corresponding angle of 35.3°. The {101} facet is an often observed facet [30, 113, 114, 133, 134], and is also used in theoretical calculations [17, 29, 40, 46, 135]. In comparison with the top-view results of Xu et al. presented in Fig. 5.4, especially for those smaller quantum dots flat {137} side facets were expected along the [110] direction, demonstrating a structural change towards truncated quantum dot shapes with steeper sides.

The local stoichiometry determination of this quantum dot [Fig. 5.15 (b)], is performed under consideration of two height profiles taken from two different XSTM images of the same quantum dot region in order to reduce noise. The black dotted curve represents the averaged data of both height profile results and the red data shows the result of an additional three-point averaging. Taking the distinctive undershoot at the quantum dot baseline into account a maximum indium amount of about 70% is concluded. From the profile of the three-point average curve one can see that the amount of indium increases gradually from the baseline to the center of the quantum dot. The highest indium amount is located in the quantum dot center, or even slightly higher. Considering the observed indium distribution of the quantum dots prepared with 1.8 ML InAs with a maximum slightly above the baseline (section 5.3.1), a tendency of the indium distribution towards the upper part of the quantum dots can be concluded. This behavior is known as "reversed cone" indium distribution [116, 117, 136] and will be discussed in detail in section 7.1.3.

An even higher maximum amount of indium with up to 90% is found for the quantum dot shown in the XSTM inset in Fig. 5.16. The determination of the indium content is again performed by averaging the results of two XSTM images of the same quantum dot

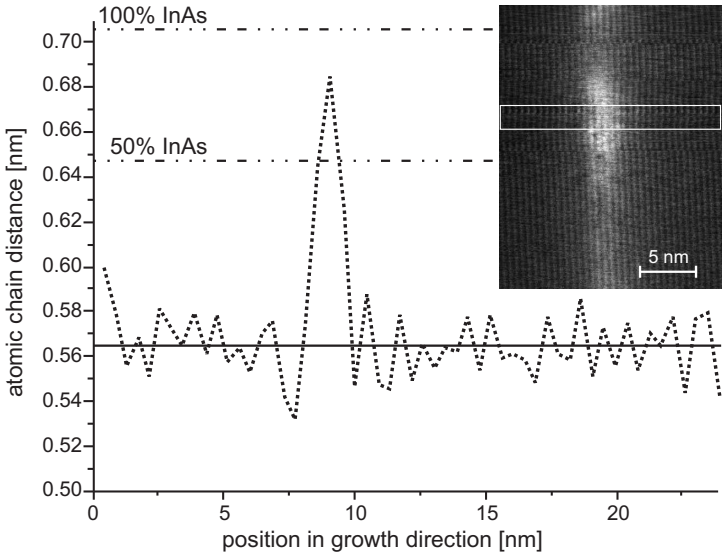

FIGURE 5.16: Local stoichiometry determination of a quantum dot at layer 2.2. The black dotted curve presents the averaged stoichiometry of two height profiles of the same region, indicated by the white box in the XSTM inset image. The averaged stoichiometry reaches up to 90%.

region. With up to 90% indium content this quantum dot represents the upper limit of all investigated quantum dots at layer 2.2, where the observed maximum content varies between 70 and 90%.

Layer 2.6

For the analysis of layer 2.6 only three quantum dots could be taken into account, so it should be noted that all conclusions can only be done under consideration of a higher statistical error. Figure 5.17 shows a filtered XSTM image (a) of a quantum dot at layer 2.6 and the relief map image (b) of the same quantum dot, including the possible truncated shape indicated by the dotted contour lines. The angle of the contour lines amounts to about 36° and could belong to {101} or to {112} side facets, as mentioned before. The height of the quantum dot is about 3−4 nm and the baselength about 20−22 nm. From the images can be seen that the indium concentration is higher at the dot center and less at the quantum dot bottom sides. This is due to the strain in the system, which is higher at the quantum dot edges than at its top [46, 137]. Thus during the overgrowth especially at the strained edges strong segregation effects will take place, reducing the local strain and leading to the observed indium dilution.

The baselength of a further investigated quantum dot at layer 2.6 amounts to about 21 nm and the height to about 3.4 nm (Fig. 5.18). Figure 5.18 (a) shows the filtered XSTM image, and the relief map image (b) is presented with the possible shape indicated by dotted contour lines. The measured angle amounting to about 34° could again belong to {101} or to {112} side facets.

The results of the local stoichiometry determination of this quantum dot are presented in Fig. 5.18 (c). In the image the results of four height contours of four different images of the same quantum dot are shown. The colored curves correspond to individual results of each height contour, differing in the maximum indium content due to limitations in resolution. For better statistics the black dotted curve presents the average of all four

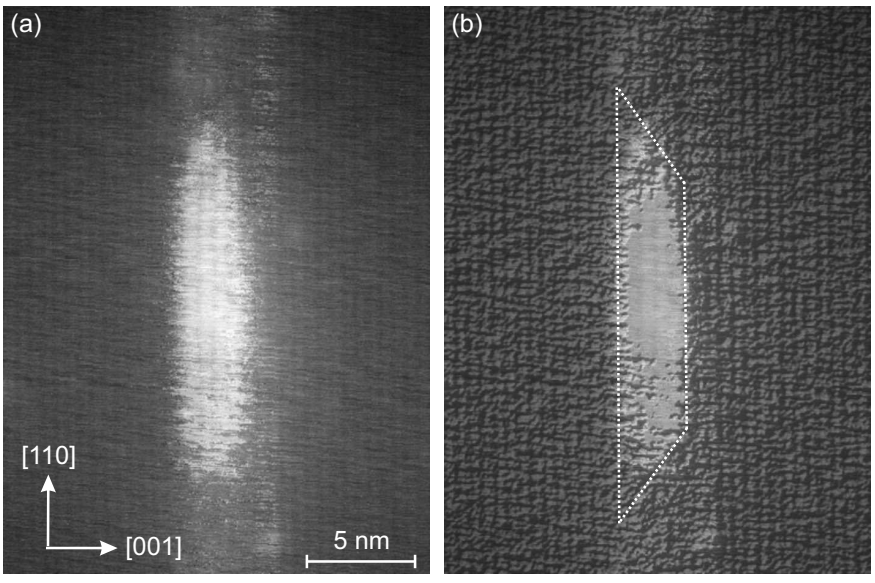

FIGURE 5.17: (a) Filtered XSTM image and (b) relief map image of a quantum dot at layer 2.6, taken at $I_T = 80$ pA and $V_S = -2.4$ V. The possible quantum dot shape is indicated by the dotted contour line.

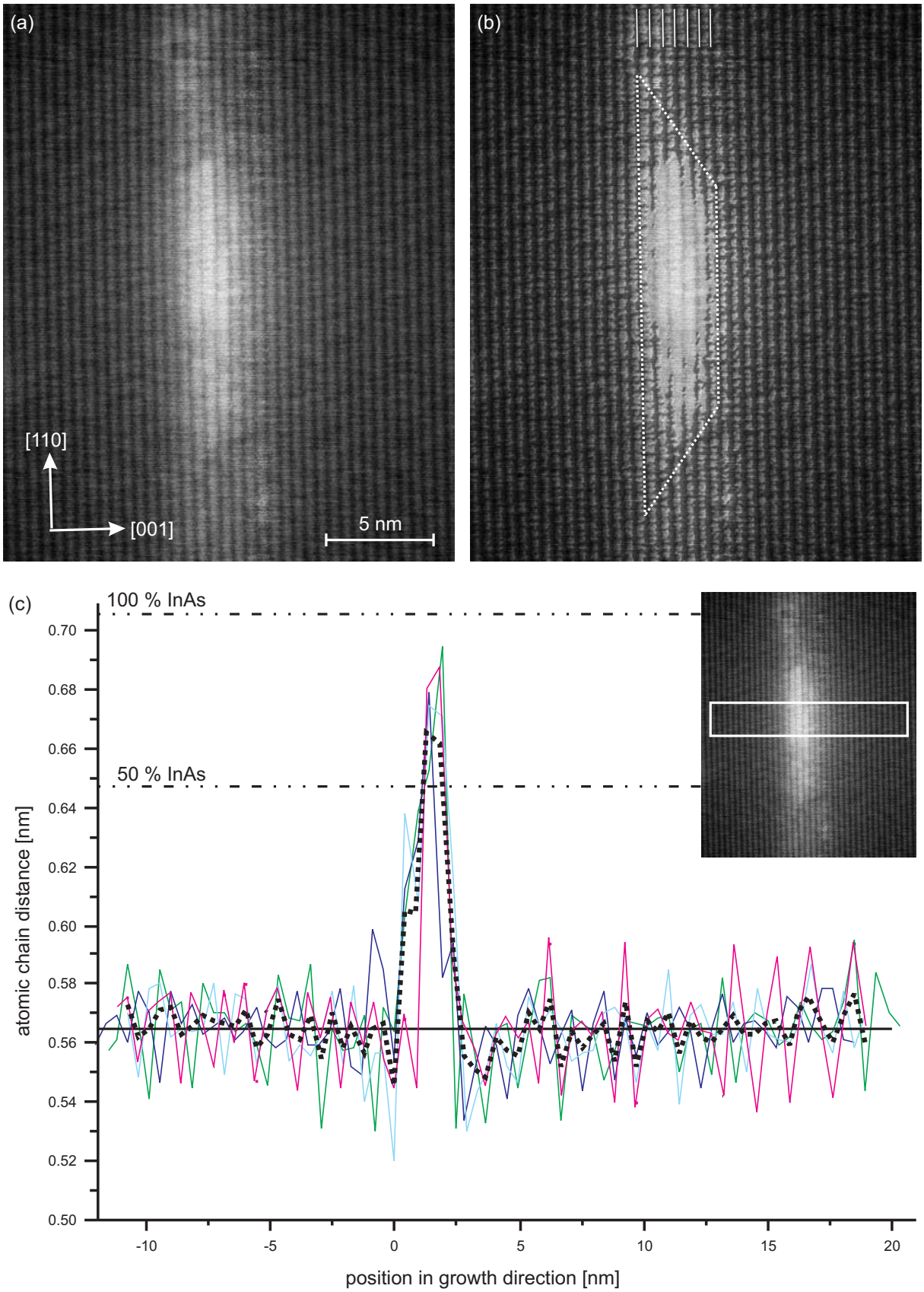

FIGURE 5.18: (a) Filtered XSTM images and (b) relief map images of a quantum dot at layer 2.6, taken at $I_T = 80$ pA and $V_S = -2.6$ V. The possible quantum dot shape is indicated by the dotted contour line. (c) Result of the local stoichiometry determination of this quantum dot. The colored curves represent the results from different images of the same region, indicated by the white box in the XSTM inset image. The black dotted curve is the averaged stoichiometry, which amounts about 75%.

curves, indicating a total maximum indium content of about 75%. Furthermore, in the stoichiometry profiles of this quantum dot the typical undershoot for such a strained system cannot be seen, indicating a cut through the quantum dot in such a way, that only about 20% of it remains in the investigated part of the sample. Thus strain relaxation has only a minor influence in the contrast mechanisms and the stoichiometry determination of this quantum dot [97]. The stoichiometry profile further shows that the highest amount of indium is located at the top of the quantum dot, and from the XSTM image it can be seen that the indium is less concentrated at the quantum dot edges, which again supports the above mentioned reversed cone indium distribution. Thus the structural changes of the quantum dots during overgrowth are characterized by a decrease of the indium stoichiometry and a formation of a reversed-cone indium distribution.

Layer 3.6

The deposition of 3.6 ML InAs is a rather high amount for the InAs/GaAs quantum dot system. Earlier investigations have shown coalescence of quantum dots already when depositing 3.0 ML InAs at MBE growth rates > 0.1 ML s^{-1} and temperatures of $\sim 500°C$ [138]. But for lower growth rates of about 0.015 ML s^{-1} only 3% of all quantum dots were found to be irregular large islands [138]. This explains why the sample investigated here, containing 3.6 ML InAs and grown with 0.017 ML s^{-1} (see section 5.1), shows large quantum dots but no irregular large islands.

The XSTM image in Fig. 5.19 (a) presents a large quantum dot with a baselength of about 22−25 nm and a height of 4 nm. Although the image could be equalized according to the surface unit cell (section 4.5.2), the baselength can only be approximated, because the quantum dot image is bent at its lower border due to drift effects of the scanning tip. Therefore the shape, indicated by the dotted contour line in (b), is not given for the lower quantum dot side. However, the measured inclination angle of about 29° could belong to the {124} or to the {135} facet, as explained when discussing layer 2.2. The truncation of the quantum dot is very pronounced, because the length of the quantum dot top facet amounts to about 13 nm. Moreover the strain in the system is very high, which can be concluded from the extreme undershoots in the local stoichiometry profile in Fig. 5.19 (c) on both sides of the quantum dot.

From a visual inspection of the XSTM images the indium distribution seems to be rather homogeneous, but the result of the local stoichiometry determination shows that the highest amount of indium is located near the quantum dot base. In Fig. 5.19 (c) the cyan curve represents the analyzed height profile, and the red curve is the three-point averaged stoichiometry. From both curves it can be seen that the indium amount has its highest value close to the quantum dot base and varies between 90 and 100%. This behavior is therewith different from the other observed layers, where most indium is located at the quantum dot center or even at its top. This contrary behavior can be seen in particular from a comparison with Fig. 5.15 (c), where the stoichiometry profile at the quantum dot region has the opposite shape, starting with a low amount of indium

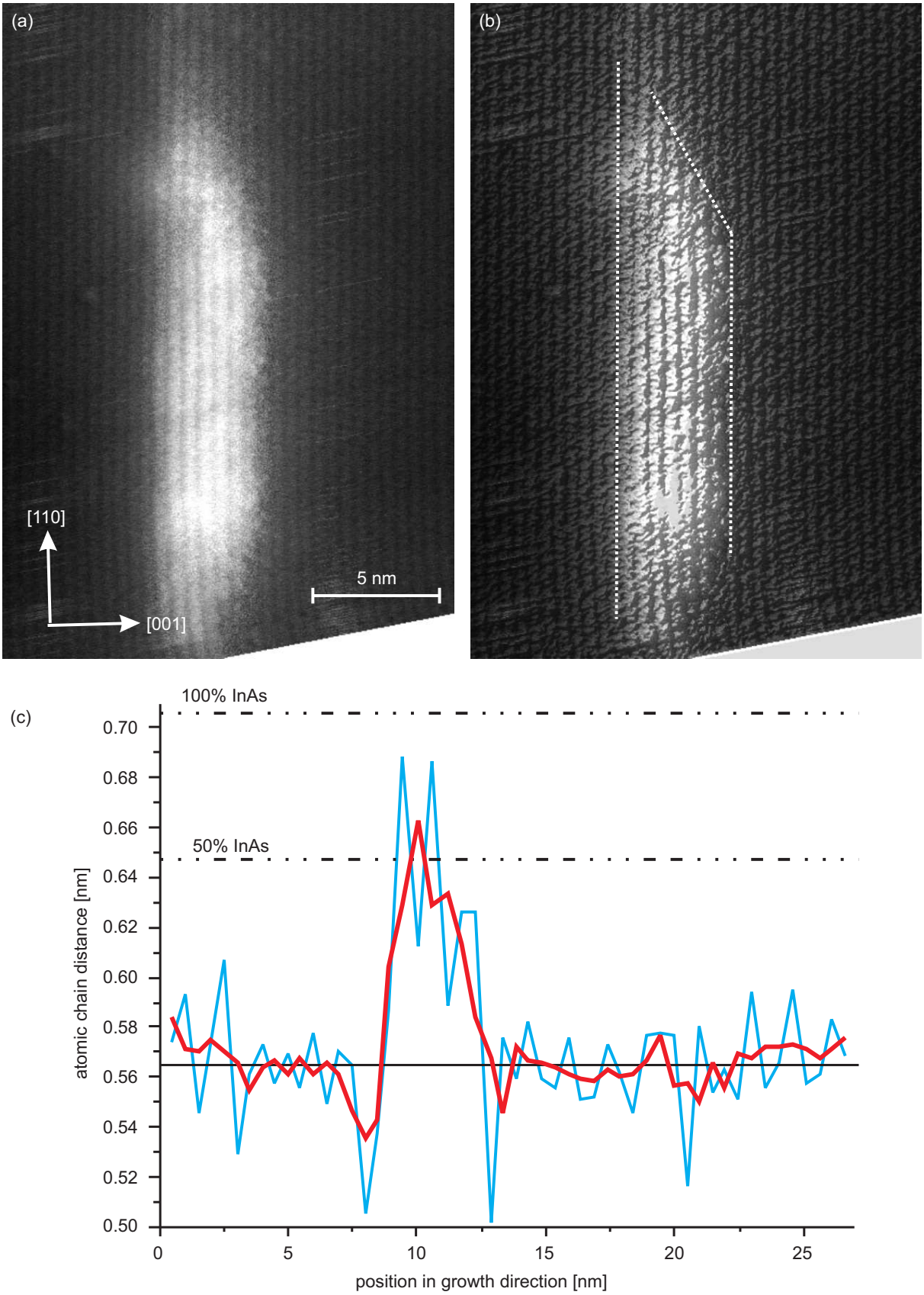

FIGURE 5.19: (a) Equalized XSTM image and (b) relief map image of a quantum dot at layer 3.6, taken at $I_T = 80$ pA and $V_S = -2.3$ V. The possible quantum dot shape is indicated by the dotted contour line. (c) Local stoichiometry determination of this quantum dot. The cyan curve represents the result of the analyzed height profile, reaching a maximum indium amount of 100%. The red curve is the three-point averaged stoichiometry, representing the indium distribution.

and increasing in growth direction.

The discussed profile in Fig. 5.19 (c) is not a general behavior at layer 3.6. Figure 5.20 (a) shows a high pass image of a quantum dot located between two surface steps. With a baselength of about 20 nm this quantum dot is a smaller one at this layer. It can be seen from the XSTM image that a high amount of indium is located at the top of the quantum dot. The same result arises by the local stoichiometry determination, shown in Fig. 5.20 (b). The indium amount increases at the quantum dot baseline and reaches up to 100% at its top. So this smaller quantum dot shows the same behavior as the quantum dots found at the layers with less material amount. Such profiles were already found earlier for MBE grown quantum dots [116, 117].

In Fig. 5.20 (c) and (d) two larger quantum dots are imaged, but with less resolution. Both quantum dots have a baselength of about 26 nm, and show an almost homogeneous indium distribution similar to the XSTM image in Figure 5.19 (a) . Unfortunately the resolution is too low for analyzing the local stoichiometry profiles.

In conclusion, quantum dots with smaller sizes that were observed also at the layers with less InAs material show typical reversed cone behavior, whereas for larger quantum

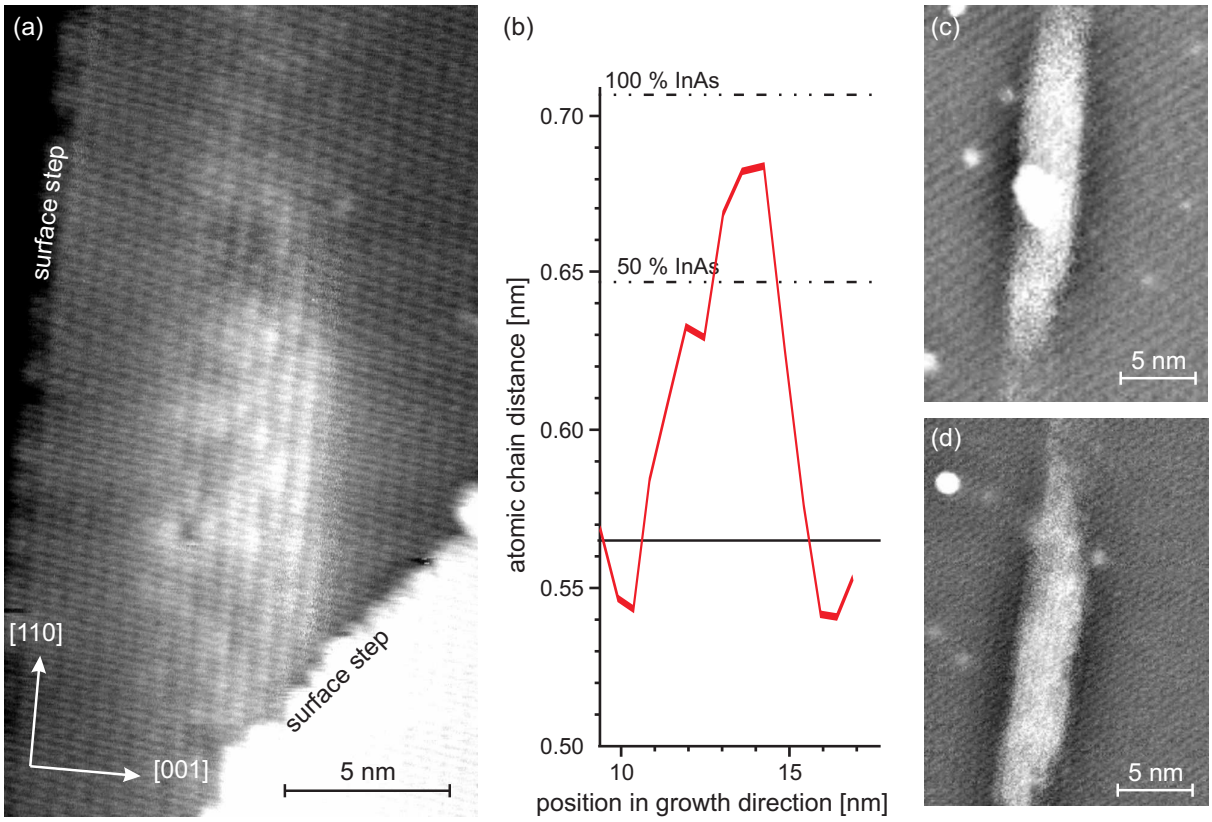

FIGURE 5.20: (a) High-pass filtered XSTM image of a smaller quantum dot found in layer 3.6, taken at $V_S = -2.3$ V. Indium atoms are mostly concentrated at the top of the quantum dot. (b) Extraction from the local stoichiometry determination of the quantum dot shown in (a). The red curve represents the averaged stoichiometry, reaching up to 100% indium. (c) and (d) XSTM images of large quantum dots at layer 3.6, showing almost homogeneous indium distributions, taken at $V_S = -2.2$ V and $V_S = -2.0$ V. All three XSTM images were taken at $I_T = 80$ pA.

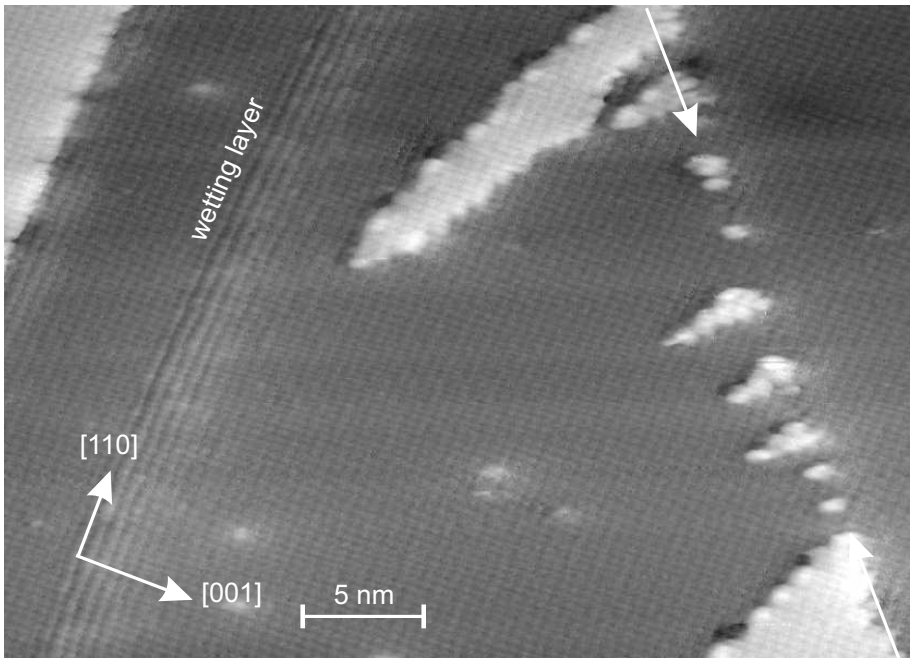

FIGURE 5.21: Equalized XSTM image of the wetting layer 3.6, taken at $I_T = 80$ pA and $V_S = -2.1$ V. The white arrows indicate the probable position of a dislocation line.

dots with baselengths > 22 nm the highest indium amount is located near the quantum dot baseline.

A final remark to layer 3.6 is directed at the high material amount and the possibility of irregular large islands. Such islands are found in earlier investigations with a size increase by a factor 2−3 compared to usual quantum dots [138]. They represent probably incoherent quantum dots, relaxing strain through an incorporation of dislocations [139]. Hence an indication of the existence of such irregular large island can be the existence of dislocations. A possible dislocation is visible by the step defects indicated in Fig. 5.21 by the two arrows. Since the scan area in [110] direction of the tip ends in this image, no direct information about an irregular island at the intersecting point between the wetting layer and this step defect line exists. Nevertheless, using this observation and assuming one irregular island with an diameter of about 40 nm within a scanned wetting layer length of 1.5 μm a density of the incoherent quantum dots of less than 1.4×10^9 cm^{-2} can be estimated.

Stoichiometry of the wetting layers

After the detailed analysis of the quantum dot shape and stoichiometry with increasing amount of material, Fig. 5.22 (a) shows the results of the local stoichiometry determination of the wetting layers grown with nominal 1.8 ML, 2.2 ML, 2.6 ML and 3.6 ML InAs. It can be seen that the maximum indium content for 1.8 ML and 3.6 ML amounts to about 25−30%, while for 2.2 ML and 2.6 ML it is slightly lower with about 20%. Additionally, a trend towards increasing layer thickness with increasing indium deposition is observed, since the full width at half maximum determined under consideration of the undershoots amounts to about 0.90 nm, 1.35 nm, 1.28 nm, and 1.65 nm, respectively. The shape of all curves starts with a steep flank and decreases slowly along growth direction, especially

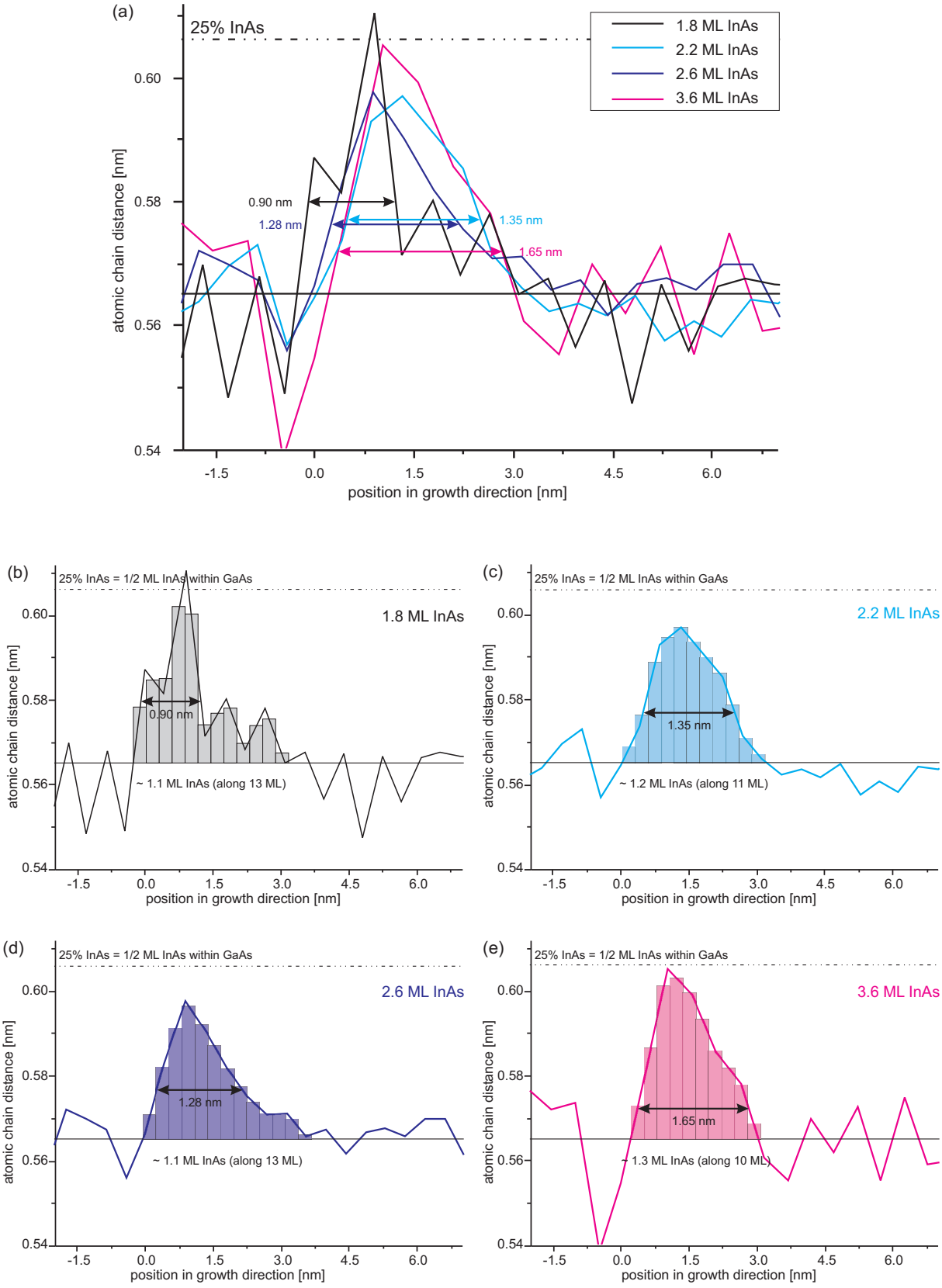

FIGURE 5.22: (a) Local stoichiometry determination from the wetting layers grown with nominal 1.8 ML (black), 2.2 ML (cyan), 2.6 ML (blue) and 3.6 ML (magenta) InAs. (b–e) Same stoichiometry results, plotted individually for each layer together with a bar chart, indicating a total InAs amount of 1.1–1.3 ML segregated along 10–13 monolayers.

for layers 1.8 and 2.6, indicating strong segregation effects. This is in contrast to the ideal Stranski-Krastanow growth and also to a later discussed InAs wetting layer grown under Sb supply (chapter 6), where reduced segregation is observed.

The strong segregation here is further confirmed by considering the bar chart of each wetting layer (b−e). Each bar has a thickness of one monolayer GaAs, and in order to obtain the integrated indium content of each layer, 10−13 ML have to be taken into account, indicating again a strong segregation. Furthermore, a total InAs content of the wetting layer between 1.1 and 1.3 ML is derived from Fig 5.22, independent of the nominal InAs thickness. This resulting amount of about 1.2 ML InAs in the wetting layer is in good agreement with an earlier determination on MBE grown InAs quantum dots [122], and slightly lower than reported from an investigation on MOCVD grown quantum dots [111]. In the latter case quantum dots with a nominal material amount of 1.8 ML InAs were analyzed, and an amount of 1.4−1.5 ML InAs in the wetting layer was derived. However, it should be noted that the actual InAs content may be slightly larger than the determined amounts shown in Fig. 5.22, since strain effects as indicated especially by the undershoot at layer 3.6 are not taken into account.

5.3.3 Reduced growth temperature

In addition to the investigation on quantum dots containing an increasing amount of InAs, in this section the resulting structures after capping of quantum dots grown under a modified growth temperature will be presented. Thus the influence of the growth temperature during the capping process can be analyzed. Sample III contains 1.8 ML InAs as well as sample I (c) but was grown at only 420°C, as shown in Fig. 5.1. Unfortunately the specific investigated {110} cleavage surface orientation is not known in this case, so that in all following images only the growth direction will be indicated.

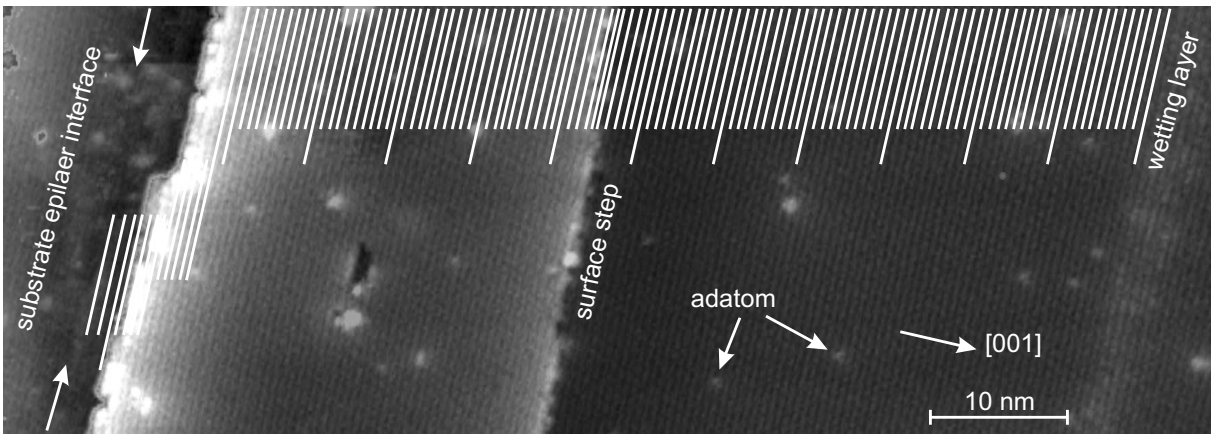

FIGURE 5.23: Filtered XSTM overview image of sample III, including the interface between substrate and epilayer and the InAs wetting layer, taken at $V_S = -2.0$ V and $I_T = 80$ pA. The position of the substrate interface is indicated by two white arrows, and the white lines indicate the atomic chains in order to determine the thickness of the spacing layer, which amounts to 69 nm.

The interface between substrate and epilayer can be seen in the left side of the XSTM overview image shown in Fig. 5.23. The interface is indicated by the two white arrows and can be recognized by a small trench and a higher amount of adatoms due to the increased sticking coefficient in this defective region. This behavior is observed on a large range along the atomic chains. The InAs wetting layer is also imaged at the right side of Fig. 5.23.

Each white line between the interface and the InAs wetting layer indicates one atomic chain, allowing to determine the thickness of the spacer layer to 122 atomic chains, which is equivalent to 69 nm. The nominal thickness amounts to 72 nm, which indicates a high accuracy in the growth parameters. In contrast, the observed spacer layer thicknesses of sample I (c) were found to amount to only 65% of the nominal value, as shown in Fig. 5.13. This effect may be related to the GaAs growth temperature, amounting to only 520°C in sample I (c), whereas here at sample III the buffer layer underneath the InAs wetting layer is grown at 560°C. Because both samples are grown in the same MBE chamber and with the same nominal growth rate this behavior indicates that the growth accuracy is directly connected to the GaAs growth temperature, e.g. due to the temperature dependent dissociation of As_4 into As_2 precursors.

A small quantum-dot like structure is shown in Fig. 5.24 (a) in an equalized XSTM image. The possible truncated shape is indicated by the dotted contour line in the high-pass filtered image [Fig. 5.26 (b)]. Above the quantum dot additional single indium atoms are visible, marked by white circles, indicating strong segregation effects. From this image a quantum dot baselength of about 8 nm and a height of 2.2 nm can be derived, which is considerably smaller than the sizes of quantum dots grown at 450°C. The steep measured angles of about 53° probably belong to {111} side facets, which

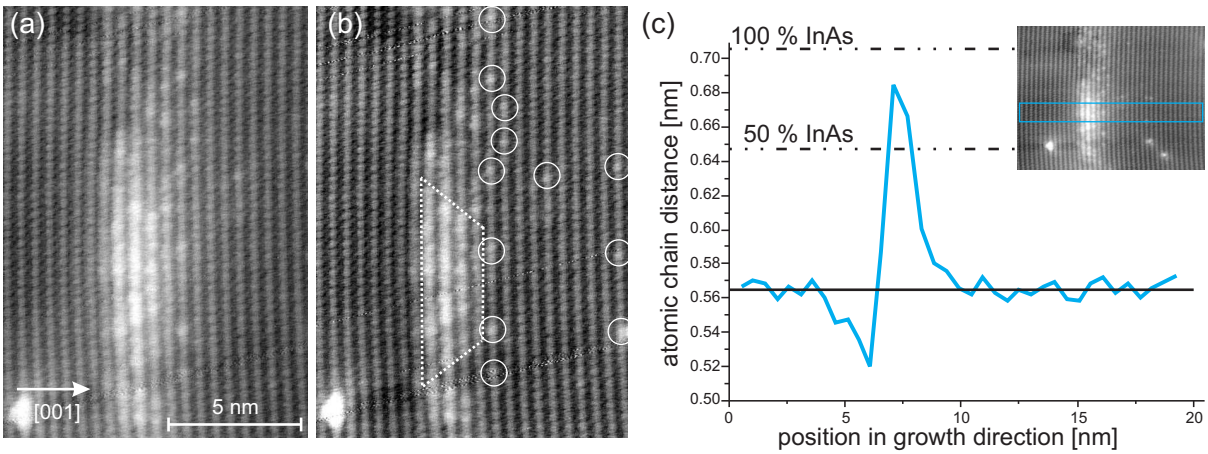

FIGURE 5.24: (a) Equalized XSTM image and (b) high-pass filtered image of a small quantum-dot like structure grown at 420°C, taken at $V_S = -1.6$ V and $I_T = 80$ pA. The possible shape is indicated by the dotted contour line, and single indium atoms are marked by white circles. (c) Local stoichiometry determination along the box shown in the XSTM image of the inset. The cyan curve represents the InAs stoichiometry, which reaches up to 90%.

nominally amounts for both cleavage surfaces to 54.7° (see Fig. 4.6). The result of the local stoichiometry determination is given in Fig. 5.24 (c). The analyzed height profile is shown in the XSTM inset image by the cyan box, and the resulting stoichiometry amounts to about 90%. A compression in the GaAs can be seen only underneath the quantum-dot like structure by the imaged undershoot. This behavior is similar to that of the quantum dots grown with 1.8 ML InAs at 450°C (shown in Fig. 5.10). Furthermore, the indium distribution is highest slightly above the quantum dot baseline in both cases.

Additional typical structures are shown in Fig. 5.25, including another small quantum-dot like structure with about 10 nm baselength and 2.8 nm height (a). The up to 4 nm thick wetting layer is characterized by a fluctuating thickness (b), and within a long area of the wetting layer also regions without any indium material can be observed, indicated in (c) by the dotted oval. The lateral extension of this unusual gap amounts to about 10 nm. Such gaps in the wetting layer are not common for InAs/GaAs, but known from the GaSb/GaAs system, where they are observed even for different Sb contents [98, 140, 141].

Above the gap in the wetting layer a small region with higher indium-related contrast can be seen, which is also imaged in the lower inset of Fig. 5.25 (d). The local stoichiometry determination of this wetting layer region is given by the dotted green line, and is

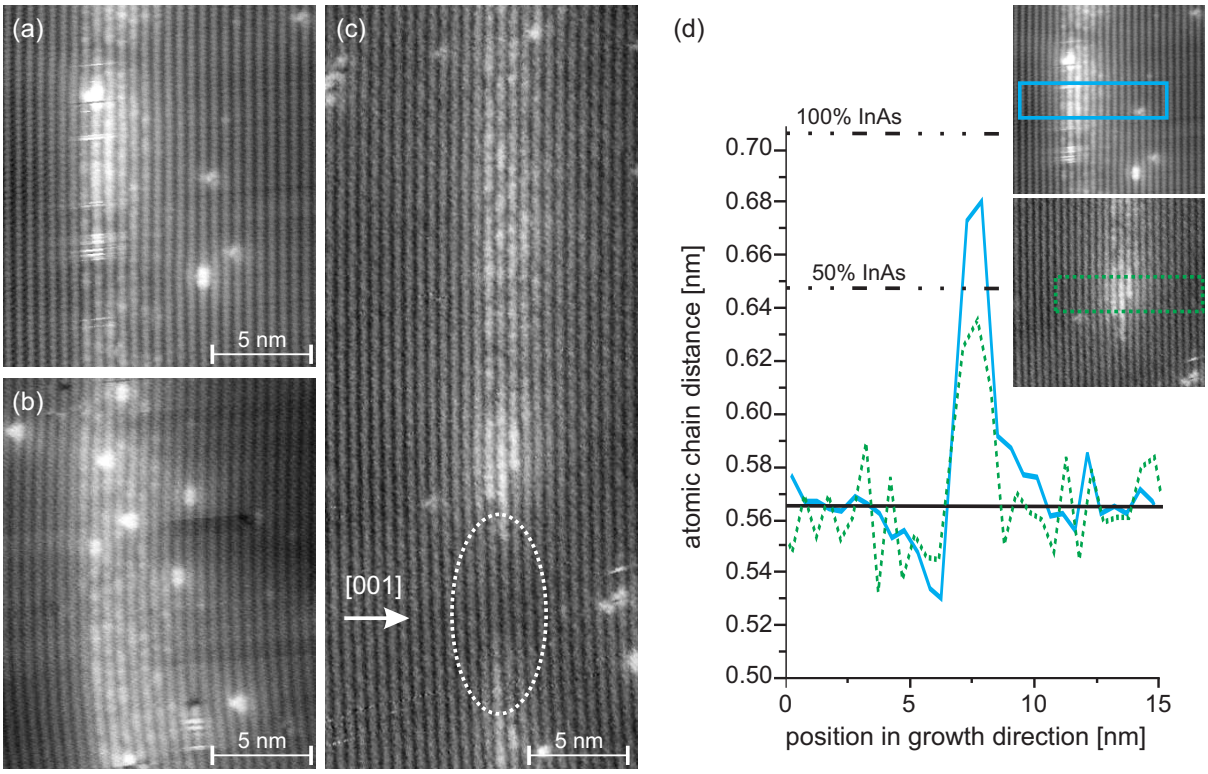

FIGURE 5.25: Filtered XSTM images of (a) a small quantum-dot like structure taken at $V_S = -1.9$ V, (b) a wetting layer thickness fluctuation taken at $V_S = -1.8$ V, and (c) a wetting layer stripe with a 10 nm wide gap indicated by the dotted oval and a region of higher indium contrast above it, taken at $V_S = -2.5$ V. All XSTM images are taken at $I_T = 80$ pA. (d) Local stoichiometry determination of the quantum-dot like structure (cyan) and the pronounced wetting layer region (green). The region of both height profiles are shown in the XSTM images of the insets.

compared with the result of the quantum-dot like structure shown in (a), given by the solid cyan line. The maximum indium content amounts to about 80% in the dot-like structure and to 40% in the pronounced wetting layer region, which is higher than the typical wetting layer value of 15−25%. Again the characteristic undershoot is found at the baseline of the quantum-dot like structure, but also for the wetting layer a small undershoot can be seen.

In conclusion the observed quantum-dot like structures grown at 420°C with typical baselengths of 5−8 nm and heights of 2−3 nm are considerably smaller than the actual quantum dots grown at higher temperature. Moreover the density of these structures of about 2×10^{11} cm^{-2} is significantly higher than for the quantum dots grown at 450°C, which amounts to only 6×10^{10} cm^{-2}. The maximum indium content in the quantum-dot like structures grown at 420°C varies between 50 and 90%, and typical profiles show an undershoot only at the baseline, but not at its top, so it can be concluded that these structures are less strained. The indium amount in the wetting layer varies between 15 and 25%, but also gaps in the layer are observed as well as pronounced regions with an higher amount of indium reaching up to 40%, the latter representing a transition between the wetting layer fluctuations and the quantum-dot like structures. Additionally single indium atoms are found above the quantum dots and the wetting layer, indicating strong segregation effects.

Finally a surprisingly large quantum dot of this sample is shown in Fig. 5.26 (a). From the image a baselength of the quantum dot of about 17 nm and a height of 2.8 nm can

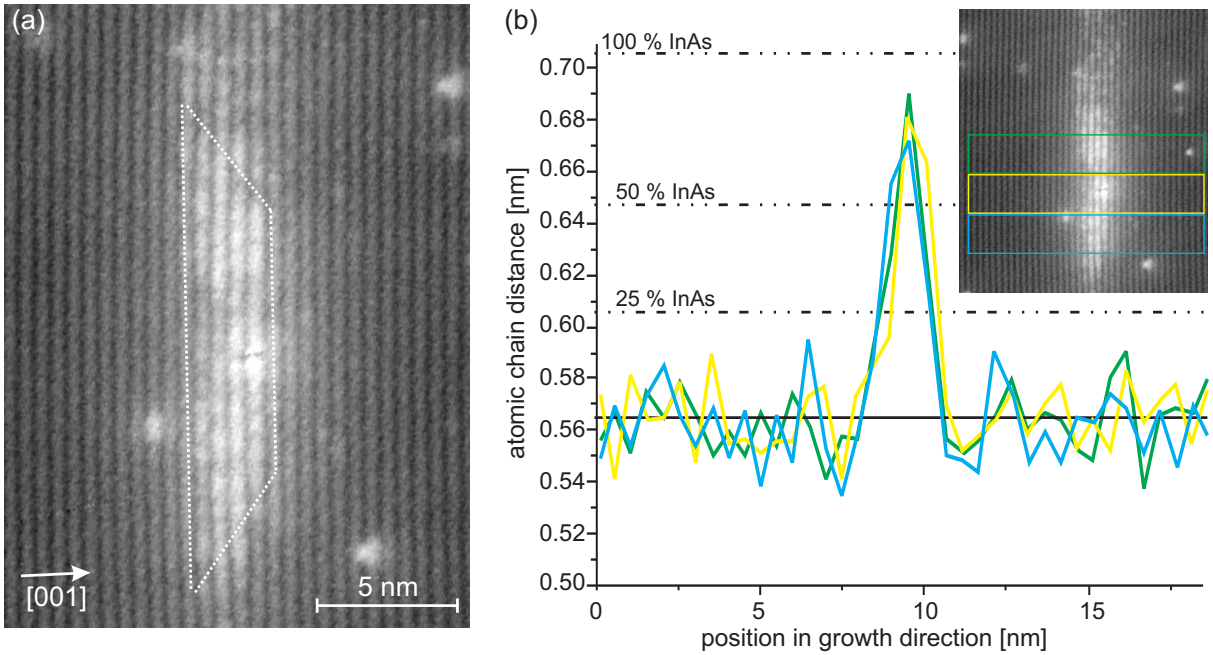

FIGURE 5.26: (a) Filtered XSTM image of an unusually large quantum dot grown at 420°C, taken at $V_S = -2.5$ V and $I_T = 80$ pA. The truncated quantum dot shape is indicated by the dotted contour line. (b) Local stoichiometry determination of this quantum dot for different positions. The maximum indium content amounts to about 90%.

be derived, and the truncated quantum dot shape is indicated by the dotted contour line. The measured inclination angles amount to between 36° and 39° and are therewith in a similar range of those found for quantum dots grown at 450°C, shown e.g. in Fig. 5.8. These angles could belong to {101} or {112} side facets and are as well steeper than the {137} side facets previously observed with top-view STM [114].

The local stoichiometry determination of this large quantum dot is presented for three different positions, indicated by the colored lines, as shown in the XSTM inset [Fig. 5.26 (b)]. Also the wetting layer beside the quantum dot is investigated (not shown here), and yielding an indium amount of about 25%. The maximum indium amount in the quantum dot is very similar for all three positions and varies between 80−90%. Again an undershoot can bee seen at the quantum dot base and at its top as it is also observed in Fig. 5.11 for a quantum dot grown at 450°C. Thus this quantum dot is generally similar to those grown at slightly higher temperatures, but untypical for sample III.

5.4 TEM and PL results

Before discussing the XSTM data the results from transmission electron microscopy (TEM) and photoluminescence (PL) measurements will be presented here. TEM data were obtained by H. Kirmse and I. Häusler from the HU Berlin, and PL spectra were taken by F. Guffarth and R. Heitz†[1] at the TU Berlin [142, 143].

With TEM further structural data are provided as well as information on stoichiometry and material content of the InAs quantum dots and the wetting layers. PL measurements will describe the optical properties of the quantum dots, complementing the XSTM and TEM data.

5.4.1 TEM results

TEM investigations were performed on sample I (c), containing 1.8 ML, 2.2 ML, 2.6 ML, 3.0 ML, and 3.6 ML InAs deposited at 450°C. Cross-sectional TEM data using the (002) reflection display a composition sensitive image, allowing the determination of the quantum dot shape, size and stoichiometry, while the (004) reflection yields a strain sensitive image to locate the quantum dot positions.

In typical InGaAs dark-field TEM images the wetting layers and quantum dots are imaged as dark stripes and objects, respectively, in contrast to the bright surrounding GaAs matrix, as shown in Figure 5.27. In the strain sensitive (004) reflection images the quantum dots are displayed as dark pronounced objects [Figure 5.27(a)], whereas in the composition sensitive (002) reflection images only a weak quantum dot contrast is observed [Figure 5.27(b)]. The InAs wetting layer is in both cases visible as a dark horizontal line. The increasing contrast of the quantum dots due to increasing material amount can be observed in Figure 5.27 (c). The quantum dot size observed with TEM for 1.8 ML and 2.2 ML InAs amounts laterally to about 10−20 nm, while the height amounts

[1] In memoriam to our deceased colleague

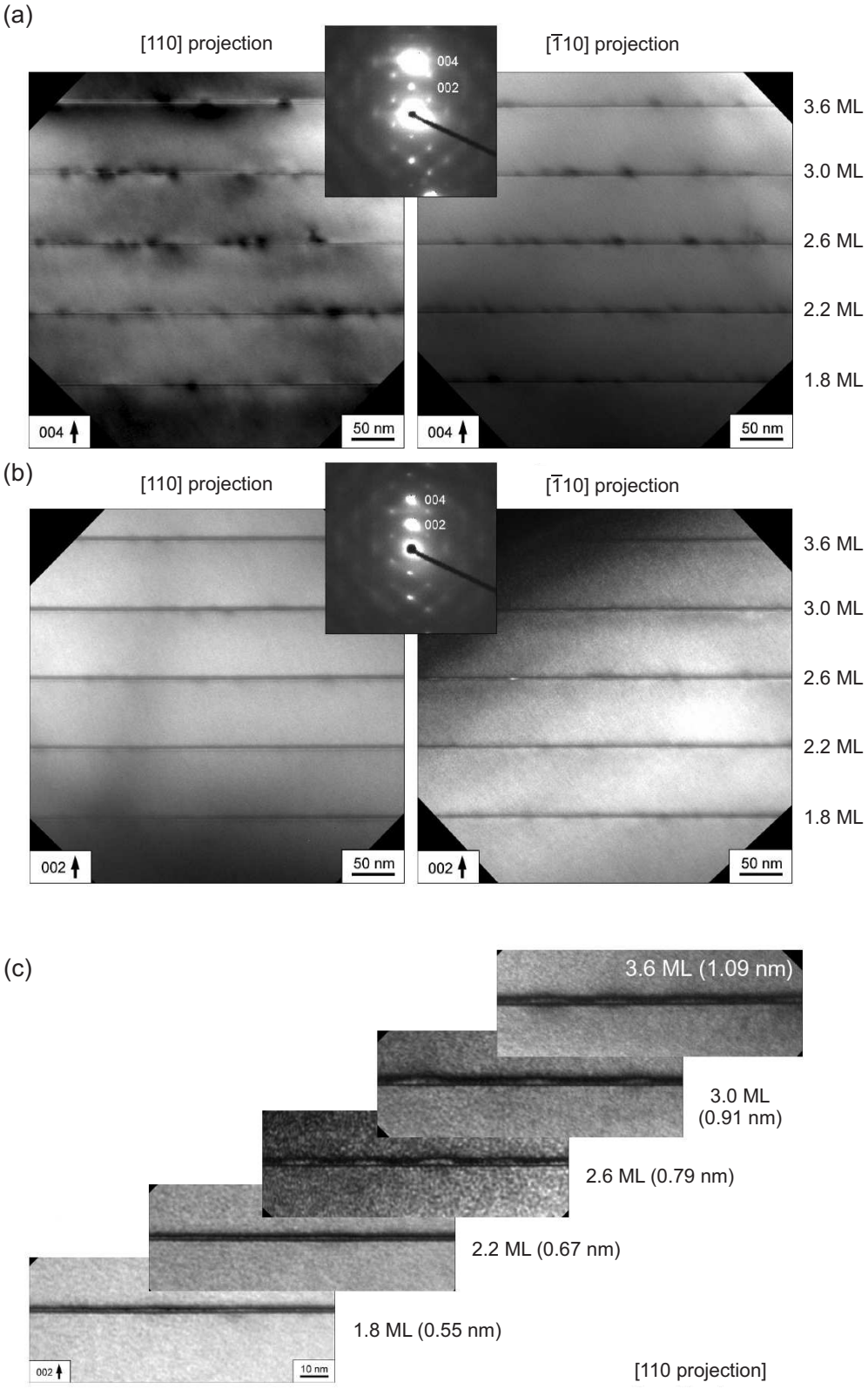

FIGURE 5.27: Cross-sectional TEM dark-field images of the InAs quantum dots grown at 450°C for [110] and [$\bar{1}$10] beam direction: (a) Strain sensitive images using the (004) reflection to locate the quantum dot positions, (b) composition sensitive images using the (002) reflection for stoichiometry analysis. The insets in (a, b) show the selected area diffraction patterns taken prior to the projection images. (c) Composition sensitive images using the (002) reflection with increasing nominal amount of InAs.

here to about 2−3 nm. Lateral sizes and heights increase with increasing amount of InAs to 14−19 nm and 2.6 nm (2.6 ML InAs), 15−22 nm and 2.8 nm (3.0 ML), and 18−24 nm and 2.9 nm (3.6 ML). The determination of the size is difficult especially for low material amount, because the quantum dots are located within the wetting layer, so that the quantum dot height does not vary much from the wetting layer height. This behavior fits well to the XSTM data, showing wetting layer thicknesses between 3 and 4 nm with strong segregation in growth direction.

The indium content is derived from TEM data by an analysis of the total material projected in beam direction, and from the resulting profiles along the growth direction the value of the maximum indium content is considered. However, the investigated region may include GaAs matrix material, InGaAs wetting layer material, and in the optimum case one complete quantum dot. The presence of the GaAs matrix material leads to a reduction of the derived average indium amount, which is thus lower than the indium content of the quantum dots. The latter can only be estimated, since the ratio of GaAs volume to quantum dot volume is unknown. This reducing indium content effect − or the so-called matrix effect − leads to the value of the maximum indium content, averaged on the investigated region. For smaller quantum dots with heights similar to the wetting layer this matrix effect is even stronger than for pronounced quantum dots with larger volumes [143].

The indium content of the wetting layers determined with TEM, which is not affected by the matrix effect, amounts to at least 23% for 3.6 ML and to 27% for all other layers, and the thickness of the layers increases with increasing material amount from 1.8−3.0 nm. These data are also in good agreement with the XSTM results (section 5.3.2 or table 5.1 at page 69), although the measured thicknesses are generally slightly smaller in TEM.

In contrast, the TEM and XSTM investigations differ considerably regarding the derived quantum dot stoichiometry. With TEM no distinctive differences are found between the wetting layers and the quantum dots grown with low nominal InAs thickness (1.8 ML and 2.2 ML) due to the above described matrix effect. Also in the layers containing nominal 2.6 ML−3.6 ML InAs the indium content observed by TEM, amounting to 28%−35%, is clearly below the XSTM results, ranging usually between 75%−100%. Furthermore an almost homogeneous indium distribution in the quantum dots is observed with TEM [143], while from detailed XSTM investigations also reversed-cone profiles − especially for larger quantum dots − are derived, demonstrating the advantages of the stoichiometry determination from XSTM data.

In TEM investigations no incoherent quantum dots are found, even not for the layer with 3.6 ML InAs. This confirms the XSTM results and indicates an excellent growth also for a high material amount.

In conclusion the TEM results confirm the increase of the quantum dot sizes with increasing material amount, and furthermore the increase of the wetting layer thicknesses, indicating strong segregation effects. An analysis of the quantum dot shape cannot be easily derived by TEM due to the limit of resolution. TEM and XSTM techniques differ

considerably regarding the indium content in the quantum dots, due to the TEM associated matrix effect, so that detailed information about the indium distribution can only be achieved with atomically-resolved XSTM data.

5.4.2 PL results

At first PL measurements will be presented from sample II (see Fig. 5.1) containing 3.6 ML InAs deposited at 450°C. Figure 5.28 (a) shows three PL spectra excited at 750 nm and recorded at 7 K (cyan), 100 K (green), and 150 K (red), respectively. In all these three spectra five PL peaks can be observed, and assigned from high to low luminescence energy to the GaAs matrix, the InAs wetting layer, an InAs wetting layer inhomogeneity, the InAs quantum dots, and to dopants of the substrate or impurities. The temperature dependent InAs quantum dot PL peak around 1.1 eV corresponds to a wavelength of about 1.1 μm, representing a large quantum dot volume in agreement with the deposited material amount of 3.6 ML. Typically this PL peak should dominate the luminescence spectra, while here each spectrum is characterized by an unusually broad luminescence band ranging from 0.9 eV to 1.4 eV. This effect could be related to a general material problem, so that the entire luminescence signal is not only connected to the InAs layer.

The contour plot of Fig. 5.28 (b) displays PLE data, showing the luminescence intensity as a function of the emission and excitation energies. The horizontal features at 1.51 eV and 1.43 eV are assigned to a direct excitation of the GaAs barrier and the InAs wetting layer. The latter is usual for MBE grown InAs/GaAs samples. It follows that the broad PL peak at 1.3 eV in Fig. 5.28 (a) is connected to a wetting layer inhomogeneity, which could be due to thickness or composition variations, leading to a high density of flat localization centers. Furthermore the broad PL peak at 1.05 eV is assigned to dopants of the substrate or impurities, which may be located in the substrate, at the surface, or at the inferface to the epilayer. The interface between the substrate and the epilayer is found to be a defective region, since small trenches are observed in the XSTM images, as shown in Fig. 5.23. Normally samples grown on semiisolating substrates are used for PL experiments, but in the present case the samples are also investigated by XSTM, which requires a certain conductivity of the substrate to enable tunneling.

The PL and PLE results of sample III, containing 1.8 ML InAs deposited at a lower temperature of 420°C and also grown on doped substrate, are presented in Figure 5.29. In contrast to sample II the luminescence around 1.3 eV is the most pronounced peak in this spectra, while it is slightly shifted to lower energies. The broad peak around 1.05 eV is once more connected to the doped substrate or impurities, but the most important point is the absence of a distinctive quantum dot peak. This observation leads to the conclusion that only small quantum-dot like structures and fluctuations of the wetting layer composition and thickness are contained in this sample, as observed in the XSTM images. The PL signal related to the quantum-dot like structures and the fluctuations will all contribute to the peak around 1.3 eV, explaining its broadness. Thus, the lower growth temperature seems to prevent the formation of sufficiently large quantum dots or

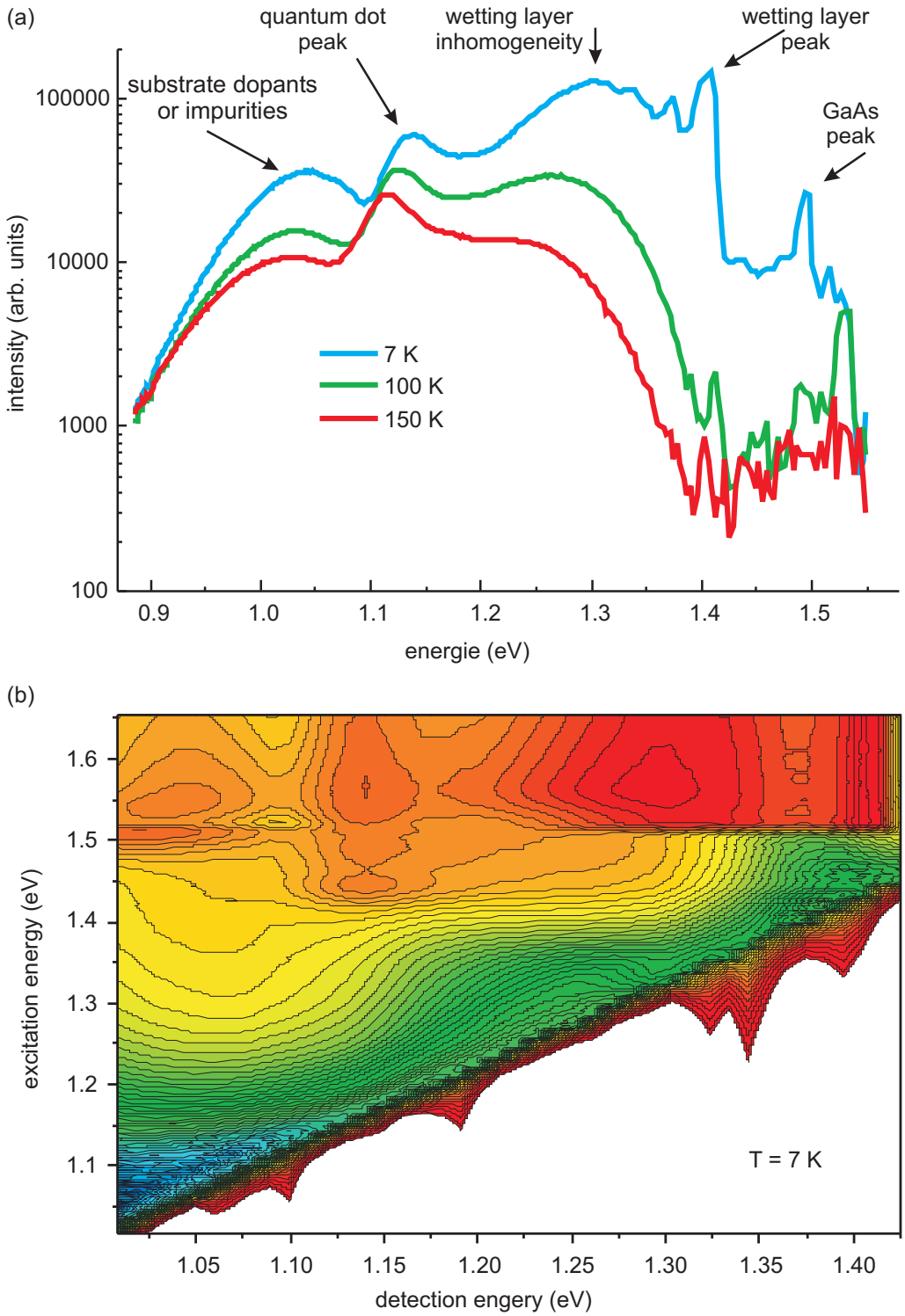

FIGURE 5.28: PL data of sample II containing 3.6 ML InAs deposited at 450°C and grown on doped substrate. (a) PL spectra taken with 750 nm excitation at 7 K (cyan), 100 K (green), and 150 K (red). (b) PLE contour data at 7 K.

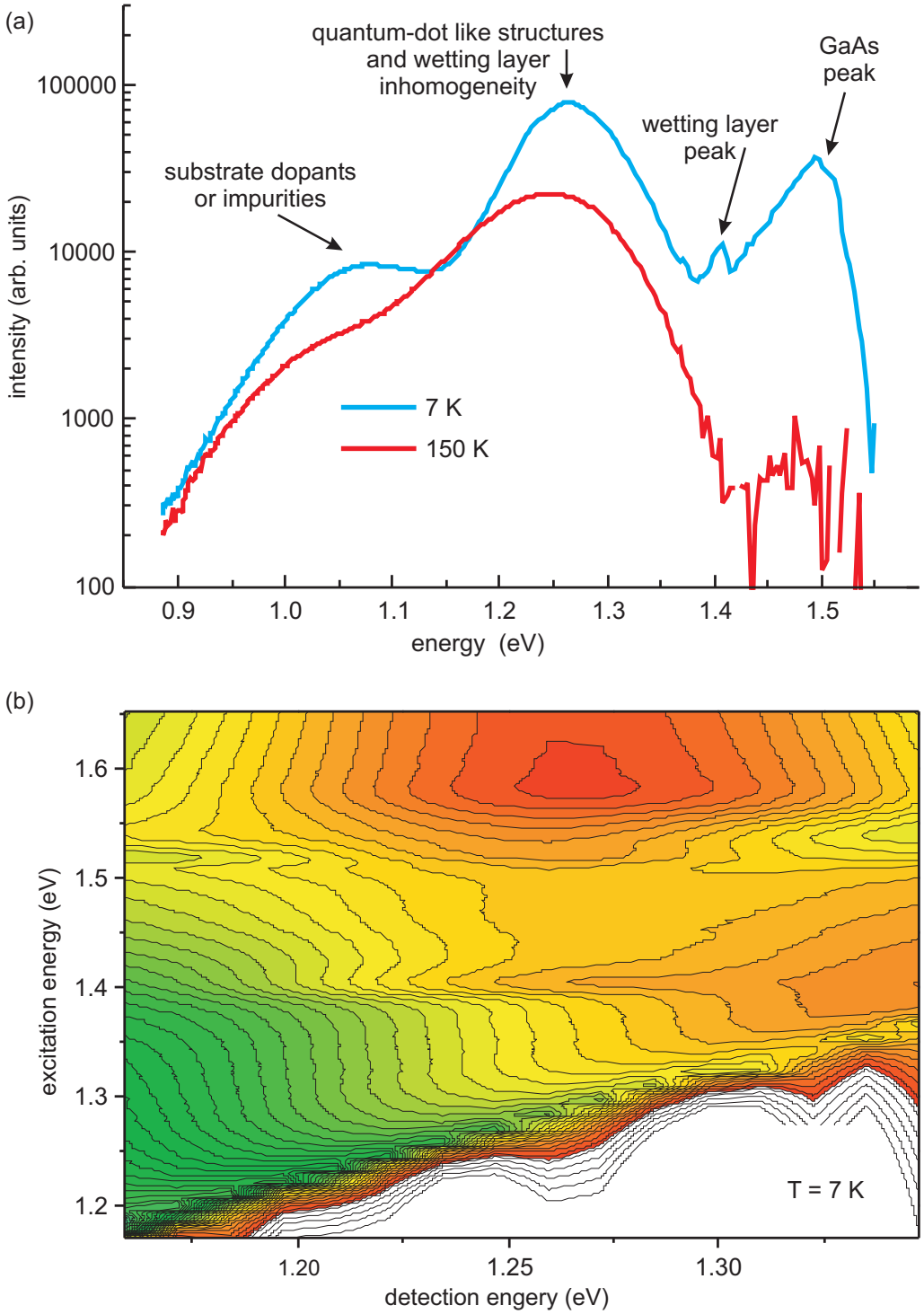

FIGURE 5.29: PL data of sample III containing 1.8 ML InAs deposited at 420°C and grown on doped substrate. (a) Spectra taken with 750 nm excitation at 7 K (cyan) and 150 K (red). (b) PLE contour plot at 7 K.

introduces defects favoring non-radiative recombination.

In conclusion the broad band around 1.3 eV is assigned to composition and thickness variations of the wetting layer, which leads to a high density of flat localization centers, and to the quantum-dot like structures. The absence of a distinctive quantum dot luminescence peak at sample III confirms the XSTM observations of a high number of small dot-like structures and distinctive fluctuations of composition and thickness in the InAs wetting layer. In contrast the peak around 1.1 eV observed at sample II belongs to sufficiently large InAs quantum dots, as they are as well observed in the XSTM images. For further investigations of excited quantum dot states it is necessary to use semiisolating substrate.

Hence sample I (b) containing 1.8 ML InAs deposited at 450°C was specifically grown for PL measurements on undoped GaAs. It should be noted that a homogeneous PL signal is measured along several sample positions, indicating identical quantum dots in the whole sample. The broad quantum dot peak is located around 1.3 eV, while the wetting layer peak is visible at 1.44 eV and the GaAs barrier above 1.48 eV, as shown in Figure 5.30 (a). The three PL spectra differ regarding the excitation energy: The cyan spectra is taken at a excitation density of about 9 kW cm^{-2}, while the spectra indicated in green and red are taken at lower excitations by factors of 100 and 1000, respectively.

The PL spectra can be interpreted as follows: The peak labeled D at 1.29 eV has the highest intensity in all three curves and is thus the ground state of the dominating quantum dot subensemble. The shape of the high excitation curve (cyan) is different from the two other ones (green and red) [Fig. 5.30 (b)], indicating the existence of exited states. Therefore the peak A at 1.41 eV is assigned to an excited quantum dot state and it is completely vanishing with decreasing excitation density, while the peaks labeled B and C are only decreasing. The explanation for the existence of the peaks B and C will be given further below.

Because the spectra taken at 90 W cm^{-2} (green) and 9 W cm^{-2} (red) have rather similar shapes despite of the decrease in excitation density, they cannot contain exited quantum dot states. Thus the peaks labeled with B−F are probably connected to the so-called shell-like growth mode: In an earlier investigation a multimodal decomposition of PL spectra was connected to the growth of quantum dots in steps of monolayer thickness [144]. In this way, individual PL peaks were associated to a respective InAs quantum dot subensemble. These subensembles gradually differ in height by single InAs monolayer steps [91, 144]. Furthermore the relative intensity increase at peaks B and C observed at the high excitation curve (cyan) can now be explained by a superposition with exited multimodal states.

Pure InAs quantum dots with truncated pyramidal shapes, similar baselengths as observed here, and a height of 3 ML would result in a ground-state luminescence of 1.29 eV, while for larger quantum dot heights of e.g. 10 ML luminescence around 1.1 eV is expected [144]. However, from the XSTM results a variation in the quantum dot height between 4 and 6 atomic chains or 8−12 ML was observed. Furthermore a strong inter-

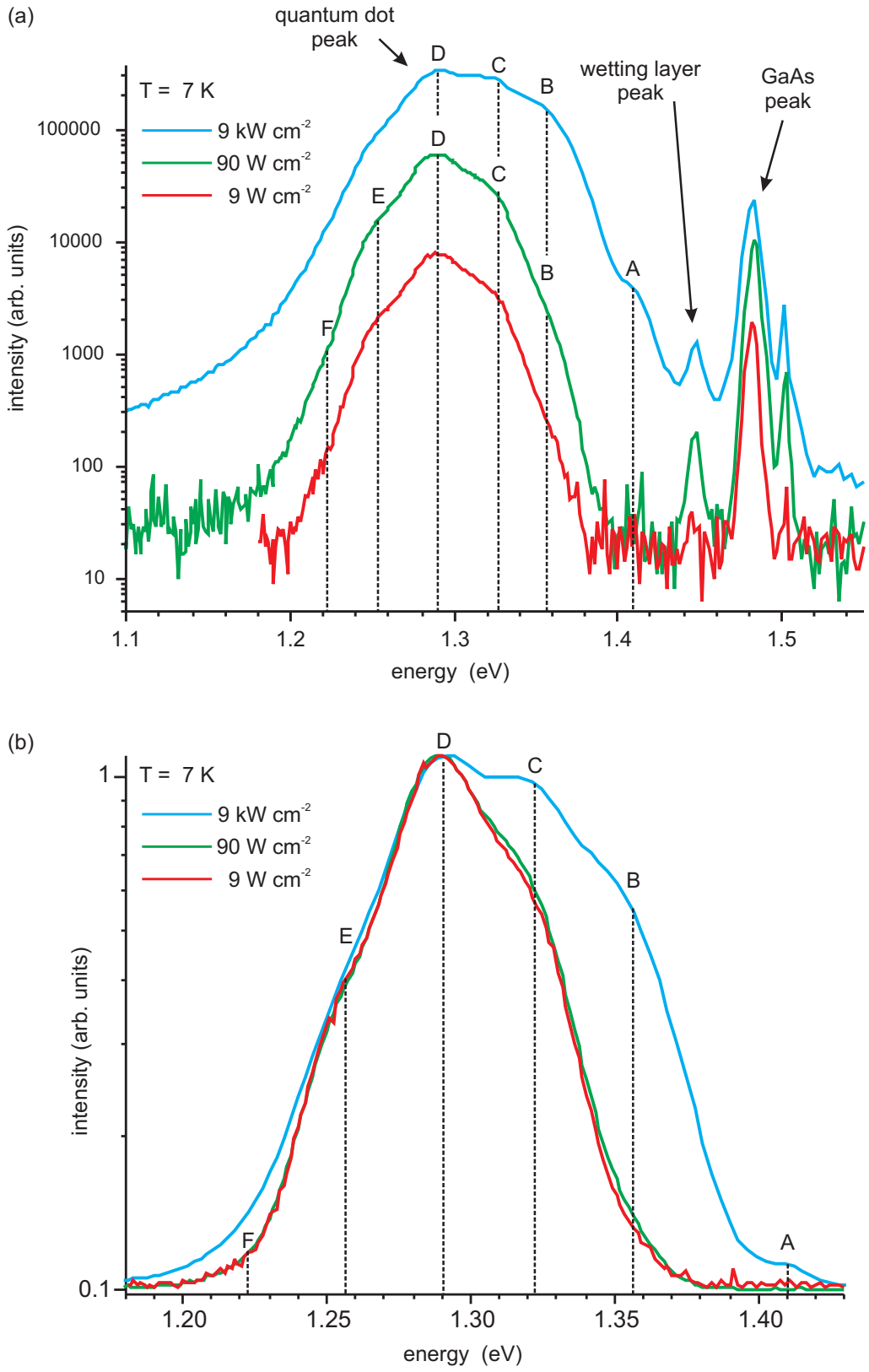

FIGURE 5.30: PL spectra of sample I (b), containing 1.8 ML InAs deposited at 450°C and grown on semiisolating substrate, taken at 7 K with different excitation densities. (a) Overview spectra showing a broad quantum dot peak around 1.29 eV, a wetting layer peak at 1.44 eV, and GaAs peaks above 1.48 eV. (b) Normalized display of the quantum dot PL in order to compare the three curves; peaks at position B−F are assigned to the quantum dot ground states of subensembles with different heights, and A−C also to quantum dot excited states.

mixing of the quantum dot material was found, with a maximum indium content varying between 55 and 90% and an averaged one of about 70%. These findings and a possible change of the indium distribution towards a reversed cone profile, which was found especially for larger quantum dots, will lead to shifts in the PL ground state emission towards higher energies in comparison to pure InAs quantum dots. Considering an estimated value of the above described energy shift of up to 200 meV [22], the observed PL peaks can be connected to intermixed InAs quantum dots with heights ranging from 8 ML (B) to 12 ML (F).

Thus the observed PL spectra can be explained in connection with theoretical investigations and the XSTM results as a multimodal distribution of intermixed InAs quantum dots, demonstrating the benefit of size and stoichiometry investigations on buried quantum dots.

5.5 Discussion and overgrowth model

After presenting structural results derived from STM, XSTM, and TEM as well as the optical properties studied by PL, a collection of all quantum dot parameters is presented in Table 5.1. All these findings will be discussed in this section, by comparing them with earlier results and afterwards presenting a model for the overgrowth process.

5.5.1 General growth characteristics

The general characteristics at the different growth conditions can be concluded as follows: The size of the quantum dots grown at 450°C increases with increasing amount of deposited material, while the density decreases. More difficult is the observation of the quantum dot height, due to the fact that in XSTM images only every second ML in growth direction can be imaged, and because TEM could not detect quantum dot heights for low InAs exposure. Nevertheless a slight increase in height from 2−3 to 3−4 atomic chains can be derived from structural results, which is further confirmed by the PL data considering the energy shift from 1.29 eV to 1.13 eV correlating with a red-shift of the quantum dot wavelength from 0.98 μm to 1.10 μm (see Table. 5.1). In the case of pure InAs quantum dots, such an energy reduction of the ground state emission of about 160 meV is comparable with an increase of the quantum dot height of about 5 ML [144] or 2-3 atomic chains.

The deposition of 1.8 ML InAs at lower growth temperature (420°C instead of 450°C) leads to small quantum-dot like structures and wetting layer fluctuations, which are connected to a broad luminescence peak and not to a typical PL signal of distinctive quantum dots. The density of these quantum-dot like structures is almost identical to the one found with top-view STM for the quantum dots grown at 450°C. Thus it may be assumed that the lower growth temperature preserves the density of quantum-dot like structures during overgrowth, while at higher temperatures the faster kinetics may lead to coalescence of some neighboring quantum dots and therewith to a reduced density by a factor three.

InAs amount and growth temperature	method	InAs quantum dots					InAs WL		PL energy	
		QD #	base-length	height	density	max. InAs content	thick-ness	max. InAs content	QD	WL
[ML] @ [°C]			[nm]	[nm]	[cm^{-2}]	[%]	[nm]	[%]	[eV]	[eV]
1.8 @ 450	top-view STM	498	5−20 (12.5)	2−3 (2.8)	19					
	XSTM	28	10−17 (12)	2−3	6.0	55−90 (80)	3−4	25−30		
	TEM		10−20	2−3		≥27	1.8	≥27		
	PL								1.29	1.44
2.2 @ 450	XSTM	12	12−25 (17)	3−4	2.2	70−90	3−4	20−25		
	TEM		10−20	2−3		≥27	1.9	≥27		
2.6 @ 450	XSTM	3	16−23 (19)	3−4	2.0	75−100	3−4	20−25 (18)		
	TEM		14−19	2.6		≥35	2.3	≥27		
3.0 @ 450	XSTM	0								
	TEM		15−22	2.8		≥28	2.4	≥27		
3.6 @ 450	XSTM	6	20−25 (22)	3−4	1.5	80−100	3−4	25−30		
	TEM		18−24	2.9		≥28	3.0	≥23		
	PL								1.13	1.43
1.8 @ 420	XSTM	8	5−17 (7)	2−3	20	50−90	0−4	15−40		
	PL								–	1.40

TABLE 5.1: Overview on the structural data of InAs/GaAs quantum dots and corresponding PL energies. The data in brackets represents the typical value of the above parameter range.

5.5.2 Changes during capping

The shape of the free-standing quantum dots is found to be pyramidal [49, 113, 120] also for increasing quantum dot sizes (see Xu et al., Ref. [114]). Top-view STM investigations in the case of larger quantum dots observed a strain limitation of the quantum dot base-length, leading to steeper side facets for larger quantum dots, but still dominating {137} side facets were observed on top. Thus the shape of these quantum dots before capping is still pyramidal, which also agrees with the results from a recent theoretical analysis [29].

In the investigation of capped quantum dots pyramidal shapes are never found. All observed capped quantum dots and quantum-dot like structures show a truncated shape

with an (001) top facet, which is most clearly observed for quantum dots with large material amount, as shown in section 5.3.2. It should be noted that a (001) top facet was also observed for capped InGaAs quantum dots [116, 136], InAs quantum dots [76, 117, 145], as well as for GaSb quantum dots [98]. Such a transition during capping towards a truncated (001) top facet is also known from Ge quantum dots capped with Si [128].

The side facets change upon capping from {137} facets to steeper ones like {101} or {111}, which is a similar behavior as found for the Ge/Si-system [134]. A further confirmation for a structural change of the quantum dots during overgrowth are the observed PL data, which can be assigned to subensembles of intermixed InAs quantum dots [91, 144]. However, the quantum dot heights derived from PL under assumption of pure InAs quantum dots are considerably smaller than those found in XSTM, but could be explained by the observed reduced indium content and changes in the indium distribution.

5.5.3 Overgrowth model

The comparison of the structural results of the uncapped and capped quantum dots leads to the following overgrowth model, shown in Fig. 5.31. In order to keep the model as simple as possible only the indium (red) and gallium (cyan) atoms are shown.

The overgrowth process starts with the pyramidal quantum dot shape (a), as derived from the uncapped quantum dot structure [113, 127] and indicated by the yellow contour line. The highest strain in this system is found at the bottom edge of the quantum dot, while the apex is almost relaxed [46] with a local lattice constant close to the one of bulk InAs.

Consequently the gallium atoms from the first ML GaAs cap will not be incorporated at the quantum dot top due to the large lattice mismatch, but they drag the indium atoms from the apex to the quantum dot edges, as indicated by the red arrows (b). This segregation of the indium atoms from the apex to the side flanks will reduce the lattice mismatch on top of the quantum dot and lead to the later observed steeper side facets. A segregation-induced exchange of indium and gallium at the wetting layer reduces the strain and the lattice mismatch, since an intermixed wetting layer is energetically more favorable than a pure InAs wetting layer. During further overgrowth the gallium atoms will easier be incorporated into the InGaAs wetting layer and only afterwards at the quantum dot [Fig. 5.31 (c)]. The indium segregation of the wetting layer is indicated in (c) by the red arrows, while the intermixing of gallium and indium at the quantum dot top is shown by the cyan arrows. After completing the overgrowth of the wetting layer the quantum dot is further capped starting at its sides [Fig. 5.31 (d), cyan arrows]. In addition indium atoms from the strained quantum dot sides segregate to the upper side flanks as indicated in (d) by the red arrows. In this way the reversed-cone indium distribution develops, especially observed for quantum dots containing higher indium amounts. Finally the shape of the quantum dot has changed from a triangular to a truncated shape as indicated by the black background (e). The resulting quantum dot

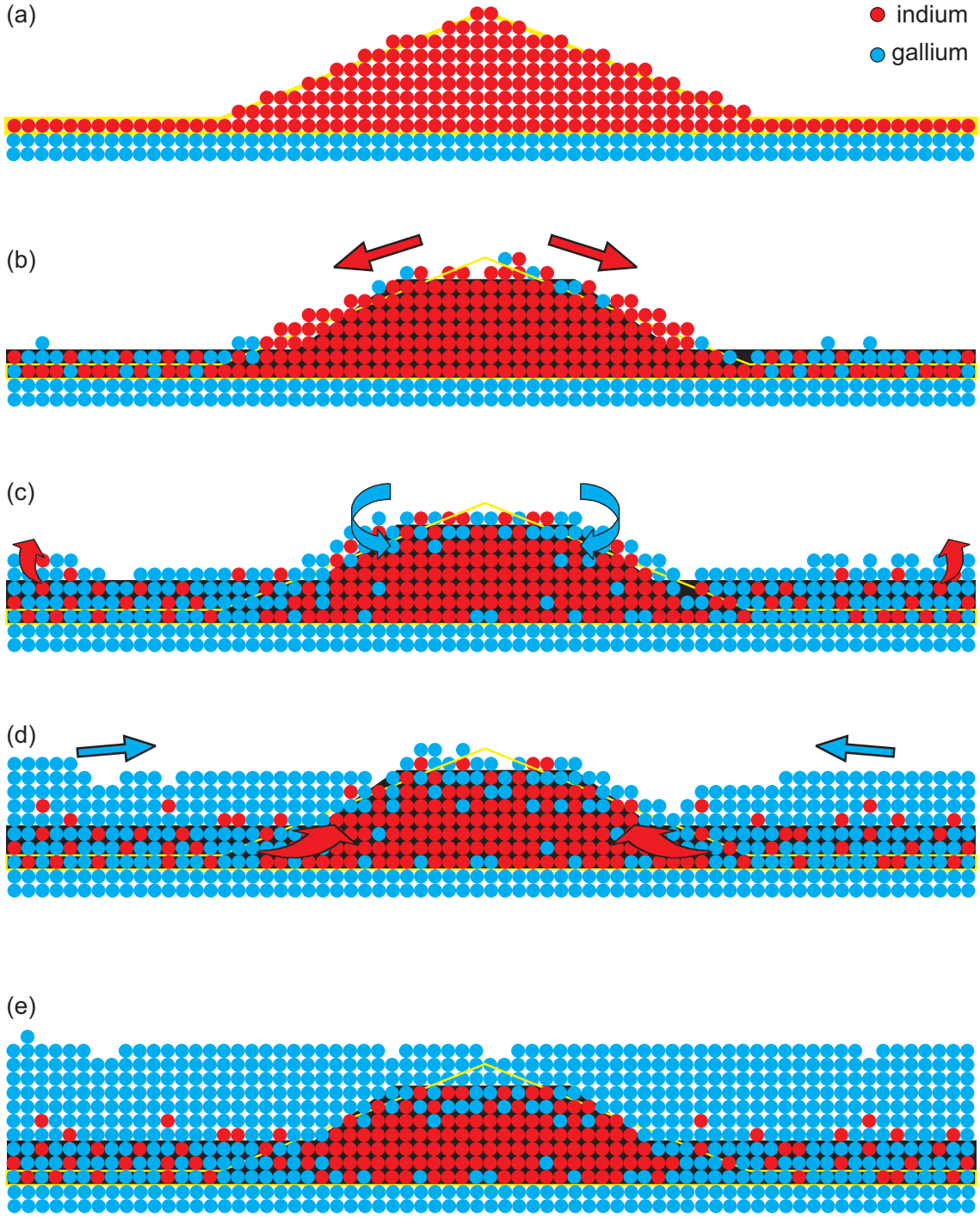

FIGURE 5.31: Atomistic model for the overgrowth process, with indium atoms in red and gallium atoms in cyan. Arsenic atoms are not drawn in terms of simplicity. The yellow contour line indicates the uncapped quantum dot shape and the black background the finally resulting shape of the quantum dot and the wetting layer. Colored arrows indicate indium and gallium segregation. (a) Triangular cross-sectional quantum dot shape derived from the uncapped quantum dot model. (b) Initial GaAs cap layer deposition: The gallium atoms will not be incorporated at the top of the quantum dot due to the large lattice mismatch, but may drag the indium atoms from the apex towards the edges. (c) Gallium atoms are at first incorporated at the surrounding InAs wetting layer and afterwards at the quantum dot, resulting in intermixing of indium and gallium especially at the wetting layer, but also at the quantum dot top. (d) Overgrowth of the quantum dot from its surrounding and already capped intermixed wetting layer. (e) After the overgrowth process: Truncated pyramidal quantum dot shape with steeper side facets and reduced indium content in the quantum dot and wetting layer.

shape has steeper side facets, is located in an intermixed wetting layer and contains a reduced stoichiometry, as observed by XSTM.

This overgrowth model explains the structural changes of the quantum dots during capping under consideration of the strain due to the lattice mismatch. It shows the transformation from the pyramidal to truncated shapes with (001) top facets. Consequently a change from {137} side facets to steeper ones like {101} or {111} occurs, and the model explains further the reduced stoichiometry and the indium distribution as well as the intermixed wetting layer.

5.5.4 Discussion

The observation of the structural changes of quantum dots during overgrowth and the presented growth model correlate well with already existing observations of the capping process in the InAs/GaAs system.

First investigations of InAs quantum dots capped with GaAs were performed with a combination of structural and optical methods [27, 146]. Changes of the shape and the composition of the quantum dots during initial overgrowth stages were observed with AFM and PL [146], but due to the limited resolution of the analyzing method no final conclusions could be drawn. The influence of the capping layer was further investigated by a combination of STM, AFM, plane-view and cross-sectional TEM under consideration of the overgrowth temperature [27]. It was observed that only for the growth of low temperature GaAs cap layers, definitely thicker than the quantum dot height, the quantum dots remain after capping. Otherwise a reduction in the quantum dot height and density as well as a dissolution of quantum dots was observed [27], indicating strong structural changes during overgrowth.

Recently Costantini et al. investigated with top-view STM and AFM the capping process of large InAs quantum dots (so-called dome structures) by GaAs [30, 147]. A backward evolution was determined, starting with large quantum dot domes transforming to pyramids and resulting in truncated pyramids with reduced heights and (001) top facets. After these structural changes of the quantum dots, the actual overgrowth of the quantum dots followed. An additional theoretical investigation on the formation of a truncated pyramid during overgrowth was presented by Hammerschmidt [148]. In this work the cohesive energies for InAs pyramids with {101} side facets and different baselengths and heights were calculated, resulting in large baselength and small heights and thus agrees well with the observed truncation of the quantum dots found with XSTM.

The existence of the two capping regimes predicted by Costantini et al. is also confirmed by the present XSTM results and the related overgrowth model. The segregation-induced exchange of indium and gallium atoms in the wetting layer reduces the strain energy and leads to a predominant incorporation of the following gallium atoms into the wetting layer. Finally, at sufficient GaAs height above the wetting layer the quantum dots are overgrown from their surrounding, since the formerly strained quantum dot apex has reduced its strain energy by the change from a pyramidal to a truncated shape as well as

due to intermixing effects.

In conclusion, the comparison of uncapped and capped quantum dots grown in the same MBE chamber and under the same growth conditions demonstrates that the quantum dot structure changes during the overgrowth process from pyramidal to truncated shapes. Due to strain energy minimization the quantum dot apex dissolves and steeper side facets form. Intermixing effects result in a reduced stoichiometry in the quantum dot and the wetting layer. These findings are further confirmed by the comparison of quantum dots with increasing sizes, which always show pyramidal shapes in top-view STM, but after overgrowth exclusively truncated shapes are observed. In addition, for these larger quantum dots the indium-rich center develops towards a reversed-cone shape.

Chapter 6

InAs quantum dots with antimony surfactant

Having understood the principal shape transition of quantum dots during overgrowth, now a strategy to directly influence the final quantum dot shape is investigated. In order to reach the technologically important lasing wavelength of 1.3 μm, the influence of antimony offered during InAs quantum dot growth is studied. Antimony may react in highly strained systems as a surfactant, which increases the critical thickness for quantum dot formation and leads to larger and still coherent quantum dots [53, 149, 150]. The surfactant behavior of antimony is characterized by floating antimony at the growth surface, which influences the InAs quantum dot growth but is not incorporated into the quantum dots. The influence of antimony exposure during different growth stages is analyzed in this chapter.

6.1 InAs:Sb sample structure

The investigated sample was grown with MOCVD on GaAs(001) by K. Pötschke in the group of Prof. D. Bimberg at the TU Berlin. For the growth trimethylindium, trimethylgallium, trimethylaluminum, tertiarbutylarsine, and triethylantimony were used with a As/Ga ratio of 15, As/In ratio of 1.5, and Sb/As ratio of 0.12, resulting in an Sb/In ratio of 0.175. The sample contains four quantum dot layers, each with nominal 1.8 ML InAs, and all layers are embedded in an AlGaAs/GaAs buffer and cap layer, as shown in Fig. 6.1.

The growth of each quantum dot layer starts with a 120 s long growth interruption (GI), during which the growth temperature was reduced from 600°C to 485°C under arsine flux in order to stabilize the growth surface. The quantum dot growth of layer 1 was performed with antimony supply. After the quantum dot growth and a further 5 s growth interruption the quantum dots were capped by 12 nm GaAs at the same temperature, before the temperature was raised to 600°C to grow further GaAs. Afterwards layer 2 was equally grown starting with a 120 s GI, followed by InAs quantum dot growth with antimony and 5 s GI, during which antimony was supplied as well. Layer 3 is equal to layer 1 expect that antimony was already offered during the last 15 s of the GI prior to

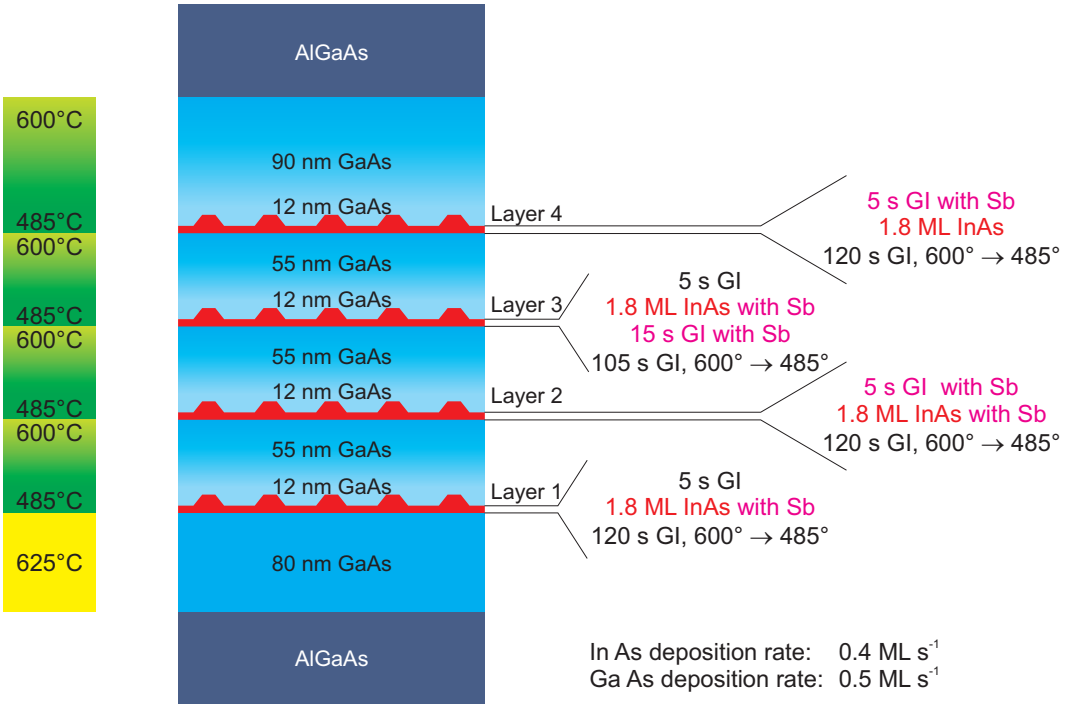

FIGURE 6.1: The investigated InAs:Sb sample structure. Antimony is offered at different growth stages: At layer 1 during quantum dot growth, at layer 2 during quantum dot growth and the following growth interruption, at layer 3 prior to the quantum dot growth, and at layer 4 only during the mentioned growth interruption.

the quantum dot growth. Finally in layer 4 antimony is only offered during the GI after the quantum dot growth, while the growth process is otherwise equal to layer 2.

For PL and TEM measurements additional samples were grown under the same growth conditions as layer 1, 2, and 4, but on undoped substrates and with thinner cap layers. Furthermore a reference sample without any antimony was grown.

6.2 XSTM results on InAs:Sb quantum dots

An overview image of all four layers with bright quantum dots found at layers 1 and 2 is shown in Fig. 6.2. Unfortunately layers 2−4 are located at surface steps, representing a typical cleavage phenomenon during XSTM experiments. Due to similar steps in most images detailed XSTM data could only be taken at layers 1 and 3, and to a limited extent at layer 2. The calculated quantum dot densities amount to about 6×10^{10} cm^{-2}, 4×10^{10} cm^{-2}, and 3×10^{10} cm^{-2} for layers 1, 2, and 3, respectively. At the sides of the overview image the AlGaAs/GaAs interfaces are visible due to a rougher appearance of the AlGaAs surface. Even under UHV conditions, rest gas chemisorption takes place, and on the Al containing compound the chemisorption has a much higher rate than on GaAs, leading to this rough and unstructured appearance of the AlGaAs layers [151].

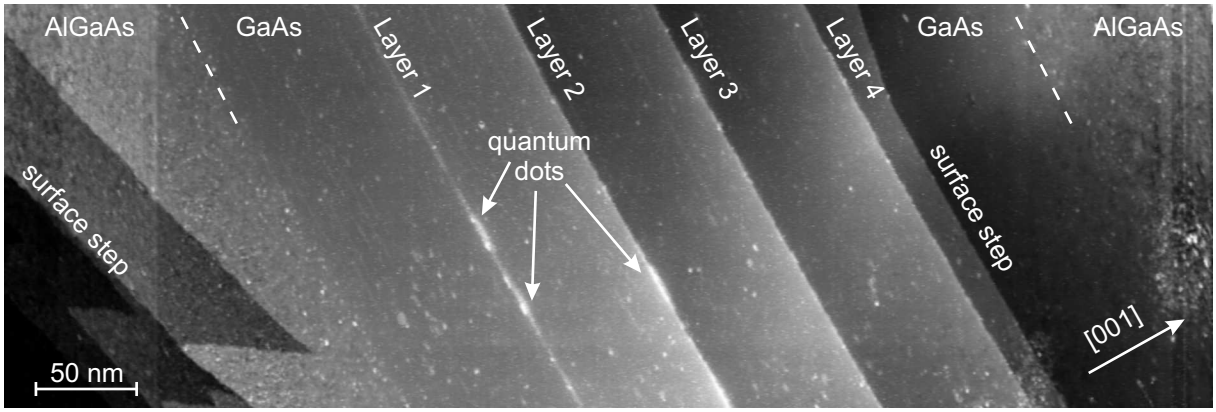

FIGURE 6.2: XSTM overview image of the AlGaAs cladding layers and the InAs:Sb layers 1 to 4, taken at $V_S = -2.8$ V and $I_T = 110$ pA [152].

6.2.1 Quantum dot growth under antimony supply

Typical quantum dots of layer 1 are presented in Fig. 6.3 (a−c) and Fig. 6.4 (a). The observed quantum dot size varies laterally between 10 and 25 nm and amounts to 1−3 nm in height. A small quantum dot with a rather pyramidal shape is imaged in Fig. 6.3 (a), while flat top facets are more frequently observed, as shown in (b, c). The quantum dot shapes are indicated by the dotted contour lines, and the measured angles between the quantum dot baselines and their side contour lines amount to about 35° indicating {101} side facets. Quantum dots with larger sizes always have a flat {001} top facet, as shown in Fig. 6.4 (a). The origin of this behavior may be the position of the cut through the quantum dots. Assuming truncated pyramidal quantum dot shapes with low index side facets, different cleavage positions e.g. parallel to the quantum dot diagonal will lead to

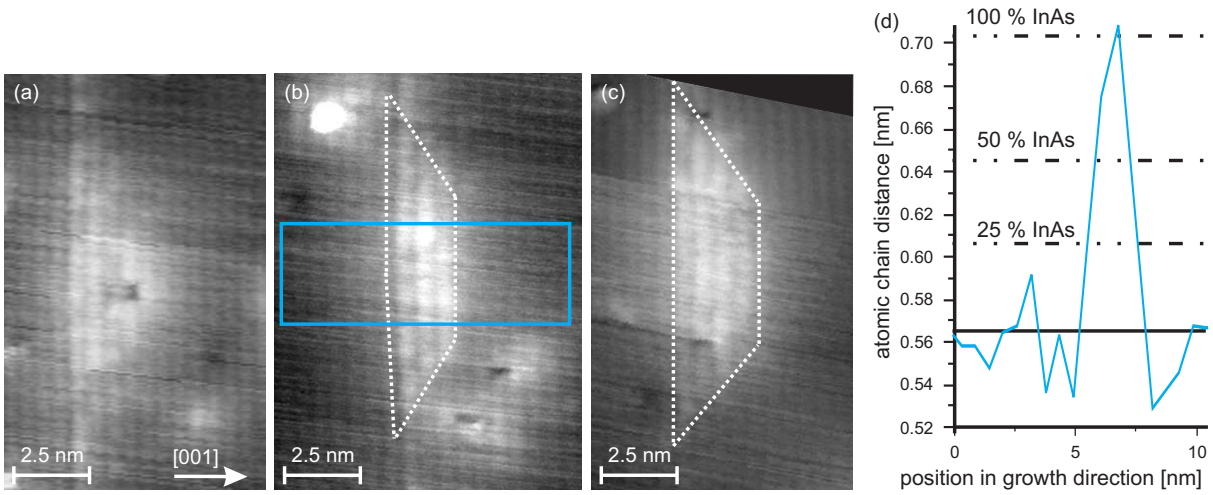

FIGURE 6.3: XSTM images of different quantum dots of layer 1. (a) A quantum dot with a rather pyramidal shape and (b, c) quantum dots with a flat top facet. Their possible shapes are indicated by the dotted contour lines. All three quantum dots show a rather homogeneous indium distribution and were imaged at $V_S = -2.7$ V and $I_T = 80$ pA. (d) Local stoichiometry determination of the quantum dot imaged in (b), amounting to about 100% InAs.

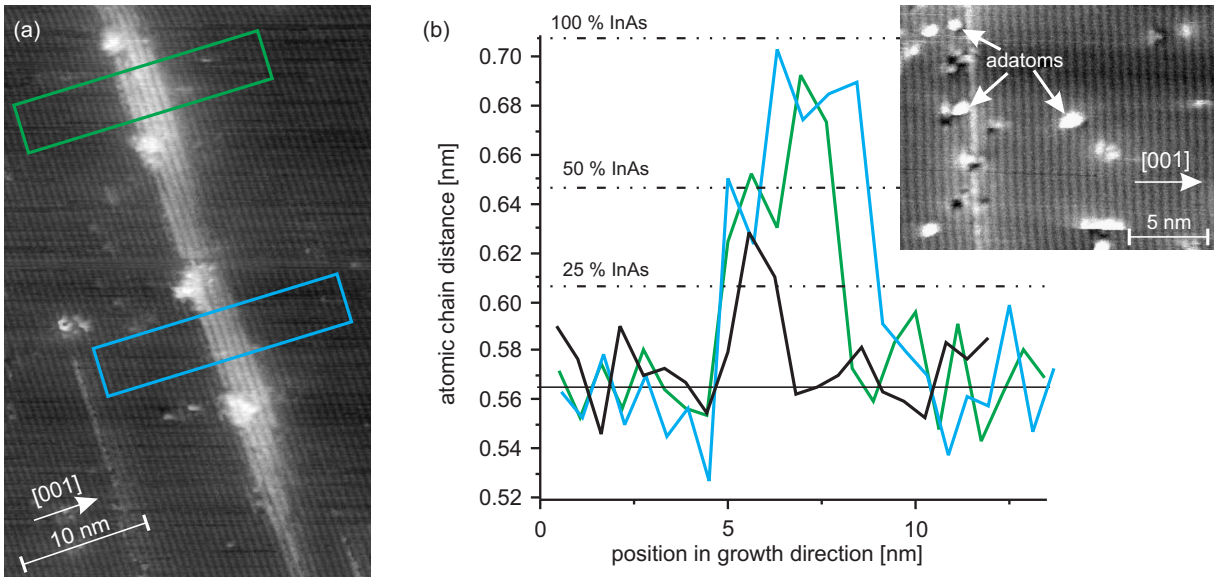

FIGURE 6.4: (a) XSTM image of two large quantum dots of layer 1, taken at $V_S = -2.4$ V and $I_T = 100$ pA. (b) Local stoichiometry determination of the quantum dots, performed along the colored boxes in (a), amounting to about 100% InAs. For the wetting layer (black curve) an amount of about 40% InAs derived for the region shown in the XSTM inset image, taken at $V_S = -3.0$ V and $I_T = 100$ pA.

such an observed distribution of cross-sections with small pyramidal shapes and larger trapezoidal ones indicating {101} side and {001} top facets.

Independent from the different sizes all quantum dots show a very homogeneous indium distribution. Importantly no antimony incorporation is observed [153]. It should be noted that at the negative sample polarity antimony atoms should clearly be visible due to the atom-selective contrast mechanism (section 4.4). Thus the result of the stoichiometry determination of the quantum dot in Fig. 6.3 (b) can directly be connected to an InAs amount of about 100%, as shown in (d).

A very similar result is also obtained for larger quantum dots, like the ones imaged in Fig. 6.4 (a). The quantum dot centers consist of almost pure InAs (green and cyan curve), while the wetting layer (black curve) far away from the quantum dots reaches only about 40% InAs composition [153]. The wetting layer shown in the XSTM inset image of (b) is found to be significantly smaller compared to the InAs wetting layer discussed in chapter 5 (Fig. 5.12) or to the results found in earlier XSTM investigations of InAs quantum dots grown without antimony supply [111, 154, 155]. Antimony supply during the InAs quantum dot growth seems to prevent segregation effects of the wetting layer. This behavior may be connected to floating antimony, which means antimony atoms that are not incorporated in the lattice but remain at the growth surface [98]. It changes the surface energy and is limiting the diffusion rates [53]. Accordingly floating antimony may suppress indium segregation, leading to well defined quantum dots with nearly pure indium content.

6.2.2 Additional antimony during the following growth interruption

The quantum dots at layer 2 were also grown under antimony supply, but antimony was additionally offered during the following growth interruption. All observed quantum dots are located directly at a surface step, so that the determination of the size, shape, and stoichiometry is more difficult.

Two typical quantum dots with baselengths of 17−20 nm and heights of 2−3 nm are shown in Fig. 6.5 (a, b). The shape is indicated by the dotted contour lines and the top facet is restricted by the surface step, parallel to the wetting layer and the quantum dot base. Thus a flat {001} top facet can be assumed. The surface step is also cleaved along the quantum dot side, due to the larger strain surrounding the quantum dots. The measured angle of the quantum dot contour line to the baseline amounts to about 34° indicating {101} side facets, as already observed at layer 1. From the visual impression pure InAs quantum dots are assumed. However, a determination of the local lattice constant cannot be performed at these quantum dots due to the high surface step leading to strain relaxation and the minor resolution.

The images of the wetting layer at a surface step [Fig. 6.5 (c)] and also on the flat surface (d) indicates a thickness of 1−2 atomic chains. This may be slightly more than observed at layer 1, but is still very thin compared with an InAs wetting layer without antimony supply.

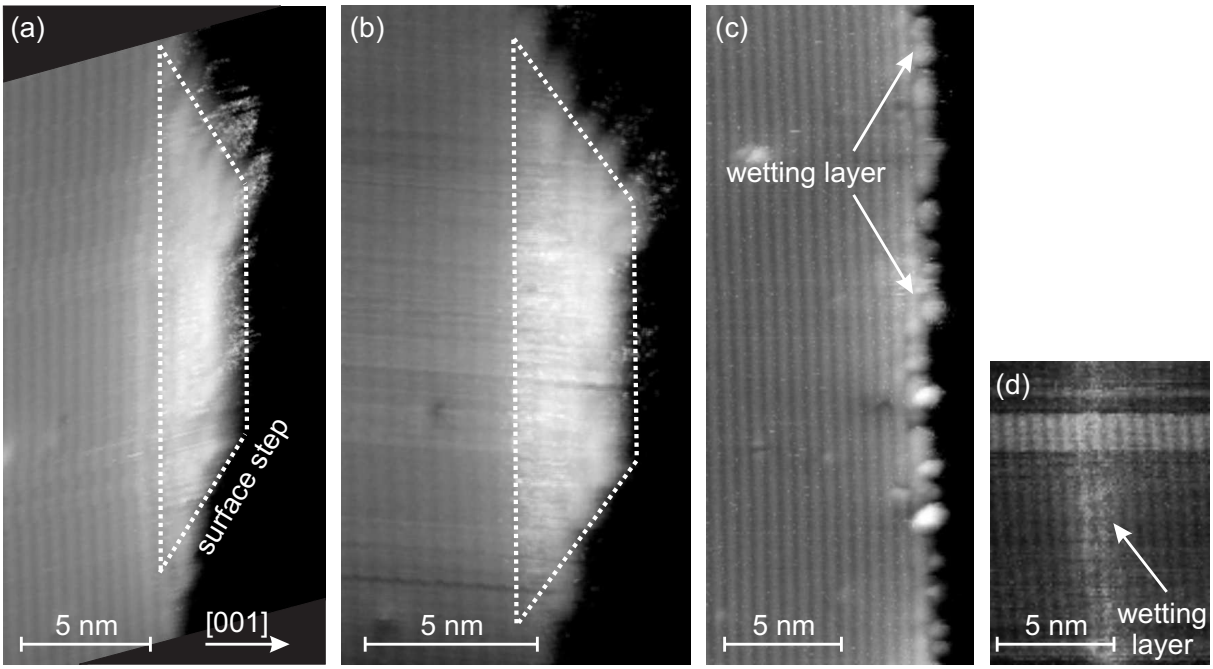

FIGURE 6.5: XSTM images of layer 2 taken at $I_T = 100$ pA. (a, b) Quantum dots located at a surface step, taken at $V_S = -2.3$ V and $V_S = -2.0$ V. The quantum dot shape is indicated by the dotted contour lines. (c, d) Thin wetting layer, taken at $V_S = -2.2$ V and $V_S = -2.7$ V.

6.2.3 Antimony supply prior and during quantum dot growth

For the growth of the InAs quantum dots at layer 3, antimony was offered already during the last 15 s of the growth interruption prior to the InAs deposition. As shown in Fig 6.6 (a, b), the observed quantum dots of layer 3 have baselengths of 20−35 nm and heights between 2−5 nm and are therewith larger than those observed before. The quantum dot shape is evaluated as a truncated pyramid with flat {001} top facets, and from the contour lines shown in (a) again {101} side facets are assumed.

The indium content and its distribution in the quantum dots at layer 3 depend on the quantum dot height. For a flatter quantum dot [Fig. 6.6 (a)], the observed local stoichiometry reaches about 80−90% InAs at the quantum dot bottom, decreasing in growth direction (e), while for a higher quantum dot (b) a reversed-cone indium distribution is visible. This is in agreement with the results of chapter 5, where a reversed indium distribution is also determined for the case of higher quantum dots. An incorporation of antimony in the quantum dots of layer 3 is not detected, but probably the increase in size is connected with the observed intermixing with GaAs.

The wetting layer extending over 2−3 atomic chains is slightly larger than those of layers 1 and 2. The additional thickness is attributed to an incorporation of single antimony atoms, which can directly be seen in Fig. 6.6 (c) as those atoms with the brightest contrast. If antimony is offered to a GaAs surface during a growth interruption, an antimony-for-arsenic exchange can take place [98, 156, 157], which leads to antimony incorporation and to the increased wetting layer thickness observed here. By counting the atoms an antimony content of about 25% in the InAsSb wetting layer is determined [153].

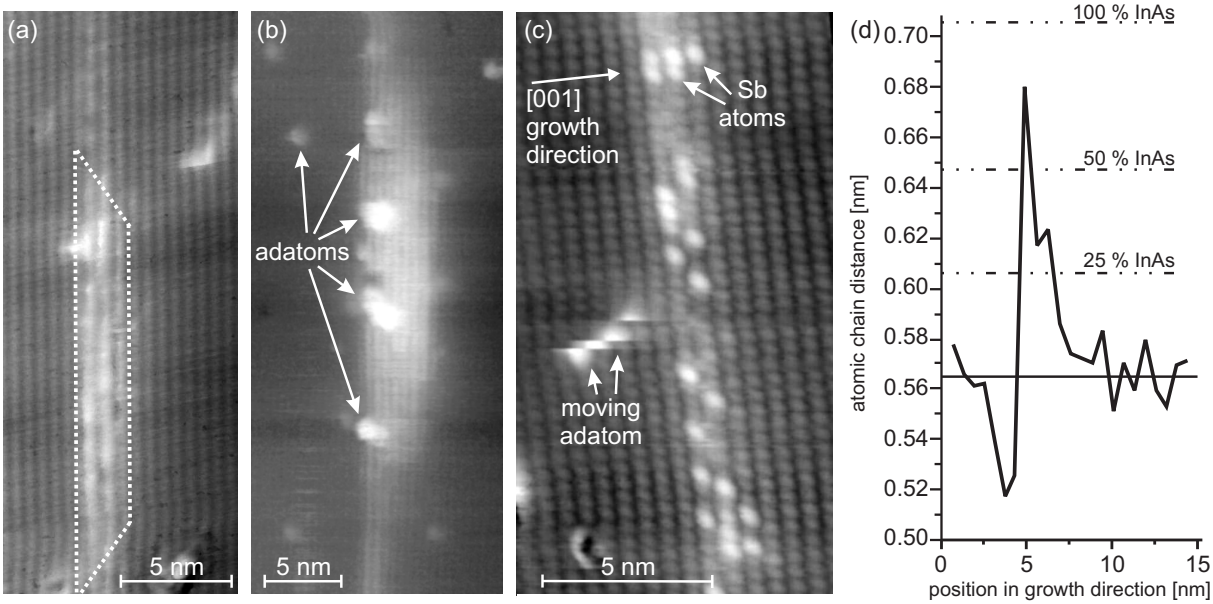

FIGURE 6.6: XSTM images of layer 3. (a) Quantum dot with shape indicated by the dotted line, taken at $V_S = -2.2$ V and $I_T = 80$ pA. (b) Quantum dot taken at $V_S = -2.3$ V and $I_T = 60$ pA. (c) Wetting layer with incorporated antimony atoms, taken $V_S = -2.3$ V and $I_T = 80$ pA [153]. (d) Local stoichiometry determination of the quantum dot in (a) containing 80−90% InAs.

6.3 PL and TEM results of InAs:Sb quantum dots

Photoluminescence spectra of layer 1, 2, and 4 (colored curves) are shown in Fig. 6.7 together with a reference sample without antimony supply (black curve). All layers containing antimony show in comparison to the reference sample a red shift of the ground-state luminescence energy of up to 0.2 eV. The energy is lowest at layer 2, at which antimony was supplied both during quantum dot growth and the following growth interruption. This is in agreement with the XSTM results, showing increasing quantum dot sizes from layer 1 to 3. Furthermore the quantum dots at layer 2 consist of almost pure InAs, which leads to a lower PL energy than in the case of intermixing.

Additionally each spectrum shows pronounced maxima, which are connected to the shell-like growth mode first proposed by Heitz et al. [144]. These multimodal PL peaks with distances between each other of about 40 meV are due to the flat truncated quantum dots with heights varying in discrete monolayer steps, as observed in the XSTM data. Also the well defined interfaces and the negligible In/Ga interdiffusion confirm these PL results, since the spectral broadening, which can be caused by variations of the quantum dot baselength, interface roughness, or composition fluctuations, is much smaller than the energy shifts caused by one monolayer steps of the quantum dot height.

Cross-sectional TEM data of quantum dots of layer 1 and 2 also result in flat quantum dots. Furthermore a reduction of the quantum dot density from layer 1 to layer 2 of about 6×10^{10} cm^{-2} to 2×10^{10} cm^{-2} was observed and confirms as well the growth of larger quantum dots, since the nominally deposited InAs material amount of 1.8 ML remains

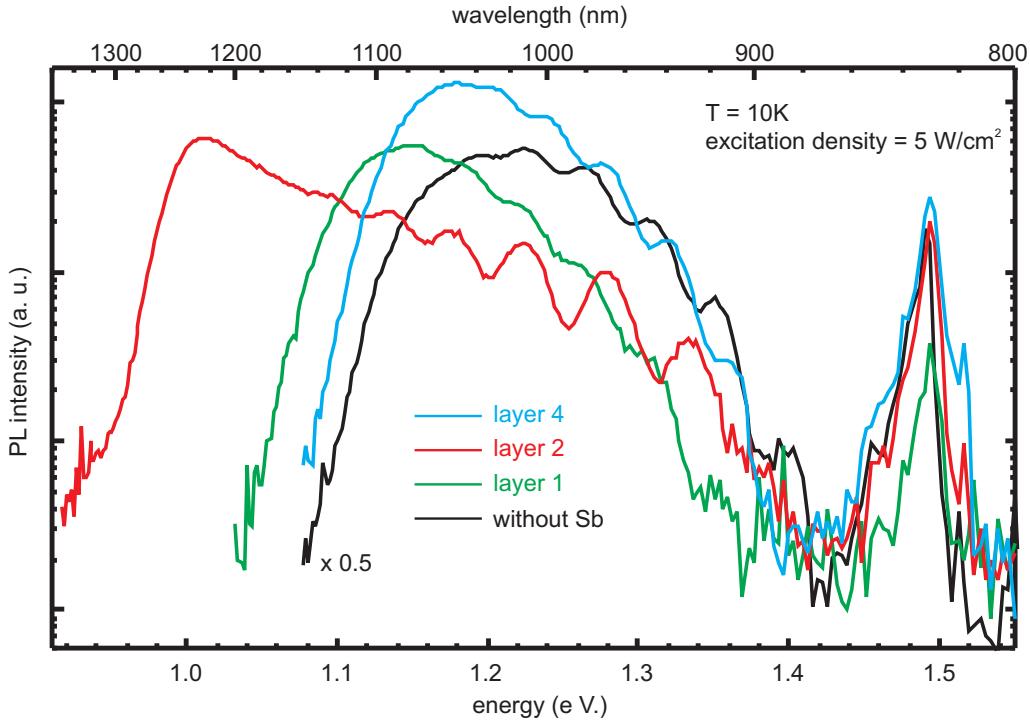

FIGURE 6.7: Photoluminescence spectra from quantum dot samples of layers 1, 2, and 4 (colored curves) in comparison to a reference sample without antimony supply (black curve) [158].

the same.

Additional systematic investigations of the influence of antimony exposure during the growth interruption after InAs quantum dot growth (in analogy to layer 4) also show a red-shift with increasing duration of antimony supply from 0 to 270 s [53]. This red-shift is connected to an increase in the quantum dot size. According to plan-view TEM images a decrease of the quantum dot density by a factor of 2 is determined with increasing duration of the antimony supply from 5 to 90 s.

6.4 Discussion

Structural and electronic results of InAs:Sb quantum dots confirm the surfactant behavior of antimony, leading to larger and more homogeneous quantum dots. The observed quantum dot sizes increase with increasing antimony amount from averaged 10−25 nm to 20−35 nm in width and from 1−3 nm to 2−5 nm in height. The quantum dots grown with antimony supply (layer 1) and those with additional antimony during the following growth interruption (layer 2) contain almost pure InAs, while for those grown with antimony prior to and during InAs growth (layer 3) an inhomogeneous composition with an indium-rich center and intermixed sides is determined. No incorporation of antimony in the quantum dots is found, but at layer 3 an antimony content of about 25% in the wetting layer was determined.

From a comparison of layer 1 and layer 2 it can be concluded that a combination of the higher amount of deposited antimony and the moment of the deposition results in larger quantum dot sizes. Comparing layer 3 with layers 1 and 2 shows, that the more drastic effect of antimony incorporation can be directly connected to the offering of antimony prior to the quantum dot growth. It is known that antimony exposure to a GaAs surface during a growth interruption leads to an exchange of arsenic and antimony [98, 156, 157], resulting in an incorporation of antimony in the GaAs surface. Due to additional antimony supply during subsequent InAs quantum dot growth, these antimony atoms remain in the wetting layer, but do not get incorporated in the quantum dots. This can be related to the compressive strain in the system, which is larger in the quantum dots and smaller in the intermixed wetting layer [153]. Thus the antimony atoms are incorporated into the wetting layer and segregate during further growth and overgrowth.

In conclusion an antimony supply to the InAs quantum dot growth at different growth stages leads in all investigated cases to quantum dots with longer ground state luminescence wavelength. The reason for the red-shift is an increase of both the quantum dot volume and the average indium content as well as distinctive interfaces. It is assumed that antimony decreases the surface energy and hence alters the formation of quantum dots, leading to a lower quantum dot density and larger quantum dot sizes [53, 150]. In addition, the antimony layer seems to prevent intermixing, which is assumed to occur predominantly during overgrowth (see chapter 5), thus leading to larger quantum dots with longer emission wavelengths.

Chapter 7

Limits of quantum dot growth

In the preceding chapter the influence of antimony during InAs quantum dot growth was investigated in order to obtain larger quantum dot volumes with longer emission wavelengths. Other promising methods to achieve longer wavelengths are the overgrowth of InAs or InGaAs quantum dots with an InGaAs layer [159, 160] or the growth of InAs quantum dots in InGaAs quantum wells, the latter being called quantum dots-in-a-well (DWELL) structure [161–164].

Here an XSTM study of such In(Ga)As quantum dot samples grown with MOCVD and MBE is presented. In both cases the quantum dot size increases, but some quantum dots contain a material hole and hence will not contribute to the optoelectronical efficiency of the laser structure. The similarities and differences of the two samples will be investigated, and possible mechanisms leading to these defective quantum dots will be discussed, demonstrating the limits of larger quantum dot growth.

7.1 InGaAs quantum dots overgrown by diluted InGaAs

7.1.1 InGaAs sample structure

The laser diode structure was grown using MOCVD by R. Sellin in the group of Prof. D. Bimberg at the TU Berlin [165]. The sample contains three quantum dot layers, as shown in Fig. 7.1, and each of them was grown as follows: 3−5 ML $In_{0.8}Ga_{0.2}As$ were deposited at 500°C with a growth rate of 1 ML/s, followed by a 60 s long growth interruption for quantum dot formation. Afterwards the quantum dots were covered by 3 nm $In_{0.1}Ga_{0.9}As$ and 2−3 nm GaAs. During the subsequent deposition of 3−4 nm GaAs, the temperature was raised to 600°C. Then a further growth interruption of 600 s was introduced in order to flatten the growth surface and to anneal defects [52, 166]. Finally the quantum dot structures were capped by 20 nm GaAs at a fast growth rate of 21 ML/s before the next quantum dot layer was grown. The thickness of each spacing layer totally amounts to about 24 nm, so that stacking effects of the quantum dots can be excluded [9, 26, 167, 168].

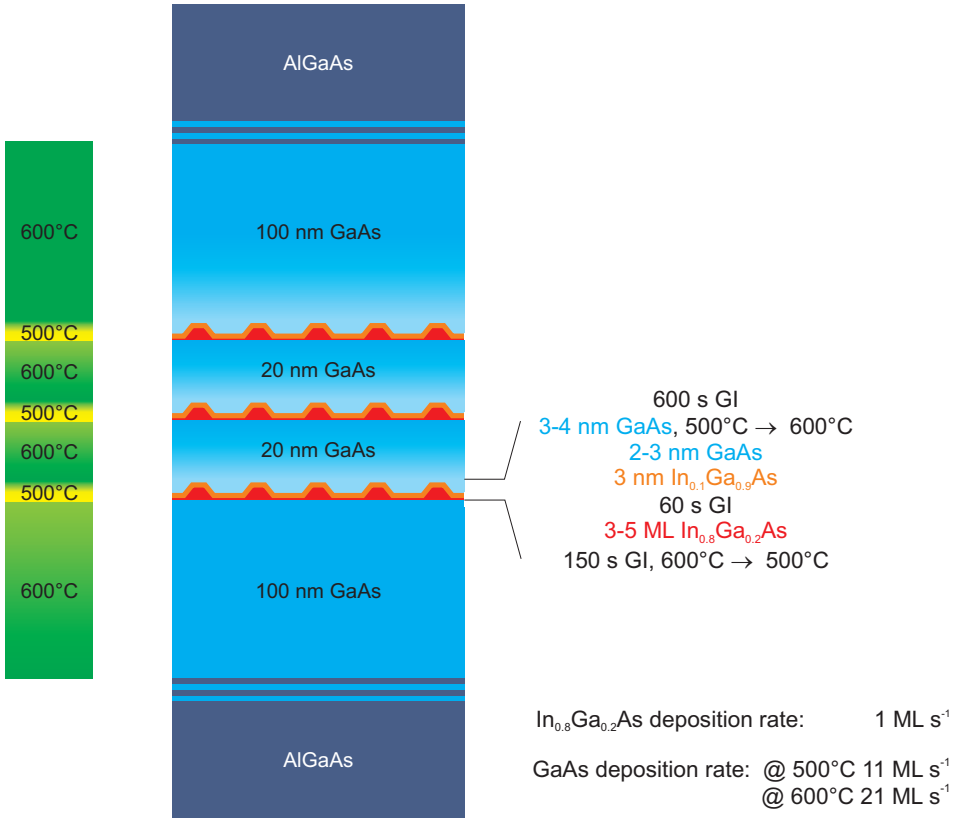

FIGURE 7.1: Investigated sample structure of InGaAs quantum dots overgrown by diluted InGaAs. The sample is grown with MOCVD under arsenic-rich conditions.

7.1.2 General behavior of InGaAs quantum dots

Three different types of quantum dots are found in this sample, as shown in Fig. 7.2. The so-called type-1 quantum dots are imaged as rather oval areas with a bright appearance, type-2 are bright kidney-shaped structures with a concave top, and type-3 quantum dots contain a material hole or nanovoid [136, 169]. Within the investigated scan area extending along 1.2 μm, 60 quantum dots are found in all three layers. The observation rate of the type-1, type-2 and type-3 quantum dots is about 50%, 10%, and 40%, respectively, independent of the quantum dot layer. This corresponds to densities of 3.6×10^{10} cm^{-2}, 4.6×10^{9} cm^{-2}, and 2.9×10^{10} cm^{-2}, respectively. For high quality laser structures a density of more than 4×10^{10} cm^{-2} is tried to achieve [159], which is just reached for both optically active quantum dot types (type-1 and type-2) in this sample.

The measured quantum dot sizes vary laterally between 10 and 20 nm and amount to about 5 nm in height, while the thickness of the rather diluted wetting layer amounts to about 4 nm, which is in good agreement with the nominal value of the total deposited InGaAs material. Consequently the quantum dot thickness differs only little from the wetting layer thickness, which can be seen especially for type-1 quantum dots, while the rims of the type-2 quantum dots slightly stick out of the wetting layer.

The shape of a typical type-1 quantum dot is presented in Fig. 7.3. The dotted contour lines indicate the possible quantum dot shape. The angle between the side contours and

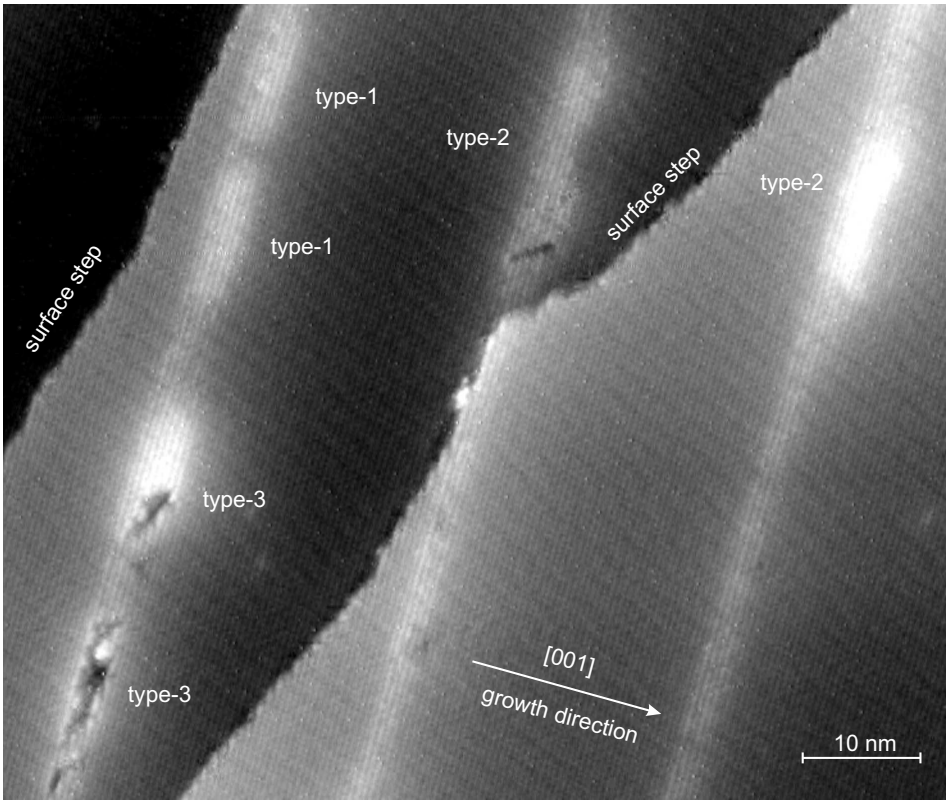

FIGURE 7.2: XSTM overview image of all three observed quantum dot types indicated by type-1, type-2, and type-3, taken at $V_S = -2.3$ V and $I_T = 100$ pA.

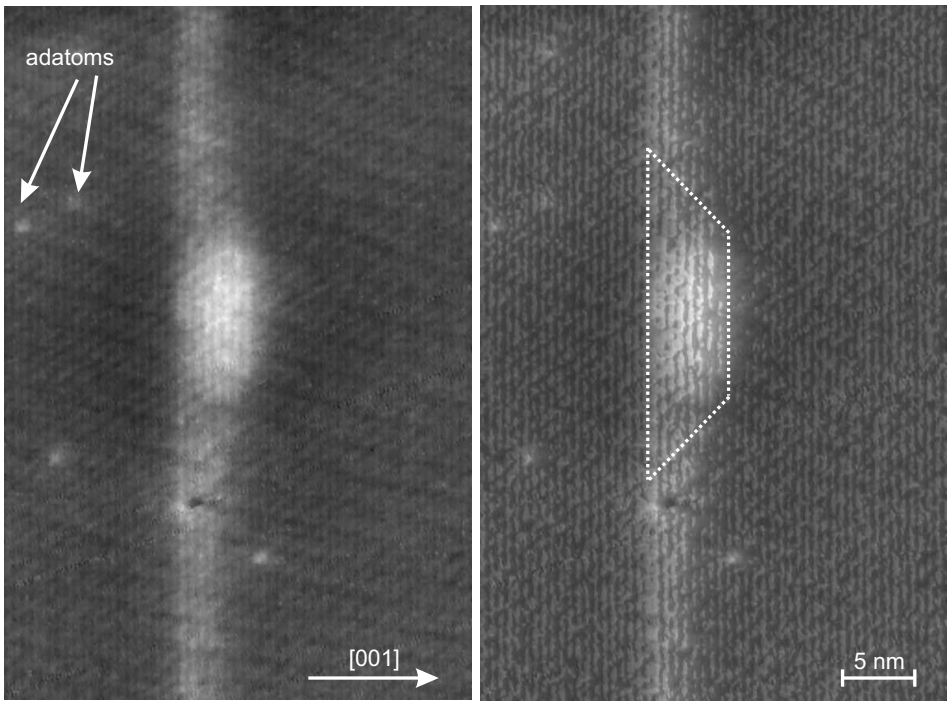

FIGURE 7.3: (a) XSTM image of a type-1 quantum dot and (b) corresponding relief map image, including a possible quantum dot shape, indicated by the dotted contour lines. The image was taken at $V_S = -2.3$ V and $I_T = 100$ pA.

the quantum dot baseline can be determined – with less accuracy than in chapter 6 due to the wetting layer thickness – to about 45° and may belong to {111} or {101} side facets. However, it can be seen very nicely that the region of the highest indium amount is located in the quantum dot center and less at its sides.

7.1.3 Reversed truncated cone indium distribution

In order to analyze the indium distribution of type-1 quantum dots, the local stoichiometry is determined along the colored boxes, indicated in the XSTM image of the inset in Fig. 7.4 (a).

For the quantum dot center a maximum indium concentration of about 60% can be concluded (orange), while the dot sides contain only about 40% (cyan), taking into account the undershoot at the quantum dot baseline. This undershoot again indicates the compressive strain in the quantum dot region, which is higher at the quantum dot center than around its sides and not existing at all for the case of the InGaAs layer. Additionally it can be seen that the indium content increases for the quantum dot center and the sides towards the quantum dot top.

The localization of the highest indium composition in the quantum dot center and the increase of the indium amount from the quantum dot base towards its top clearly demonstrates the reversed truncated cone shape of the indium-rich zone. This is indicated by the dashed red line in Fig. 7.4 (b), while the estimated contour of this quantum dot is indicated by the dotted lines. The brightest contrast and therewith the highest indium amount is observed at the quantum dot top, which is in good agreement with the results of the local stoichiometry determination.

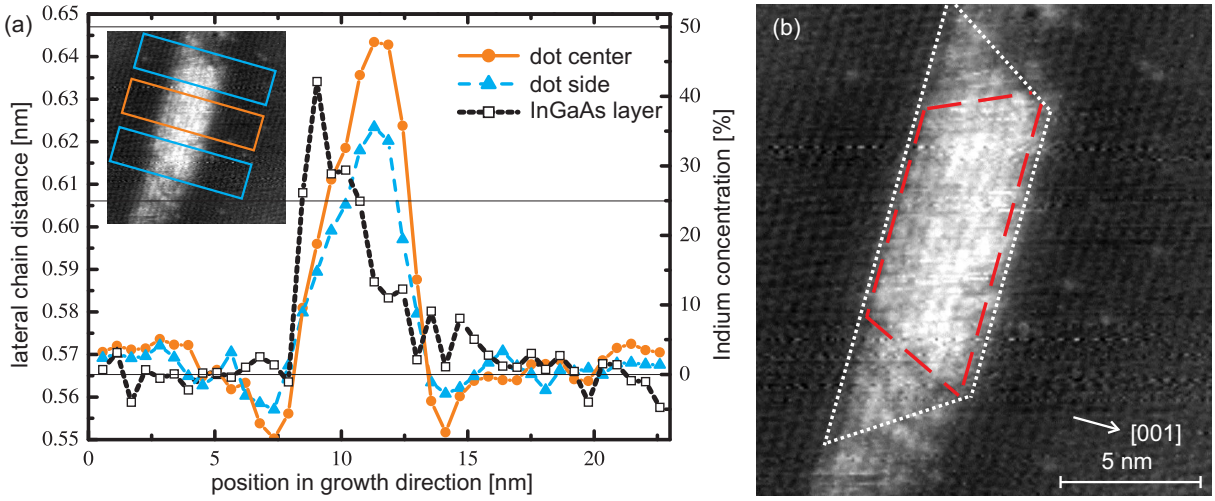

FIGURE 7.4: (a) The local stoichiometry of a type-1 quantum dot, evaluated for the center (orange) and the sides (cyan), as shown in the XSTM inset. The profile of the wetting layer is taken far away from the quantum dots. (b) XSTM image of the same quantum dot with estimated contours indicated by the dotted lines for the whole quantum dot and by the dashed red lines for its indium-rich zone. The image was taken at $V_S = +2.1$ V and $I_T = 80$ pA [136].

A reversed cone distribution was already observed by XSTM and theoretically analyzed for MBE grown $In_{0.5}Ga_{0.5}As$ and InAs quantum dots [116, 117]. Here we found a reversed truncated cone composition distribution, which is formed due to strain minimization during growth and overgrowth. Thus segregation results in a considerable deviation from the nominal indium concentration of 80%.

This strong segregation behavior is further confirmed by the observed vertical intermixing of the $In_{0.8}Ga_{0.2}As$ wetting layer and the $In_{0.1}Ga_{0.9}As$ overgrowth layer, as shown in Fig. 7.4 (a) (black curve). The indium concentration starts at about 40% and decreases almost exponentially along growth direction, in contrast to the nominal growth parameters, and thus indicating a strong indium segregation also at the wetting layer.

7.1.4 Nanovoids in InGaAs quantum dots

After examination of the type-1 quantum dots, in this section type-2 and type-3 quantum dots are investigated, leading to a general growth model for this InGaAs quantum dot sample.

A typical type-2 quantum dot is shown in Fig. 7.5 (a). In comparison to type-1 quantum dots with their flat (001) top facet, the shape of the type-2 quantum dots is characterized by a concave top so that the extension in growth direction in the center of a quantum dot is less than at its sides. Their size amounts laterally to about 20 nm and in growth direction to about 5 nm.

An even more unusual phenomenon is represented by the type-3 quantum dots, which contain a material hole or nanovoid. Figure 7.5 (b, c) shows the same quantum dot at both polarities. The quantum dot has a baselength of about 23 nm, and the observed nanovoid is about 10 nm wide and has an extension along growth direction of about 3 nm. The differences in the nanovoid shape between the arsenic sensitive image (b) and the gallium and indium sensitive image (c) originates from the different tunneling polarities leading to atom selective imaging [67]. The rim of the nanovoid appears much more pronounced at negative sample bias (b), while at positive sample bias the nanovoid appears much broader (c). This difference is quantitatively examined in height profiles across the quantum dot along I and II, displayed in Fig. 7.5 (e, f). Especially the appearance of the left rim and in particular its height vary strongly with the sample bias, indicating an arsenic termination of the inner surface of the nanovoid, as it is also expected from the arsenic-rich growth conditions. The depth of the nanovoid underneath the cleavage surface is at least 0.3 nm (e, f), which is more than a 1 ML high cleavage step, demonstrating that material is actually missing and that the observed depth is limited by the tip shape.

It should be noted that no opposite structures are found, as observed e.g. in the diluted nitride system [170, 171], ruling out the possibility of a cleavage induced artifact. Additionally, no correlation of the nanovoids with surface steps is found, although steps created during the cleaving process are usually crossing the wetting layer at dot positions in order to minimize the strain energy. This behavior indicates a much lower strain in the nanovoids already before cleavage.

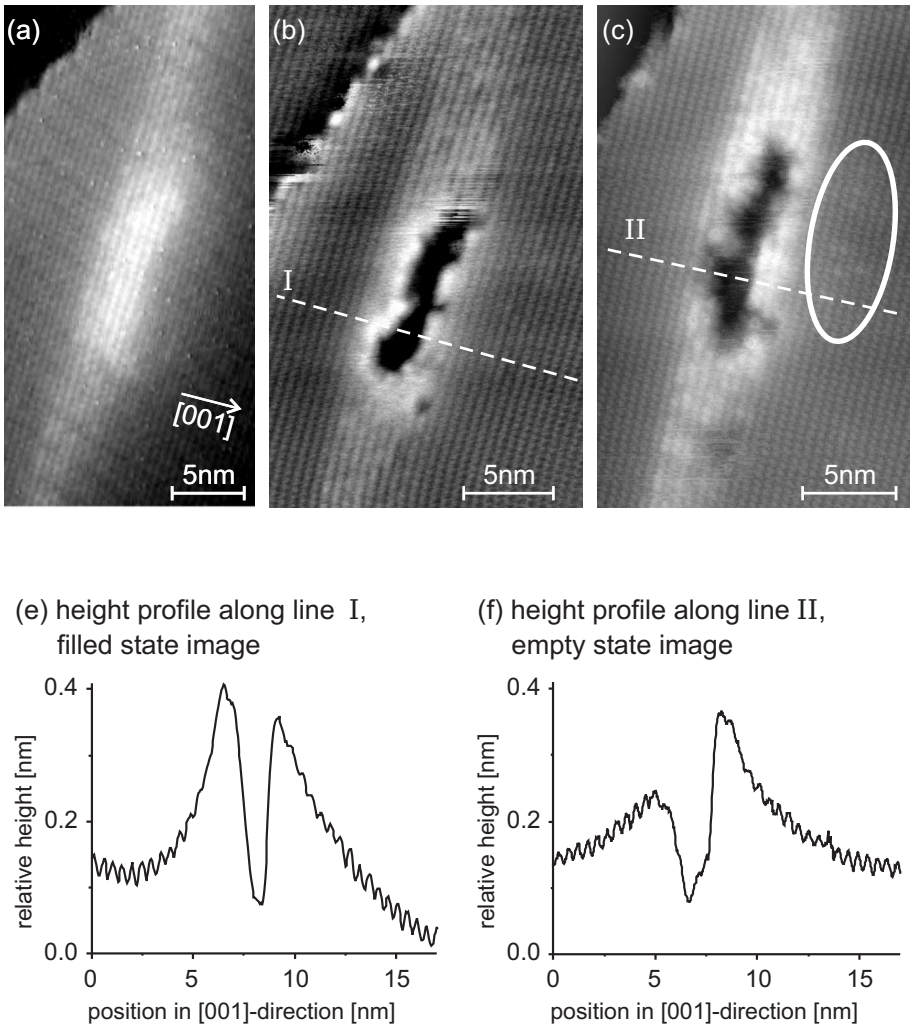

FIGURE 7.5: XSTM images of (a) a type-2 quantum dot, taken at $V_S = -2.3$ V and $I_T = 100$ pA. (b, c) Type-3 quantum dot, taken at $V_S = -2.1$ V, $V_S = +1.8$ V, and $I_T = 100$ pA. (e, f) Corresponding height profiles across the quantum dot along the dashed lines indicated with I and II [169].

In a detailed analysis single indium atoms are found above the wetting layer and the quantum dots, as indicated by the white oval in Fig. 7.5 (c) and pronounced in the corresponding high-pass filtered image, shown in Fig.7.6 (a). These single indium atoms are observed above the nanovoids (a) and also above the wetting layer (b). The distance between the wetting layer baseline and these single indium atoms amounts to about 7−9 nm, which is almost identical with the nominal distance from starting the In(Ga)As deposition up to the position where the 600 s long growth interruption took place (9−11 nm).

The amount of these indium atoms can be evaluated by counting them and comparing this value with the number of gallium atoms perpendicular to the growth direction. In Fig. 7.6 (b) 12 indium atoms in a lateral range corresponding to 73 unit cells are visible. Assuming a homogeneous distribution of the indium atoms and considering that only every second ML in growth direction is imaged, the amount of incorporated indium above the wetting layer results to about 0.3 ML InAs. On the other hand, the amount of missing indium atoms in the type-2 and type-3 quantum dots can be calculated as follows: The volume of missing material is assumed for both types by a cylinder, as shown in Fig. 7.6 (c). Further the size of the missing volume is assumed to be equal for all quantum dots of each type, so that their dimension can be estimated by the largest observed ones, which are

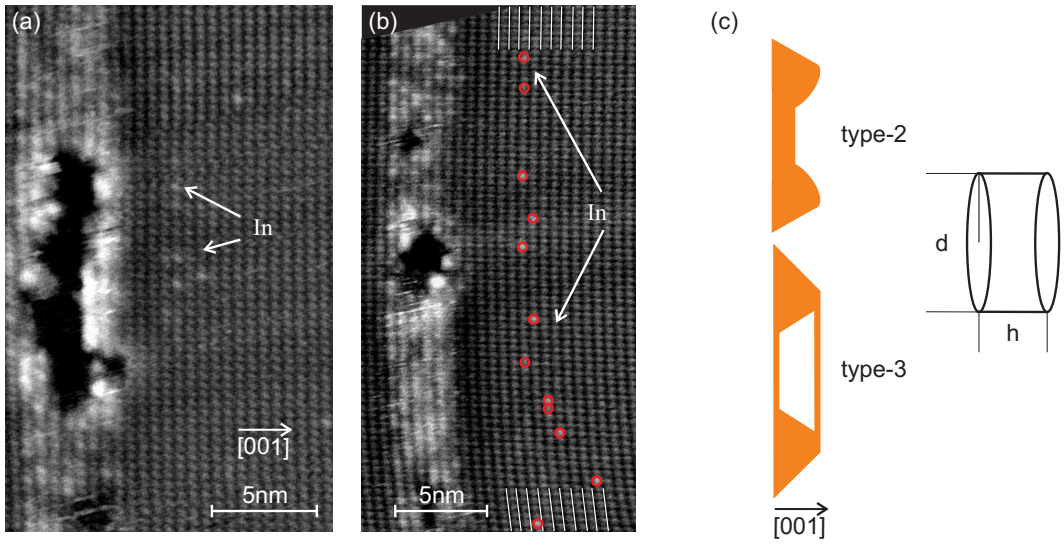

FIGURE 7.6: (a, b) High-pass filtered XSTM images of type-3 quantum dots with pronounce single indium atoms above the quantum dot layer, indicated by red circles in (b). Images taken at $V_S = +1.8$ V, $V_S = +2.2$ V, and $I_T = 80$ pA. (c) Schematic shape of a type-2 and type-3 quantum dot. The volume of missing material is estimated for both types by a cylinder.

probably cut through their centers. The sizes obtained in this way for type-2 (h = 1 nm, d = 7 nm) lead to a missing type-2 volume of about 40 nm^3, while the missing type-3 volume (h = 3 nm, d = 10 nm) results in about 240 nm^3. Taking into account the different quantum dot densities of type-2 (4.6×10^9 cm^{-2}) and type-3 (2.9×10^{10} cm^{-2}), the missing volumes correspond to a homogeneous layer with and average thickness of about 0.7 Å or 0.3 ML, in excellent agreement with the observed amount of indium atoms above the wetting layer.

7.1.5 InGaAs quantum dot growth model

From a recent investigation of InAs quantum dots capped with a thin GaAs layer prior to a 300 s long growth interruption [172] it is known that the critical time scale for an growth interruption changing the quantum dot shape amounts to only a few ten seconds. A longer growth interruption resulted in vertically segregated InGaAs quantum wells, while no distinctive quantum dots could be found. This observation demonstrates the strong influence of a growth interruption during the capping processes.

Hence the three different resulting quantum dots types investigated here can be related to a combination of strong segregation during the 600 s long growth interruption at rather high temperature and insufficient diffusion during the fast overgrowth. The changes in their shape during the overgrowth steps are shown schematically in Fig. 7.7.

The initial deposition of $In_{0.8}Ga_{0.2}As$ quantum dot material and the following 60 s long growth interruption for quantum dot formation leads to a statistical size distribution of the quantum dots as shown in Fig. 7.7 (a). The three different quantum dot types are then forming as follows: During overgrowth of the small type-1 quantum dots by the thin $In_{0.1}Ga_{0.9}As$ layer and a thin GaAs cap layer (b), the indium-rich center develops,

characterized by a reversed truncated-cone shape, as analyzed in section 7.1.3. In this case, similar strain-induced segregation mechanisms are active as already discussed in chapter 5. The growth interruption (c) and the further overgrowth (d) have no significant influence on the shape of the type-1 quantum dots, since the thermal activation energy prevents diffusion within the already completely covered bulk material below 600°C.

The larger and more strained type-2 quantum dots are covered by a less GaAs material. During the following 600 s long growth interruption at elevated temperature (c) indium atoms from the highly strained indium-rich quantum dot center strongly segregate outwards. This leads to a wide but shallow depression and to the formation of a new wetting layer at the present growth surface. Such a second wetting layer formation was already predicted for the case of partially capped quantum dots, since according to the SK growth mode it is energetically favorable for InAs material to segregate from the quantum dot and to cover the GaAs surface [173–175]. After further overgrowth the shallow depression is filled with GaAs material and results in the observed kidney-shaped cross

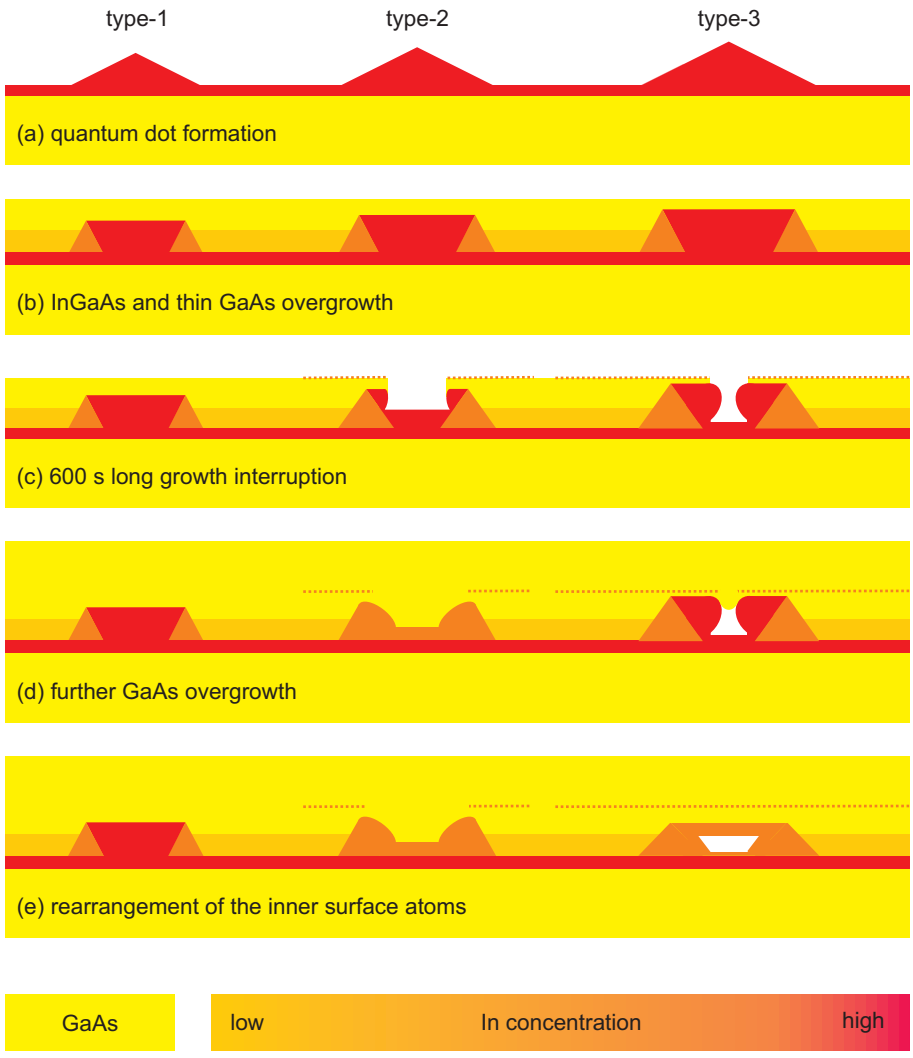

FIGURE 7.7: Schematic model of the development of three quantum-dot types; orange dotted lines denote out-diffused indium atoms [169].

sectional image (d). Such crater-like depressions in quantum dots were also observed in plane-view AFM images of InAs quantum dots covered by a thin GaAs cap layer [146]. Often such structures are called quantum rings and were further investigated also with XSTM [176], showing similar kidney-shaped images.

The largest type-3 quantum dots are capped by a very thin layer (b). Hence, the strain of the indium-rich center is so high, that during the 600 s long growth interruption the quantum dot material strongly segregates outward also from deeper regions (c). Again a second wetting layer is formed at the position where the growth was interrupted, as observed in the XSTM images shown in Fig. 7.5 (d, g). Additionally the observed density of the indium atoms in this second wetting layer is in good agreement with the amount of missing indium atoms in the nanovoids and type-2 quantum dots, corresponding to about 0.3 ML. If the crater aperture of the nanovoids is narrow enough (c) and the following overgrowth with GaAs sufficiently fast, the nanovoid is preserved since surface diffusion of the atoms occurs too slowly (d). After closing of the aperture the material hole remains and only a strain-induced rearrangement of the InAs material in the inner surface of the nanovoid may take place (e). The arsenic-rich growth conditions explain the arsenic termination of the nanovoid, as concluded from Fig. 7.5 (b).

The dissolution of partially capped quantum dots via the formation of such crater-like features has previously been predicted in a theoretical study by Wang et al. [175], who considered strain and surface energies, in agreement with the conclusions drawn here. Another theoretical description of this process was presented based on a liquid-droplet model, where outdiffusion is driven by surface tension [177], but neglecting strain effects.

In conclusion the presented growth model can nicely explain the three investigated quantum dot types as well as the associated formation of the second wetting layer. In order to grow larger and thus more strained quantum dots it has to be taken into account that due to kinetic effects nanovoids can form during overgrowth. This examination again confirms the strong influence of the capping process on the resulting quantum dot structure.

7.2 InAs quantum-dot-in-well sample

An even more distinctive influence of the capping process on the resulting quantum dot structure is found by investigating a quantum-dot-in-a-well (DWELL) nanostructure. The sample was grown using MBE by H. Y. Liu in the group of Prof. M. Hopkinson at the University of Sheffield, UK.

7.2.1 DWELL sample structure

The sample contains four DWELL structures, with two growth modes named DWELL 1 and 2, differing only in the thickness of the low temperature GaAs cap layer deposited prior to an extended growth interruption, as shown in Fig. 7.8. The DWELL sequence starts with 2 nm $In_{0.15}Ga_{0.85}As$ and 2.8 ML InAs quantum dot material, followed by a 10 s

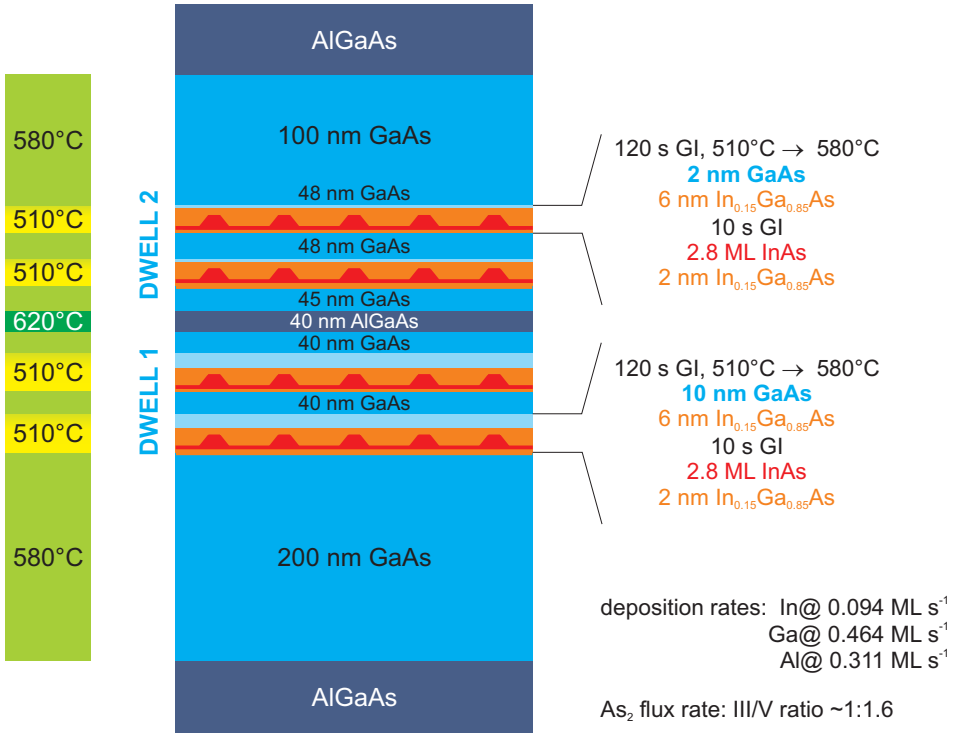

FIGURE 7.8: Investigated quantum-dot-in-a-well sample structure grown with MBE. DWELL 1 is capped with 10 nm and DWELL 2 with only 2 nm low temperature GaAs prior to an extended growth interruption.

growth interruption for quantum dot formation, and finally 6 nm $In_{0.15}Ga_{0.85}As$. After the DWELL growth at 510°C the nanostructures are capped, in the case of DWELL 1 with 10 nm GaAs followed by a 120 s long growth interruption and further GaAs cap growth at 580°C. In the case of DWELL 2 the GaAs cap layer thickness prior to the growth interruption is only 2 nm instead of 10 nm.

From optical investigations it was found that lasing at 100°C occurs at wavelengths of 1.29 μm and 1.35 μm for devices with 2 nm and 10 nm GaAs caps, respectively [50, 178]. This red-shift in wavelength indicates an increase in quantum dot size for thicker low-temperature GaAs cap layers. However, room temperature electroluminescence measurements showed a decrease of the intensity in the case of thicker GaAs cap layers and thus a decrease of the sample quality [50].

7.2.2 XSTM results on DWELL nanostructures

A typical XSTM image showing the DWELL nanostructure is presented in Fig. 7.9. The DWELL InGaAs region appears as a bright stripe indicated by the white dashed lines. The thickness of this DWELL region amounts to 6.5−8 nm, and the embedded quantum dots do not show clear contours. This result is similar to a recent investigation of DWELL quantum dots grown with MOVPE and containing only 1.8 ML InAs [179]. The quantum dot density observed here amounts to about 2.6−2.8 $\times$ 10^{10} cm^{-2} and is slightly larger for DWELL 1.

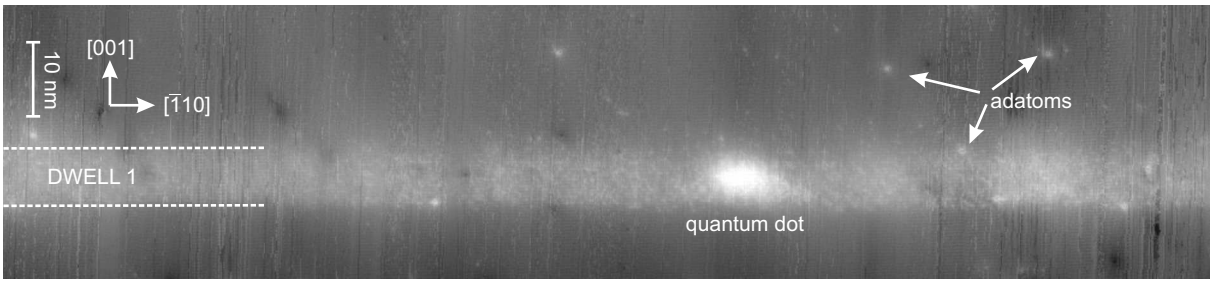

FIGURE 7.9: XSTM overview image of DWELL 1. The DWELL region is visible as a bright stripe and indicated by the white dashed lines. A quantum dot is embedded in the DWELL InGaAs layers, showing no clear contours.

In Fig. 7.10 XSTM images of a quantum dot from each DWELL structure are presented. The quantum dot shapes of both DWELL structures can be assumed as truncated pyramids, as indicated by the white dotted contour lines. The stoichiometry of the quantum dots in both DWELL types can be described by an indium-rich core close to the truncated quantum dot apex, indicated by the red dashed lines in Fig. 7.10. These observations are similar to those found for other In(Ga)As quantum dots [116, 117, 136], while they differ from a DWELL investigation by Ouattara et al. [179]. In the latter work, the quantum dot shape is determined as a broad oval with the highest amount of indium being found within the bottom half of the InGaAs region. This difference may be related to a 5 minute long growth interruption after only 3 nm GaAs cap growth on top of the DWELL structure. During this long growth interruption strong rearrangements can take place as will be discussed in section 7.2.3.

The size of quantum dots in DWELL 1 capped by 10 nm GaAs show typical baselengths of about 30 nm along [$\bar{1}$10] direction and heights of 6−9 nm along growth direction [Fig. 7.10 (a)]. Quantum dots in DWELL 2 capped by 2 nm GaAs prior to the growth interruption are generally smaller with baselengths of 20−25 nm and heights of 5−7 nm (b).

In addition to the regular quantum dots shown in Fig. 7.10 also structural defects

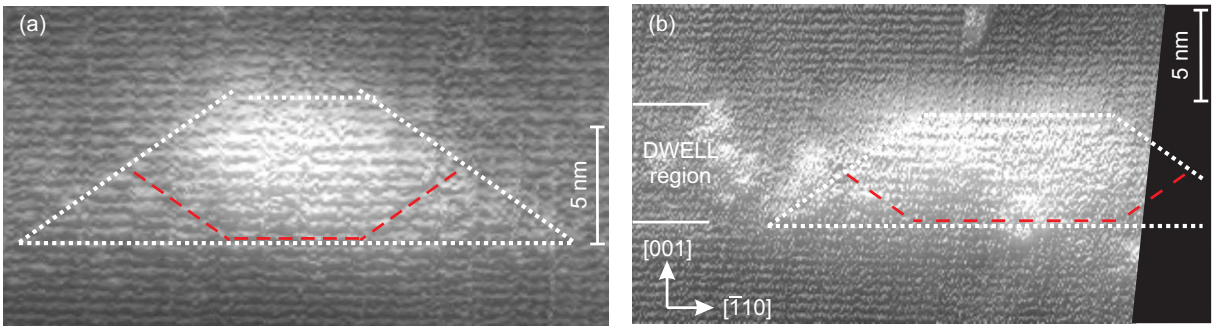

FIGURE 7.10: XSTM images of (a) a quantum dot in DWELL 1, taken at $V_S = 1.3$ V and $I_T = 65$ pA, and (b) a quantum dot in DWELL 2, taken at $V_S = -3.0$ V and $I_T = 50$ pA. Quantum dot shapes are indicated by the white dotted contour lines, while the red dashed lines indicate the indium-rich core [180].

or so-called nanovoids are observed, like those imaged in Fig. 7.11 (a−c) [180]. These nanovoids, indicated by cyan ellipses (a, b), are only rarely found in the case of the 2 nm thick GaAs cap prior to the growth interruption (a), while more than 30% of the quantum dots capped by 10 nm GaAs contain such structural defects (b, c).

The positions of the nanovoids are found both in the quantum dot center and at its edges, and their sizes amount to 5−20 nm laterally and to 1−5 nm along growth direction. In order to estimate the depth underneath the cleavage surface, height profiles across the nanovoids are analyzed. The height profile taken along the dashed line of Fig. 7.11 (c) is displayed in Fig. 7.11 (d), presenting the maximum depth observed for this nanovoid. It amounts to about 1.0 nm, which is much more than a 1 ML high cleavage step (0.2 nm), and indicates actually missing material. Additionally, no opposite structures are found like those observed in the nitride system [170, 171], which would be characteristic for cleavage defects e.g. caused by strain. In general, the nanovoids are similar to those observed in section 7.1.4.

XSTM data of the two DWELL layers show increased quantum dot sizes in the case of capping with thicker low temperature GaAs, which can explain the red-shift of the emission wavelength. Furthermore the predominant observation of nanovoids in this layer is in good agreement with the photoluminescence results, leading to an explanation of the decreasing sample quality.

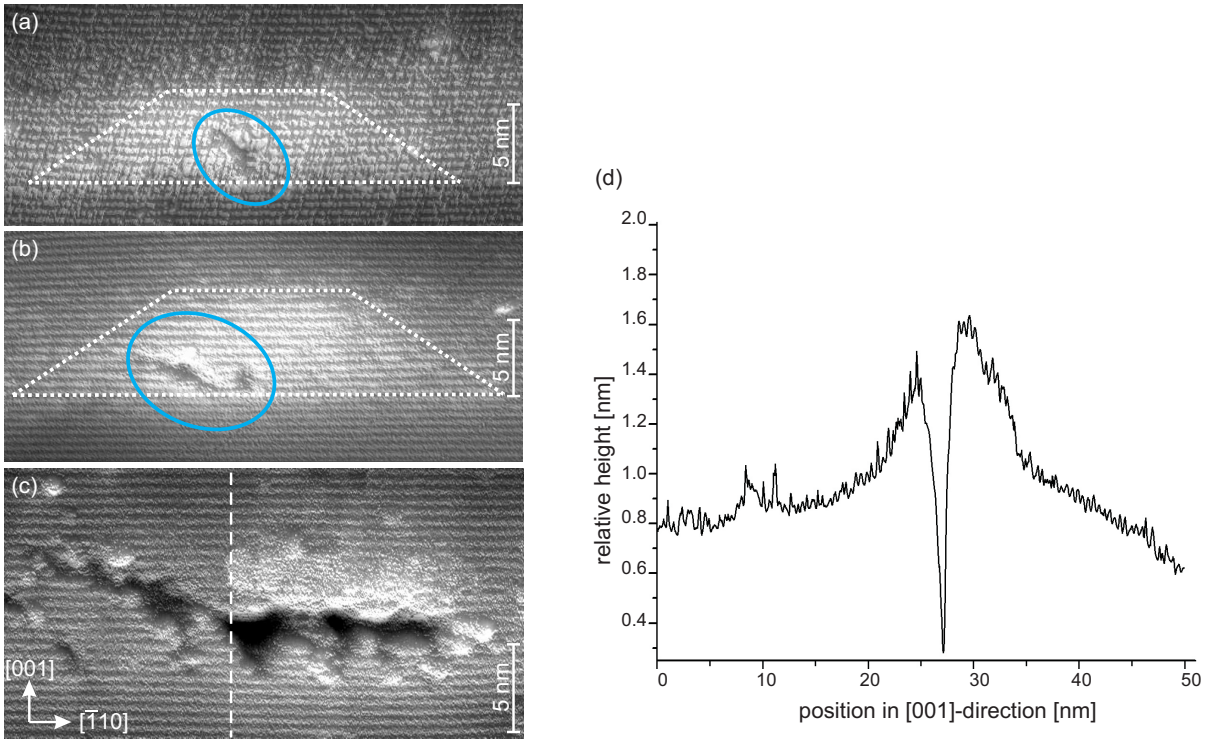

FIGURE 7.11: XSTM images of quantum dots containing nanovoids in (a) DWELL 1, taken at $V_S = -2.1$ V, (b) DWELL 2, taken at $V_S = -2.2$ V, and (c) DWELL 2, taken at $V_S = -2.9$ V with $I_T = 60$ pA for all images. Quantum dot shapes are indicated by the white dotted contour lines, while the cyan ellipses indicate the nanovoid position in (a, b). (d) Height profile across the quantum dot along the dashed line in (c).

7.2.3 Growth model for DWELL nanostructures

In order to understand the formation of the DWELL structures and in particular of the nanovoids a model for the quantum dot growth and the capping with InGaAs and GaAs is presented in Fig. 7.12. Growth of the DWELL structure starts with 2 nm $In_{0.15}Ga_{0.85}As$ deposition on the GaAs(001) substrate (a). The following InAs quantum dot growth on the InGaAs layer leads to a higher quantum dot density compared to an exclusive InAs deposition on GaAs [162, 164, 181], since the InGaAs layer reduces the surface energy.

After the strain-induced faceting of the growth surface by InAs deposition (b) [45], indium diffuses from the InGaAs layer and the wetting layer to the quantum dots [arrows in (c)], where elastic relaxation of indium-rich material in the quantum dot apex is minimizing the strain energy. Due to the high amount of InAs large quantum dot dome structures with steep side facets may form, as recently reported [29]. Here, indium migrates from the flanks to the quantum dot apex, leading to an indium depletion at the flanks (d).

During the following capping process by 6 nm $In_{0.15}Ga_{0.85}As$, a flattening of the quantum dot apex is expected (e), as observed also for the InAs/GaAs system [30] and already discussed in chapter 5. Additionally, from atomic force microscopy data taken during capping, the formation of trenches around the quantum dots due to InGaAs deposition is found, as shown in Fig. 7.13. This behavior can be attributed to limited surface-diffusion kinetics and the large strain energy which would have to be invested when filling the trenches.

For the quantum dots in DWELL 1 a total amount of 10 nm GaAs is deposited at low temperature (g). During the GaAs deposition the strain in the InGaAs layer increases considerably, so that many indium atoms segregate into the quantum dot center, while gallium tends to segregate out of the quantum dot, resulting in larger quantum dots. This process is indicated for indium by red and for gallium by cyan arrows in (g). In addition to the segregation process, some trenches are overgrown forming a cavity or so-called nanovoid (h), since growth kinetic is too slow to fill all trenches. During the following growth interruption the thicker GaAs cap layer preserve the nanovoid, and only a migration of the nanovoid towards the quantum dot center can take place, thereby reducing the local strain energy (i).

In the case of DWELL 2 only a thin GaAs cap is deposited prior to the 120 s long growth interruption, the latter allowing to fill the trenches by material rearrangement, additionally supported by the faster kinetics due to the increased temperature (j). Since most trenches are filled during the growth interruption or the subsequent overgrowth, predominantly regular quantum dots are observed in DWELL 2. During the growth interruption some indium from the InGaAs layer may segregate into the quantum dots [arrows in (j)], so that the indium content in the quantum dot center slightly increases. This leads to highly strained GaAs above the truncated quantum dot apex (k,l).

The presented growth and capping model can also explain the absence of nanovoids in the DWELL sample reported previously [179], since there only 1.8 ML InAs were

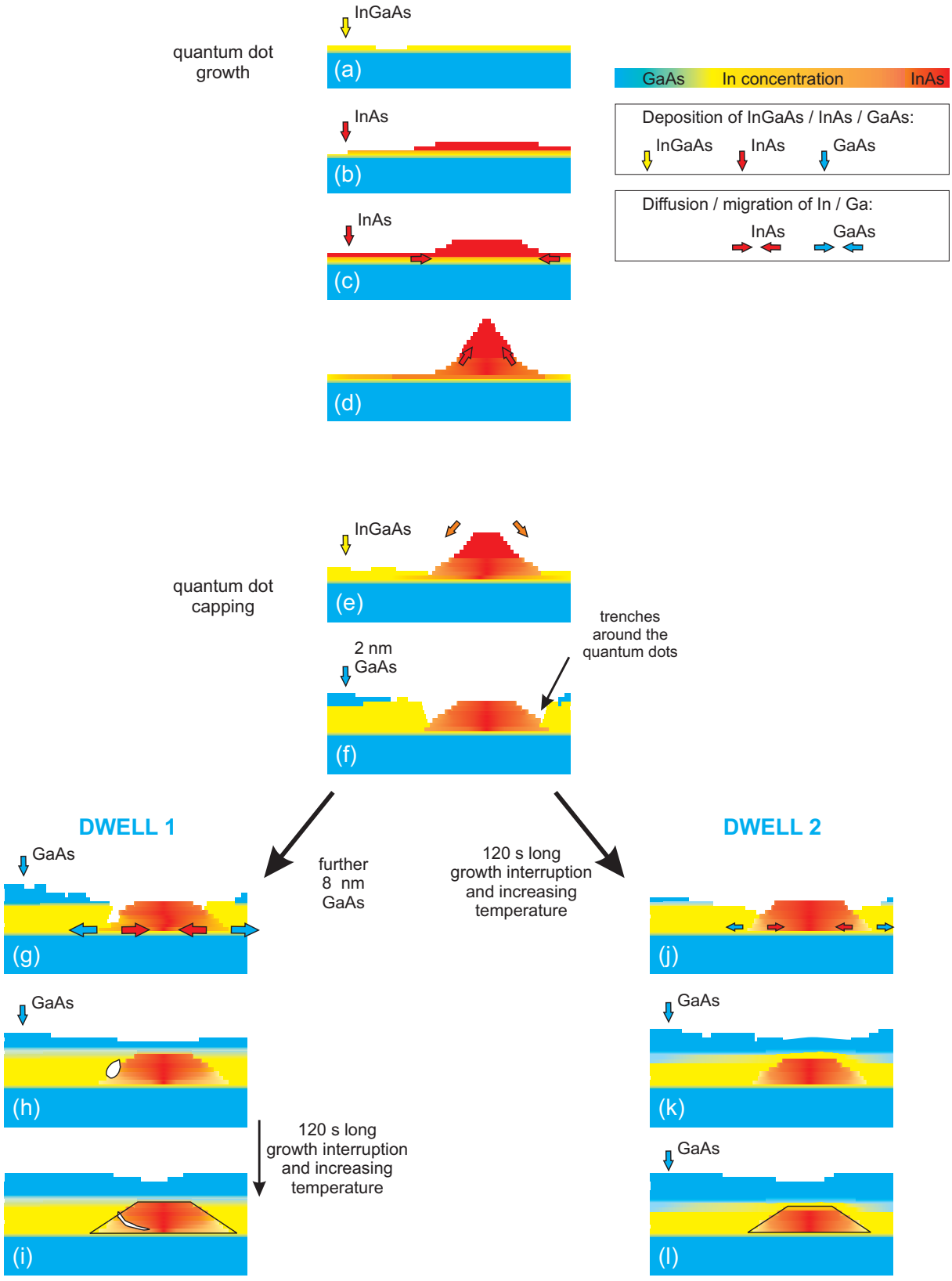

FIGURE 7.12: Model for quantum dot growth (a–d), the first capping steps (e, f), and the quantum dot evolution for DWELL 1 (g–i) leading to large quantum dots as well as to nanovoid formation, or for DWELL 2 (j–l) leading to predominantly regular quantum dots.

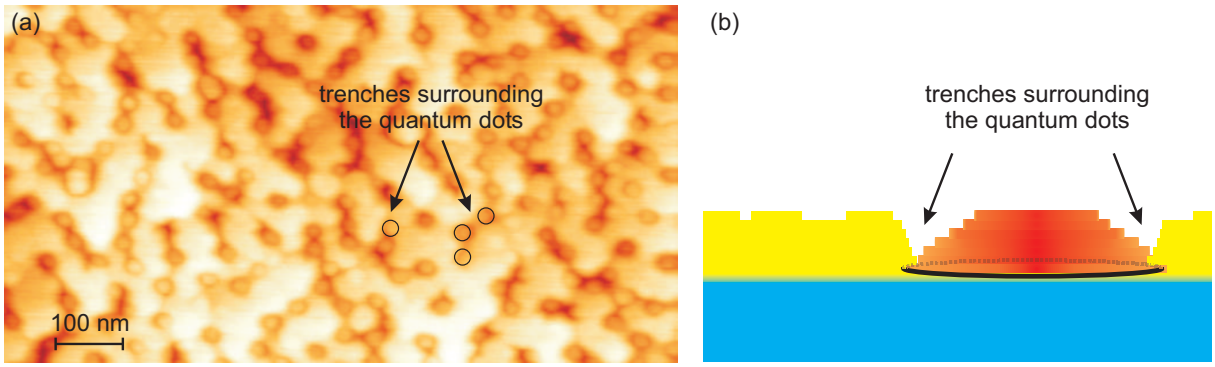

FIGURE 7.13: (a) AFM image taken after 6 nm InGaAs cap [182]. The InGaAs cap layer thickness is already higher than the quantum dots, which are visible as oval areas. Dark trenches around the quantum dots are indicated by the black circles. The sketch of (b) shows the position of the trenches in the growth model.

deposited. Thus the strain in the system during the capping was lower and a material rearrangement around possible trenches during the 5 minute long growth interruption after only 3 nm GaAs could easily take place, similar to the model for DWELL 2.

7.3 Discussion

Using InGaAs layers in combination with In(Ga)As quantum dots leads to an increase in the quantum dot size, and thus to the desired increase in the emission wavelength [50, 165, 178]. However, the additional observation of quantum dots containing nanovoids impressively shows the limit of larger quantum dot growth. The mechanisms leading to these nanovoids are primarily the strain in the system and the limited growth kinetics during capping.

Growth interruptions during capping are playing an important role for the resulting quantum dot structure. They allow material rearrangements and can lead to a dissolution of quantum dots [172], shape changes (section 7.1.3), and even to nanovoid formation (section 7.1.4). In another case, however, a specific growth interruption can avoid nanovoid formation due to material rearrangements filling formerly developed trenches (section 7.2.3). Due to the atomical resolved investigation on these defective quantum dots, the origin of the luminescence intensity decrease can be explained very well. Consequently the present investigations clearly show the importance of structural examinations of the capping process itself and of the final buried nanostructures.

Chapter 8

Unstrained GaAs/AlGaAs quantum dots

The last chapter of this thesis is focused on the investigation of GaAs/AlGaAs quantum dots, which are designed to emit light within the visible spectral range [31, 33]. One advantage of this system is an almost perfect match of the lattice constant, enabling the growth of unstrained quantum dots of a heterostructure which has been intensively studied [183, 184]. First XSTM results of these unstrained quantum dots will be presented, showing that in contrast to the predicted sharp interfaces a decomposition of the AlGaAs host layer and a roughening of the GaAs/AlGaAs interface are observed.

8.1 GaAs/AlGaAs quantum dot growth

The sample was grown using solid-source MBE by A. Rastelli et al. in the group of O. G. Schmidt at the Max-Planck-Institute of Solid State Physics in Stuttgart. The growth of the investigated unstrained GaAs quantum dots on a GaAs(001) substrate starts with a buffer layer followed by the deposition of 1.8 ML InAs quantum dot material, as shown in Fig. 8.1 (a). The SK grown InAs quantum dots are covered by 10 nm GaAs, followed by selective etching of nominally 5 nm strained material using $AsBr_3$ gas [185]. This technique leads to the formation of nanoholes at the position of the former InAs quantum dots, since the etching rate for InAs and for strained GaAs is higher than the one for unstrained GaAs (b). During the next preparation step, a layer of 7 nm $Al_{0.45}Ga_{0.55}As$ was deposited, which equally wets the underlying GaAs and the nanoholes, followed by 2 nm GaAs quantum dot material. A subsequent annealing step leads to a flattening of the GaAs surface. Finally, 10 nm $Al_{0.35}Ga_{0.65}As$ and a GaAs cap layer were grown. Therewith almost unstrained GaAs/AlGaAs quantum dots are formed in a hierarchical − i.e. multistep − procedure, which are located directly at positions above the previously self-organized InAs quantum dots, but are expected to have an inverted quantum dot shape, as shown schematically in Fig. 8.1 (c, d).

The InAs quantum dot growth and the etching process were controlled by AFM. The size and depth of the nanoholes may be tuned by changing the etching time. The density of the nanoholes is equal to the density of the previously grown InAs quantum dots [185].

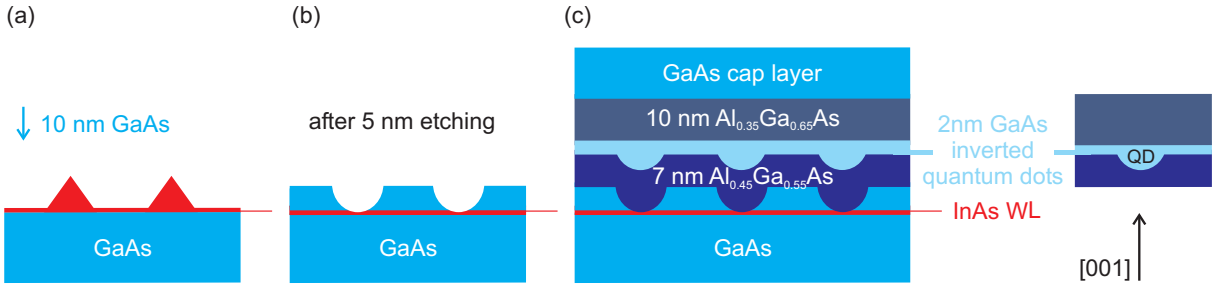

FIGURE 8.1: Fabrication of unstrained GaAs/AlGaAs quantum dots: (a) Growth of InAs quantum dots, followed by deposition of a 10 nm thick GaAs cap layer. (b) Etching of 5 nm strained material results in the formation of nanoholes at the positions of the former InAs quantum dots. (c) Deposition of AlGaAs and GaAs quantum dot material, annealing, and further capping by AlGaAs and GaAs results in a sample structure containing GaAs quantum dots.

Furthermore the etched nanoholes covered with the first $Al_{0.45}Ga_{0.55}As$ layer were also investigated by top-view STM, resulting in a deepness of the nanoholes of about 4 nm and an anisotropic shape. Their extensions of 65 nm along the [110] direction are about 35% larger than the observed extensions of about 40 nm along the $[1\bar{1}0]$ direction. In addition, it is known from low temperature PL data that the GaAs/AlGaAs quantum dots are optically active at 700−780 nm wavelength [31, 186].

8.2 XSTM results on GaAs/AlGaAs quantum dots

In contrast to the above mentioned structural investigations before GaAs quantum dot deposition, here images of the buried quantum dots are presented. Although the quality of the XSTM images of unstrained GaAs quantum dots should be further improved, they give a first important impression of the structure of the GaAs quantum dots. Both the positions of the unstrained quantum dots are determined and even size and shape can be estimated.

8.2.1 Decomposition of the AlGaAs host layer

Figure 8.2 shows a detailed XSTM image of the $Al_{0.45}Ga_{0.55}As/GaAs/Al_{0.35}Ga_{0.65}As$ quantum well structure beside the quantum dots. The bright line at the bottom of the image stems from the InAs wetting layer and is located directly at a surface step. The AlGaAs regions appear brighter than the GaAs regions and mostly do not show atomic resolution. Between the two AlGaAs regions, indicated by white arrows, the GaAs quantum well is visible. The observed thickness of the AlGaAs layers fits well to the nominal growth parameters, while the thickness of the GaAs quantum well varies between 0.5 and 2.5 nm. Furthermore a decomposition of the AlGaAs is determined, indicated in Fig. 8.2 by the solid contours marking GaAs areas in AlGaAs regions. In contrast, the dotted contours indicate AlGaAs areas in GaAs regions demonstrating that the interfaces between the GaAs and AlGaAs layers are not abrupt, in contrast to a simple model on layer growth

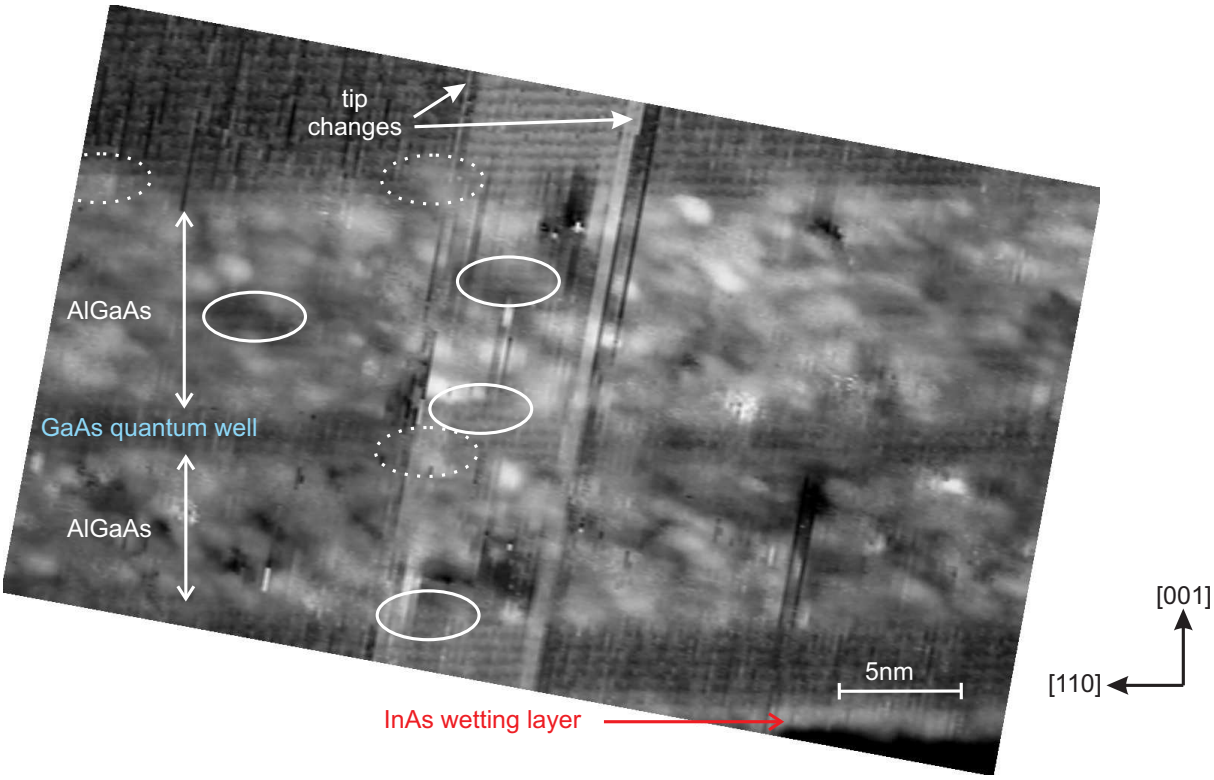

FIGURE 8.2: Atomically resolved GaAs quantum well structure. The AlGaAs regions are indicated by arrows, and the GaAs quantum well is located between the two AlGaAs regions. Solid contours indicate GaAs areas in AlGaAs and dotted contours AlGaAs areas in GaAs. The image was taken at $V_S = -2.5$ V and $I_T = 50$ pA [188].

of nearly unstrained material. Such an interface roughness was already mentioned in an early XSTM investigation by Salemink et al. [151] and further analyzed by Reusch et al. also using XSTM [187].

This observed AlGaAs decomposition may also explain another effect which was not yet understood: Recently, single dot photoluminescence excitation spectroscopy data for GaAs/AlGaAs quantum dots grown under similar conditions have been compared to eight-band $k \cdot p$ theory based calculations. For the computation sharp GaAs/AlGaAs quantum dot interfaces were assumed, and the possibility of a decomposition of the AlGaAs layer was not taken into account. It turned out that the spectroscopic value for the exciton groundstate is blue-shifted by 5.6 meV [31] compared to the calculated energy. The here observed decomposition may be one explanation for this blue-shift.

8.2.2 GaAs/AlGaAs quantum dots

In order to locate the unstrained GaAs/AlGaAs quantum dots, grown with a rather low density of 4×10^9 cm^{-2}, large areas have to be scanned. This process is time consuming and leads to a gradual surface contamination, since even under UHV conditions rest gas chemisorption especially on the aluminium-containing compound takes place. This results in unstable tunneling conditions and in a rough and unstructured appearance of

the AlGaAs layers [151], as already shown in Fig. 8.2. Thus, the obtained XSTM images are less resolved and interpretation is more difficult than in the preceding chapters.

In order to locate GaAs quantum dots, the XSTM images have to be examined for regions were the lower AlGaAs layer reaches down to the InAs wetting layer. At this position the etching technique has formed a nanohole, in which the AlGaAs matrix and GaAs quantum dot material was deposited (Fig. 8.1).

In Fig. 8.3 (a) the InAs wetting layer is indicated as a transparent red line, located at a surface step. The former GaAs quantum dot cap layer as well as the GaAs wetting

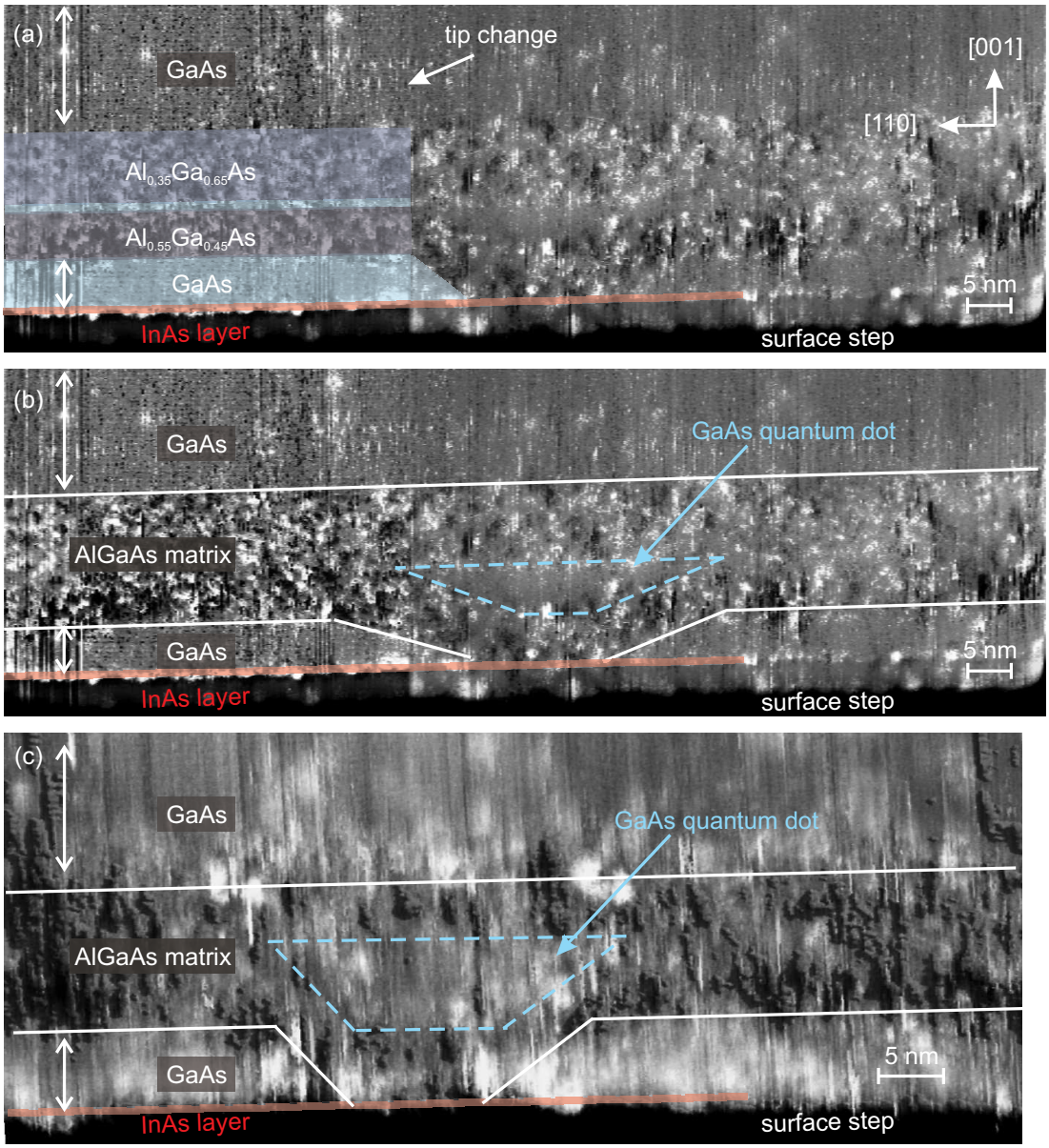

FIGURE 8.3: Filtered XSTM images of two different GaAs quantum dots, taken at $I_T = 60$ pA [188]. Colored stripes and white lines indicate the different materials and their interfaces. (a, b) GaAs quantum dot taken at $V_S = -2.0$ V. (c) Image of a different quantum dot, taken at $V_S = +2.3$ V and relief filtered in order to pronounce the AlGaAs matrix and the embedded quantum dot.

layer are indicated by transparent cyan stripes, and the AlGaAs quantum dot matrix layers by transparent dark blue stripes. At the right side of the colored stripes a tip change and a corresponding change in the image contrast is visible. Figure 8.3 (b) shows the same image, but the interfaces of the AlGaAs quantum dot matrix material and the GaAs regions are separated by white lines. It can clearly be seen that the lower AlGaAs interface reaches down to the InAs wetting layer, and exactly above this position the GaAs/AlGaAs quantum dot is located. The GaAs quantum dot material has a smooth appearance like the other GaAs regions of this sample, in contrast to the surrounding rough AlGaAs matrix. Hence the derived contour of this quantum dot is indicated by the dashed cyan line.

The width of the GaAs quantum dot increases in growth direction, as also expected from the growth procedure. Consequently the shape can be described by a reversed truncated pyramid or a reversed truncated cone. The estimated quantum dot height amounts to about 5 nm and the lateral extension along [110] direction is about 35 nm. No surface curvature at the quantum dot is observed, confirming the absence of strain in the present case. This is in contrast to the InAs/GaAs system, where quantum dots are highly strained and form bright protruding objects in XSTM images.

Another GaAs quantum dot is shown in Fig. 8.3 (c), taken at positive sample bias, where mainly the aluminium and gallium atoms are imaged. Here the AlGaAs matrix appears darker than the surrounding GaAs material, indicating that anionic contamination such as oxygen adatoms are present on the AlGaAs surface. In the lower part of the image the InAs wetting layer is again located at a surface step, and the AlGaAs matrix material reaches down to the InAs wetting layer, indicating the position of the GaAs quantum dot. The quantum dot region has the same smooth appearance as the GaAs on top of the AlGaAs matrix and the shape can once more be characterized by a reversed truncated cone with a lateral extension of about 35 nm, and a height of about 6 nm. Unfortunately the resolution of these images is limited due to the problems mentioned above, so that no further details can be derived.

8.3 Discussion

The investigation of hierarchically self-assembled GaAs/AlGaAs quantum dots leads to a first impression of unstrained GaAs quantum dots in XSTM images. The developed strategy to localize the unstrained and thus inconspicuous GaAs quantum dots via the corrugated AlGaAs layer underneath is a very useful preliminary work for further analysis. It will help to take images briefly after sample cleavage and thus with a less contaminated sample surface and better tip conditions.

In spite of the initial difficulties first structural results on GaAs/AlGaAs quantum dots are derived. The GaAs quantum dot centers appear to be rather pure GaAs, but the GaAs/AlGaAs interfaces are found to be intermixed. Furthermore, the estimated quantum dot height of 5−6 nm is in agreement with the top-view STM investigation of

the former nanoholes, while the lateral size of 35 nm along [110] direction is only about half the size of the nanoholes observed before quantum dot material deposition [31]. This observed smaller lateral size can be related to the unknown cleave position through the quantum dots.

Additionally, from atomically resolved images a thickness variation of the GaAs quantum well between 0.5 nm and 2.5 nm and a decomposition of the AlGaAs layers is observed. This interface roughness may be one explanation for an blue-shift of the exciton ground-state observed in a comparison between spectroscopy data and a theoretical calculation without intermixing effect [31]. Furthermore, such an intermixing is in agreement with recently published results on the electronic structure of GaAs/AlGaAs quantum dots investigated under an external magnetic field and compared with a theoretical investigation varying the degree of interface intermixing [189]. This underlines once more the importance of a structural investigation of the buried nanostructures considerably improving the understanding of the growth process.

Chapter 9

Conclusion

In the present thesis different In(Ga)As/GaAs and GaAs/AlGaAs quantum dot structures was investigated with XSTM. The growth and examination of these samples were designed to derive an enhanced knowledge on the spatial structure of the buried quantum dots as well as on their optical properties. In particular, a detailed study of the influence of the overgrowth process on the resulting nanostructure is necessary, since in the last years an intensive discussion on this topic has taken place. Furthermore, structural parameters are always the basis for theoretical calculations, and a comparison with other physical properties can lead to a better understanding of these fascinating nanostructures.

In the first part it was examined how InAs/GaAs quantum dot structures change during the overgrowth process. For this purpose atomically resolved STM images of InAs quantum dots obtained prior to capping by the group of Jacobi et al. [49, 113, 120] were compared with XSTM results of buried structures investigated in this study. For the first time such an investigation was performed at samples grown in the same MBE chamber and under identical growth conditions. Consequently changes in size, shape, and stoichiometry of the quantum dots could directly be attributed to the overgrowth process.

In the top-view STM study pyramidal InAs/GaAs quantum dots with rather flat {137} side facets were observed [49, 113]. Such high-index facets were formerly not expected, but subsequent investigations on uncapped quantum dots confirmed these structural findings. Also recently published top-view STM results of InAs quantum dots with increased sizes always show pyramidal shapes with {137} side facets [114]. In the present XSTM study it was observed that the quantum dot shape after overgrowth is characterized by a flat (001) top facet and steeper {101} or {111} side facets. In addition, also quantum dots with an increased material amount always show a truncated pyramidal shape with a flat (001) top facet. Furthermore from the stoichiometry determination a strong intermixing of both quantum dots and wetting layer was found, and for larger quantum dots even an indium distribution forming a reversed cone was derived. On the other hand for quantum dots grown under a reduced growth temperature, a strong size reduction of the quantum dots was found supported by missing quantum dot luminescence in photoluminescence measurements.

Based on these findings, a model for the overgrowth of free-standing quantum dots was

presented: The atoms of the initial GaAs capping layer cannot be incorporated directly at the top of the pyramidal quantum dot due to the large lattice mismatch, but drag some indium atoms from the apex towards the quantum dot edges. This segregation of indium atoms from the apex to the sides leads to intermixing and thus reduces this lattice mismatch at the apex, and furthermore steeper side facets are formed. The intermixing of the wetting layer can be attributed to strain energy reduction. Further GaAs overgrowth leads to a capping of the quantum dots starting from their sides, and finally a truncated pyramidal quantum dot structure remains.

Further XSTM investigations were performed with different quantum dot samples designed to obtain increased emission wavelengths. Firstly, InAs quantum dots grown under antimony supply during different growth stages were studied. From the XSTM data it could be concluded, that the red-shift in the wavelength is caused by an increase of the quantum dot volume and the averaged indium content. Antimony is known to decrease the surface energy [53, 150], allowing an earlier onset of quantum dot formation [98], larger quantum dot sizes, and strongly reduced indium-gallium intermixing. Additionally antimony is only incorporated into the wetting layer, while the quantum dots remain antimony free.

Secondly, MOCVD grown InGaAs quantum dots covered with a strain-reducing diluted InGaAs capping layer were examined. Three different quantum dot types were found, depending on the size of the uncapped quantum dots. The smallest quantum dots again showed a structural change towards a truncated pyramid, and a rearrangement of the indium distribution towards a reversed cone during the initial capping process was found. For the larger quantum dot types additional and even more drastic changes were observed. During an extended growth interruption after partial capping, strong segregation effects lead to an outdiffusion of single indium atoms from the highly strained indium-rich quantum dot center. These indium atoms form a new wetting layer, as observed in the XSTM images, and the remaining quantum dots develop either towards a truncated pyramid with a shallow depression or − in the case of the largest and thus most strained quantum dots − towards a material hole or so-called nanovoid. Such a dissolution of partially capped quantum dots and the formation of a new wetting layer is in nice agreement with theoretical results [175].

Thirdly, MBE-grown InAs quantum dot structures embedded within InGaAs quantum well layers (DWELL) were analyzed. The two investigated DWELL structures only vary in the thickness of the GaAs cap layer prior to an extended growth interruption under an increased temperature. XSTM data showed that for the thicker capping layer the quantum dots were increased in size. In addition, also nanovoids were found in this DWELL structure. However the formation process of the nanovoids observed here differs from those observed in the above discussed InGaAs sample. During the overgrowth with the InGaAs quantum well, the large and highly strained InAs quantum dots still remain uncapped, since overgrowth takes place firstly at the wetting layer and finally at the quantum dots, as already discussed above. Thus during overgrowth with InGaAs trenches

form around the quantum dots, as also observed with AFM [182]. In the case of a thin GaAs cap layer deposited prior to the growth interruption, these trenches are filled by a material rearrangement, additionally supported by the faster kinetics due to the increased temperature. In the case of the thicker GaAs cap layer, in contrast, the strain in the system increases considerably, so that strong segregation processes and limited growth kinetics lead to the overgrowth of some trenches, remaining as nanovoids. These findings are in agreement with luminescence data showing a red-shift of the emission wavelength in the case of the increased GaAs capping layer, accompanied by a decreasing intensity.

It should be noted here that the XSTM observation of capped quantum dots containing nanovoids impressively show the limitations in the growth of larger and thus more strained quantum dots.

Finally hierarchically grown unstrained GaAs/AlGaAs quantum dots were investigated. The growth of these quantum dots was based on self-organized InAs quantum dots capped with a thin GaAs layer. Afterwards the strained InAs and GaAs material was removed by selective etching and the developed nanohole was filled subsequently with a thin AlGaAs layer and the GaAs quantum dot material. Hence, the growth of the GaAs/AlGaAs quantum dots depends on the structure of the capped InAs quantum dots, since only the strained material was removed. Thus structural and stoichiometric changes of the InAs quantum dots during capping may affect also the appearance of the nanohole, forming the base of the following GaAs quantum dot material deposition. XSTM images of GaAs/AlGaAs quantum dots confirmed the expected quantum dot heights and showed pure GaAs quantum dot centers. In addition a decomposition of the AlGaAs layers was observed as well as a variation in the GaAs wetting layer thickness, which was not taken into account in theoretical calculations so far. Thus these initial results already underline the importance of further investigations on buried GaAs/AlGaAs quantum dot structures.

These entire investigations demonstrate the uniqueness of the XSTM method for the structural study of buried quantum dots with atomic resolution. The comparison of uncapped and capped quantum dots allows to examine the processes occurring during growth and overgrowth of these fascinating nanostructures. Systematic variations of the sample preparation parameters lead to an enhanced understanding of the influences introduced by certain growth steps. Thus further XSTM experiments will be very promising to improve the insight on the formation processes of buried nanostructures.

List of abbreviation

AFM	atomic force microscopy
DWELL	(quantum)-dot-in-a-well
GI	growth interruption
MBE	molecular beam epitaxy
ML	monolayer
MOCVD	metal-organic chemical vapor deposition
MOVPE	metal-organic chemical vapor phase epitaxy
PL	photoluminescence
PLE	photoluminescence excitation
RHEED	reflection high-energy electron diffraction
SK	Stranski-Krastanow
STM	scanning tunneling microscopy
TEM	transmission electron microscopy
VPE	vapor phase epitaxy
XSTM	cross-sectional scanning tunneling microscopy
UHV	ultrahigh vacuum

Danksagung

An dieser Stelle möchte ich mich bei all denjenigen bedanken, die mir diese Arbeit ermöglicht haben und ohne deren Unterstützung diese Zeit nicht so schön gewesen wäre.

Als Erstes danke ich Prof. Mario Dähne, der mir die Anfertigung dieser Arbeit ermöglicht hat. Seine Begeisterung über neue Messergebnisse und die vielen hilfreichen Diskussionen über die erhaltenden Daten sowie seine Ausdauer beim Korrekturlesen diverser Arbeiten ist einzigartig. Ich danke Prof. Dieter Bimberg für die Anfertigung des Zweitgutachtens, der Bereitstellung einiger hier untersuchter Proben sowie der zeitweiligen finanziellen Unterstützung. Außerdem gilt mein Dank Prof. Erwin Sedlmayr für die Übernahme des Prüfungsvorsitzes.

Für die Herstellung der Proben danke ich Dr. Roman Sellin und Konstantin Pötschke aus der Arbeitsgruppe von Prof. Dieter Bimberg, Dr. Takayuki Suzuki und Dr. Yevgeniy Temko aus der Gruppe von Prof. Karl Jacobi und Dr. Armando Rastelli aus der Arbeitsgruppe von Prof. Oliver Schmidt. Ich danke Priv.-Doz. Dr. Udo Pohl für die vielfältigen und äußerst hilfreichen Diskussionen zum Quantenpunktwachstum. Further, I thank Dr. Huiyun Liu and Prof. Mark Hopkinson for the DWELL sample growth and the fruitful discussions.

Herzlichen Dank an Dr. Holger Eisele für seine geduldige Einführung in den Umgang mit dem Rastertunnelmikroskop, das Auffinden von Quantenpunkten sowie dafür, dass er mich motiviert hat, die Promotion zu beginnen. Ich danke ihm für seine tatkräftige Hilfe bei der Interpretation der Messdaten, bei allen notwendigen Reparaturen und für viele nette Abende beim Messen und auf Konferenzen.

Desweitern möchte ich mich bei allen ehemaligen und aktuellen Arbeitsgruppenmitgliedern recht herzlich für ihre Unterstützung und die tolle Atmosphäre in den vergangenen Jahren bedanken: Angela Berner und Gerd Pruskil für die gemeinsamen Kämpfe gegen Viren, Würmer und Trojaner, und Jan Grabowski, Kai Hodeck, Lena Ivanova und Martina Wanke für ein immer offenes Ohr und praktische Hilfe bei physikalischen Problemen sowie für eine insgesamt schöne Zeit. Ich danke Tai-Yang Kim, Matthias Müller, Dominik Martin, Vivien Voßebürger und allen weiteren Mitstreitern, die hier nicht mehr namentlich genannt sind, für die gemeinsamen XSTM Messungen: *DANKE!*

Ein besonderer Dank gilt Sebastian Becker und Rainer Timm für die schöne gemeinsame Zeit in der Arbeitsgruppe und die Freundschaft, die darüber hinaus entstanden ist. Außerdem gilt mein Dank meiner gesamten Familie, für ihre Unterstützung bei allem was ich bisher getan habe. Der größte Dank aber gebührt meinem Ehemann Ernst für sein Verständnis für die vielen arbeitsreichen Tage und dafür, dass er immer für mich da ist.

Bibliography

[1] D. Bimberg, M. Grundmann, and N. N. Ledentsov, *Quantum Dot Heterostructures*, John Wiley & Sons Ltd., Chichester, 1999, ISBN: 978-0-471-97388-1.

[2] M. Grundmann (Ed.), *Nano-Optoelectronics: Concepts, Physics and Devices*, NanoScience and Technology, Springer, Berlin, 2002, ISBN: 978-3-540-43394-1.

[3] A. Einstein, Physikalische Zeitschrift **18**, 121 (1917).

[4] J. P. Gordon, H. J. Zeiger, and C. H. Townes, Phys. Rev. **95**, 282 (1954).

[5] T.-H. Maiman, Nature **187**, 493 (1960).

[6] R. N. Hall et al., Phys. Rev. Lett. **9**, 366 (1962).

[7] M. I. Nathan et al., Appl. Phys. Lett. **1**, 62 (1962).

[8] N. Holonyak et a., Appl. Phys. Lett. **1**, 82 (1962).

[9] L. Goldstein, F. Glas, J. Y. Marzin, M. N. Charasse, and G. LeRoux, Appl. Phys. Lett. **47**, 1099 (1985).

[10] Photographer: Klaas Ole Krtz 2003-06-27 (Wikimedia user: Drbashir117), image taken from http://en.wikipedia.org/wiki/Image:KielerFoerdeUndHDWKraene.jpg, visited November 2007.

[11] Image of my parents sail boat.

[12] V. N. Lutskii, phys. stat. sol. (a) **1**, 199 (1970).

[13] Y. Arakawa and H. Sakaki, Appl. Phys. Lett. **40**, 939 (1982).

[14] M. Asada, Y. Miyamoto, and Y. Suematsu, IEEE J. Quantum Elec. **QE-22**, 1915 (1986).

[15] N. Kirstaedter, N. N. Ledentsov, M. Grundmann, D. Bimberg, V. M. Ustinov, S. S. Ruvimov, M. V. Maximov, P. S. Kop'ev, Zh. I. Alferov, U. Richter, P. Werner, U. Gösele, and J. Heydenreich, IEEE Electron. Lett. **30**, 1416 (1994).

[16] U. Woggon, *Optical Properties of Semiconductor Quantum Dots*, Vol. 136 of *Springer Tracts in Modern Physics*, Springer-Verlag, Berlin, 1997, ISBN: 3-540-60906-7.

[17] V. A. Shchukin and D. Bimberg, Rev. Mod. Phys. **71**, 1125 (1999).

[18] A. Zrenner, J. Chem. Phys. **112**, 7790 (2000).

[19] T. J. Bukowski and J. H. Simmons, Crit. Rev. Sol. Stat. Mat. Sci. **27**, 119 (2002).

[20] V. Shchukin, N. N. Ledentsov, and D. Bimberg, *Epitaxy of Nanostructures*, Springer, Berlin, 2003, ISBN: 3-540-67817-4.

[21] N. Anscombe, Nature Photonics **1**, 360 (2007).

[22] A. Schliwa, M. Winkelnkemper, and D. Bimberg, Phys. Rev. B **76**, 205324 (2007).

[23] O. Stier, M. Grundmann, and D. Bimberg, Phys. Rev. B **59**, 5688 (1999).

[24] P. W. Fry, I. E. Itskevich, D. J. Mowbray, M. S. Skolnick, J. J. Finley, J. A. Barker, E. P. O'Reilly, L. R. Wilson, I. A. Larkin, P. A. Maksym, M. Hopkinson, M. Al-Khafaji, J. P. R. David, A. G. Cullis, G. Hill, and J. C. Clark, Phys. Rev. Lett. **84**, 733 (2000).

[25] J. Shumway, A. J. Williamson, A. Zunger, A. Passaseo, M. DeGiorgi, R. Cingolani, M. Catalano, and P. Crozier, Phys. Rev. B **64**, 125302 (2001).

[26] Q. Xie, A. Madhukar, P. Chen, and N. P. Kobayashi, Phys. Rev. Lett. **75**, 2542 (1995).

[27] G. D. Lian, J. Yuan, L. M. Brown, G. H. Kim, and D. A. Ritchie, Appl. Phys. Lett. **73**, 49 (1998).

[28] P. B. Joyce, T. J. Krzyzewski, G. R. Bell, and T. S. Jones, Appl. Phys. Lett. **79**, 3615 (2001).

[29] P. Kratzer, Q. K. K. Liu, P. Acosta-Diaz, C. Manzano, G. Costantini, R. Songmuang, A. Rastelli, O. G. Schmidt, and K. Kern, Phys. Rev. B **73**, 205347 (2006).

[30] G. Costantini, A. Rastelli, C. Manzano, P. Acosta-Diaz, R. Songmuang, G. Katsaros, O. G. Schmidt, and K. Kern, Phys. Rev. Lett. **96**, 226106 (2006).

[31] A. Rastelli, S. Stufler, A. Schliwa, R. Songmuang, C. Manzano, G. Costantini, K. Kern, A. Zrenner, D. Bimberg, and O. G. Schmidt, Phys. Rev. Lett. **92**, 166104 (2004).

[32] S. Watanabe, E. Pelucchi, B. Dwir, M. H. Baier, K. Leifer, and E. Kapon, Appl. Phys. Lett. **84**, 2907 (2004).

[33] M. Benyoucef, A. Rastelli, O. G. Schmidt, S. M. Ulrich, and P. Michler, Nanoscale Res. Lett. **1**, 172 (2006).

[34] Y. Miyamoto, M. Cao, Y. Shingai, K. Furuja, Y. Suematsu, K. G. Ravikumar, and S. Arai, Jpn. J. Appl. Phys. **26**, L225 (1987).

[35] S. R. Andrews, H. Arnot, P. K. Rees, T. M. Kerr, and S. P. Beaumont, J. Appl. Phys. **67**, 3472 (1990).

[36] R. Steffen, F. Faller, and A. Forchel, J. Vac. Sci. Technol. B **12**, 3653 (1994).

[37] K. Eberl, P. M. Petroff, and P. Demeester (Eds.), *Low Dimensional Structures Prepared by Epitaxial Growth or Regrowth on Patterned Substrates*, Vol. 298 of *NATO Science Series E*, Springer Netherland, 1995, ISBN: 978-0-7923-3679-2.

[38] N. N. Ledentsov, *Growth Process and Surface Phase Equilibria in Molecular Beam Epitaxy*, Vol. 156 of *Springer Tracts in Modern Physics*, Springer, Berlin, 1999, ISBN: 978-3-540-65794-1.

[39] M. A. Herman, W. Richter, and H. Sitter, *Epitaxy. Physical Principles and Technical Implementation*, Vol. 62 of *Springer Series in Materials Science*, Springer, Berlin, 2004, ISBN: 3-540-67821-2.

[40] E. Pehlke, N. Moll, A. Kley, and M. Scheffler, Appl. Phys. A **65**, 525 (1997).

[41] F. C. Frank and J. H. van der Merwe, Proc. Roy. Soc. **198**, 205 (1949).

[42] M. Volmer and A. Weber, Zeit. phys. Chem. **119**, 227 (1926).

[43] I. N. Stranski and L. Krastanow, Monatshefte für Chemie / Chemical Monthly **71**, 351 (1937).

[44] I. N. Stranski and L. Krastanov, Sitzungsbericht Wiener Akademie der Wissenschaften, Klasse IIb **146**, 787 (1938).

[45] V. A. Shchukin, N. N. Ledentsov, M. Grundmann, P. S. Kop'ev, and D. Bimberg, Surf. Sci. **352**, 117 (1996).

[46] N. Moll, M. Scheffler, and E. Pehlke, Phys. Rev. B **58**, 4566 (1998).

[47] R. Heitz, T. R. Ramachandran, A. Kalburge, Q. Xie, I. Mukhametzhanov, P. Chen, and A. Madhukar, Phys. Rev. Lett. **78**, 4071 (1997).

[48] L. Däweritz and R. Hey, Surf. Sci. **236**, 15 (1990).

[49] J. M. Màrquez Bertoni, *Struktur von GaAs-Oberflächen und ihre Bedeutung für InAs-Quantenpunkte*, PhD thesis, TU Berlin, 2000.

[50] H. Y. Liu, S. L. Liew, T. J. Badcock, D. J. Mowbray, M. S. Skolnick, S. K. Ray, T. L. Choi, K. M. Groom, B. Stevens, F. Hasbullah, C. Y. Jin, M. Hopkinson, and R. A. Hogg, Appl. Phys. Lett. **89**, 073113 (2006).

[51] W. Richter, Appl. Phys. A **75**, 129 (2002).

[52] R. L. Sellin, Ch. Ribbat, M. Grundmann, N. N. Ledentsov, and D. Bimberg, Appl. Phys. Lett. **78**, 1207 (2001).

[53] K. Pötschke, L. Müller-Kirsch, R. Heitz, R. L. Sellin, U. W. Pohl, D. Bimberg, N. Zakharov, and P. Werner, Physica E **21**, 606 (2004).

[54] D. L. Huffaker, G. Park, Z. Zou, O. B. Shchekin, and D. G. Deppe, Appl. Phys. Lett. **73**, 2564 (1998).

[55] D. Bimberg, M. Grundmann, N. N. Ledentsov, M. H. Mao, Ch. Ribbat, R. Sellin, V. M. Ustinov, A. E. Zhukov, Zh. I. Alferov, and J. A. Lott, phys. stat. sol. (b) **224**, 787 (2001).

[56] J. M. García, T. Mankad, P. O. Holtz, P. J. Wellman, and P. M. Petroff, Appl. Phys. Lett. **72**, 3172 (1998).

[57] L. Reimer, *Transmission Electron Microscopy*, Vol. 36 of *Springer Series in Optical Sciences*, Springer, Berlin, 1984, ISBN: 3-540-11794-6.

[58] P. Werner, K. Scheerschmidt, N. D. Zakharov, R. Hillebrand, M. Grundmann, and R. Schneider, Cryst. Res. Technol. **35**, 759 (2000).

[59] C. J. Chen, *Introduction to Scanning Tunneling Microscopy*, Oxford Series in Optical and Imaging Sciences, Oxford University Press, 1993, ISBN: 0-19-507150-6.

[60] R. Wiesendanger (Ed.), *Scanning Probe Microscopy and Spectroscopy. Analytical Methods*, NanoScience and Technology, Springer, Berlin, 1998, ISBN: 978-3-540-43394-1.

[61] G. Binnig, H. Rohrer, Ch. Gerber, and E. Weibel, Appl. Phys. Lett. **40**, 178 (1981).

[62] G. Binnig, H. Rohrer, Ch. Gerber, and E. Weibel, Phys. Rev. Lett. **49**, 57 (1982).

[63] Chunli Bai, *Scanning Tunneling Microscopy and its Application*, Vol. 32 of *Springer Series in Surface Sciences*, Springer, Shanghei Scientific & Technical Publishers, 1995, ISBN: 3-540-59346-2.

[64] R. Wiesendanger and H.-J. Güntherodt (Eds.), *Scanning Tunneling Microscopy I-III*, Springer Series in Surface Sciences, Ed. 2, Springer-Verlag, Berlin, 1996, ISBN: 3-540-58415-3.

[65] S. Grafström, Appl. Phys. Rev. **91**, 1717 (2002).

[66] P. Muralt, Appl. Phys. Lett. **49**, 1441 (1986).

[67] R. M. Feenstra, J. A. Stroscio, J. Tersoff, and A. P. Fein, Phys. Rev. Lett. **58**, 1192 (1987).

[68] A. R. Smith, S. Gwo, and C. K. Shih, Rev. Sci. Instrum. **65**, 3216 (1994).

[69] R. M. Feenstra, Semicond. Sci. Technol. **9**, 2157 (1994).

[70] A. Y. Lew, E. T. Yu, D. H. Chow, and R. H. Miles, Appl. Phys. Lett. **65**, 201 (1994).

[71] A. R. Smith, K.-J. Chao, C. K. Shih, Y. C. Shih, and B. G. Streetman, Appl. Phys. Lett. **66**, 478 (1995).

[72] T. Takahashi, M. Yoshita, and H. Sakaki, Appl. Phys. Lett. **68**, 502 (1996).

[73] W. Wu, J. R. Tucker, G. S. Solomon, and J. S. Harris, Appl. Phys. Lett. **71**, 1083 (1997).

[74] B. Legrand, B. Grandidier, J. P. Nys, D. Stiévenard, J. M Gérard, and V. Thierry-Mieg, Appl. Phys. Lett. **73**, 96 (1998).

[75] K.-J. Chao, N. Liu, C.-K. Shih, D. W. Gotthold, and B. G. Steetman, Appl. Phys. Lett. **75**, 1703 (1999).

[76] H. Eisele, O. Flebbe, T. Kalka, C. Preinesberger, F. Heinrichsdorff, A. Krost, D. Bimberg, and M. Dähne-Prietsch, Appl. Phys. Lett. **75**, 106 (1999).

[77] S. Blügel, *Theorie der Rastertunnelmikroskopie*, Lecture Notes, Research Centre Jülich, http://www.fz-juelich.de/iff/staff/Bluegel_S/Lectures/S_Bluegel_lec.html, visited on August 2007.

[78] G. Binnig, C. F. Quate, and Ch. Gerber, Phys. Rev. Lett. **56**, 930 (1986).

[79] R. J. Hamers, J. Phys. Chem. **100**, 13103 (1996).

[80] W. Ma, R. Nötzel, H.-P. Schönherr, and K. H. Ploog, Appl. Phys. Lett. **79**, 4219 (2001).

[81] S. K. Park, J. Tatebayashi, and Y. Arakawa, Physica E **21**, 279 (2004).

[82] D. B. Williams and C. B. Carter, *Transmission Electron Microscopy - A Textbook for Materials Science*, Plenum Press, New York and London, 1996, ISBN: 0-306-45324-X.

[83] A. Rosenauer, U. Fischer, D. Gerthsen, and A. Förster, Ultramicroscopy **72**, 121 (1998).

[84] R. Beanland, Ultramicroscopy **102**, 115 (2005).

[85] H. S. Djie, D.-N. Wang, B. S. Ooi, J. C. M. Hwang, X.-M. Fang, Y. Wu, J. M. Fastenau, and W. K. Liu, J. Appl. Phys. **100**, 033527 (2006).

[86] A. Rosenauer, D. Gerthsen, D. Van Dyck, M. Arzberger, G. Böhm, and G. Abstreiter, Phys. Rev. B **64**, 245334 (2001).

[87] M. De Giorgi, A. Taurino, A. Passaseo, M. Catalano, and R. Cingolani, Phys. Rev. B **63**, 245302 (2001).

[88] A. Gustafsson, M.-E. Pistol, L. Montelius, and L. Samuelson, J. Appl. Phys. **84**, 1715 (1998).

[89] H. Y. Liu, C. M. Tey, I. R. Sellers, T. J. Badcock, D. J. Mowbray, M. S. Skolnick, R. Beanland, M. Hopkinson, and A. G. Cullis, J. Appl. Phys. **98**, 083516 (2005).

[90] N. I. Cade, H. Gotoh, H. Kamada, H. Nakano, and H. Okamoto, Phys. Rev. B **73**, 115322 (2006).

[91] U. W. Pohl, K. Pötschke, A. Schliwa, F. Guffarth, D. Bimberg N. D. Zakharov, P. Werner, M. B. Lifshits, V. A. Shchukin, and D. E. Jesson, Phys. Rev. B **72**, 245332 (2005).

[92] T. Kalka, *Aufbau eines Tieftemperatur-UHV-Rastertunnelmikroskops für Ballistische-Elektronen-Emmissions-Mikroskopie*, Diploma thesis, FU Berlin, 1995.

[93] R. Timm, *Rastertunnelmikroskopie an Querschnittsflächen von Typ-II Quantentöpfen*, Diploma thesis, TU Berlin, 2002.

[94] S. K. Becker, *CM Utility*^{2}, Version 1.3, TU Berlin, Copyright 2001 AG Dähne.

[95] I. Horcas, R. Fernández, J. M. Gómez-Rodríguez, J. Colchero J. Gómez-Herrero, and A. M. Baro, Rev. Sci. Instrum. **78**, 013705 (2007).

[96] Ch. Hennig, *Rastertunnelmikroskopie an Querschnittsflächen von Quantenpunkten auf Vizinalflächen*, Diploma thesis, TU Berlin, 2002.

[97] H. Eisele, *Cross-Sectional Scanning Tunneling Microscopy of InAs/GaAs Quantum Dots*, Wissenschaft & Technik Verlag, Berlin, 2002, ISBN: 3-89685-388-0.

[98] R. Timm, *Formation, atomic structure, and electronic properties of GaSb quantum dots in GaAs*, PhD thesis, TU Berlin, 2007.

[99] M. Ternes, *Aufbau eines Rastertunnelmikroskops und Untersuchungen an Querschnittsflchen von Halbleiterstrukturen*, Diploma thesis, TU Berlin, 2001.

[100] J. P. Ibe, P. P. Bey, Jr., S. L. Brandow, R. A. Brizzolara, N. A. Burnham, D. P. DiLella, K. P. Lee, C. R. K. Marrian, and R. J. Colton, J. Vac. Sci. Technol. A **8**, 3570 (1990).

[101] S. Y. Tong, A. R. Lubinsky, B. J. Mrstik, and M. A. Van Hove, Phys. Rev. B **17**, 3303 (1978).

[102] Ph. Ebert, B. Engels, P. Richard, K. Schroeder, S. Blügel, C. Domke, M. Heinrich, and K. Urban, Phys. Rev. Lett. **77**, 2997 (1996).

[103] J.F. Zheng, J.D. Walker, M.B. Salmeron, and E.R. Weber, Phys. Rev. Lett. **72**, 2414 (1994).

[104] K.-J. Chao, C.-K. Shih, D.W. Gotthold, and B.G. Streetman, Phys. Rev. Lett. **79**, 4822 (1997).

[105] W. Barvosa-Carter, M. E. Twigg, M. J. Yang, and L. J. Whitman, Phys. Rev. B **63**, 245311 (2001).

[106] C. Domke, Ph. Ebert, M. Heinrich, and K. Urban, Phys. Rev. B **54**, 10288 (1996).

[107] Ph. Ebert, Surf. Sci. Report **33**, 121 (1999).

[108] Ph. Ebert, Appl. Phys. A **75**, 101 (2002).

[109] M. Heinrich, C. Domke, Ph. Ebert, and K. Urban, Phys. Rev. B **53**, 10894 (1996).

[110] B. Siemens, C. Domke, Ph. Ebert, and K. Urban, Phys. Rev. B **59**, 3000 (1999).

[111] O. Flebbe, H. Eisele, T. Kalka, F. Heinrichtsdorff, A. Krost, D. Bimberg, and M. Dähne-Prietsch, J. Vac. Sci. Technol. B **17**, 1639 (1999).

[112] A. Lenz, *Rastertunnelmikroskopie an Querschnittsflächen von III-V-Quantenpunkten bei speziellen Wachstumsbedingung*, Diploma thesis, TU Berlin, 2002.

[113] J. Márquez, L. Geelhaar, and K. Jacobi, Appl. Phys. Lett. **78**, 2309 (2001).

[114] M. C. Xu, Y. Temko, T. Suzuki, and K. Jacobi, J. Appl. Phys. **98**, 083525 (2005).

[115] K. Jacobi, L. Geelhaar, and J. Márquez, Appl. Phys. A **75**, 113 (2002).

[116] N. Liu, J. Tersoff, O. Baklenov, A. L. Homes, Jr., and C.-K. Shih, Phys. Rev. Lett. **84**, 334 (2000).

[117] D. M. Bruls, J. W. A. M. Vugs, P. M. Koenraad, H. W. M. Salemink, J. H. Wolter, M. Hopkinson, M. S. Skolnick, Fei Long, and S. P. A. Gill, Appl. Phys. Lett. **81**, 1708 (2002).

[118] R. Timm, H. Eisele, A. Lenz, S. K. Becker, J. Grabowski, T.-Y. Kim, L. Müller-Kirsch, K. Pötschke, U. W. Pohl, D. Bimberg, and M. Dähne, Appl. Phys. Lett. **85**, 5890 (2004).

[119] E. Lenz, *In Berechnung*, Version 146, TU Berlin, 2004-2006 AG Dähne.

[120] L. Geelhaar, *GaAs-Oberflächen im Inneren des stereografischen Dreiecks*, PhD thesis, TU Berlin, 2000.

[121] D. Leonard, M. Krishnamurthy, C. M. Reaves, S. P. Denbaars, and P. M. Petroff, Appl. Phys. Lett. **63**, 3203 (1993).

[122] J. M. Moison, F. Houzay, F. Barthe, L. Leprince, E. André, and 0. Vatel, Appl. Phys. Lett. **64**, 196 (1994).

[123] N. P. Kobayashi, T. R. Ramachandran, P. Chen, and A. Madhukar, Appl. Phys. Lett. **68**, 3299 (1996).

[124] B. A. Joyce, T. S. Jones, and J. G. Belk, J. Vac. Sci. Technol. B **16**, 2373 (1998).

[125] Y. Hasegawa, H. Kiyama, Q. K. Xue, and T. Sakurai, Appl. Phys. Lett. **72**, 2265 (1998).

[126] H. Lee, R. Lowe-Webb, W. Yang, and P. C. Sercel, Appl. Phys. Lett. **72**, 812 (1998).

[127] H. Eisele and K. Jacobi, Appl. Phys. Lett. **90**, 129902 (2007).

[128] M. Kummer, B. Vögeli, and H. von Känel, Mat. Sci. Engineering B **69**, 247 (2000).

[129] W. Sheng and J.-P. Leburton, Phys. Rev. B **63**, 161301(R) (2001).

[130] R. Heitz, O. Stier, I. Mukhametzhanov, A. Madhukar, and D. Bimberg, Phys. Rev. B **62**, 11017 (2000).

[131] H. Y. Liu, M. Hopkinson, C. N. Harrison, M. J. Steer, R. Frith, I. R. Sellers, D. J. Mowbray, and M. S. Skolnick, J. Appl. Phys. **93**, 2931 (2003).

[132] P. B. Joyce, T. J. Krzyzewski, G. R. Bell, T. S. Jones, S. Malik, D. Childs, and R. Murray, Phys. Rev. B **62**, 10891 (2000).

[133] K. Zhang, Ch. Heyn, W. Hansen, Th. Schmidt, and J. Falta, Appl. Phys. Lett. **76**, 2229 (2000).

[134] G. Costantini, A. Rastelli, C. Manzano, R. Songmuang, O. G. Schmidt, K. Kern, and H. von Känel, Appl. Phys. Lett. **85**, 5673 (2004).

[135] J. Kim, L-W. Wang, and A. Zunger, Phys. Rev. B **57**, R9408 (1998).

[136] A. Lenz, R. Timm, H. Eisele, Ch. Hennig, S. K. Becker, R. L. Sellin, U. W. Pohl, D. Bimberg, and M. Dähne, Appl. Phys. Lett. **81**, 5150 (2002).

[137] I. Kegel, T. H. Metzger, A. Lorke, J. Peisl, J. Stangl, G. Bauer, K. Nordlund, W. V. Schoenfeld, and P. M. Petroff, Phys. Rev. B **63**, 035318 (2001).

[138] P. B. Joyce, T. J. Krzyzewski, G. R. Bell, T. S. Jones, E. C. Le Ru, and R. Murray, Phys. Rev. B **64**, 235317 (2001).

[139] T. Suzuki, Y. Temko, and K. Jacobi, Phys. Rev. B **67**, 045315 (2003).

[140] P. M. Thibado, B. R. Bennett, M. E. Twigg, B. V. Shanabrook, and L. J. Whitman, J. Vac. Sci. Technol. A **14**, 885 (1996).

[141] R. Timm, J. Grabowski, H. Eisele, A. Lenz, S. K. Becker, L. Müller-Kirsch, K. Pötschke, U. W. Pohl, D. Bimberg, and M. Dähne, Physica E **26**, 231 (2005).

[142] R. Heitz, pri. communication, TU Berlin (2003).

[143] H. Kirmse, pri. communication, HU Berlin (2006-2007).

[144] R. Heitz, F. Guffarth, K. Pötschke, A. Schliwa, D. Bimberg, N. D. Zakharov, and P. Werner, Phys. Rev. B **71**, 045325 (2005).

[145] D. M. Bruls, P. M. Koenraad, H. W. M. Salemink, J. H. Wolter, M. Hopkinson, and M. S. Skolnick, Appl. Phys. Lett. **82**, 3758 (2003).

[146] J. M. García, G. Medeiros-Ribeiro, K. Schmidt, T. Ngo, J. L. Feng, A. Lorke, J. Kotthaus, and P. M. Petroff, Appl. Phys. Lett. **71**, 2014 (1997).

[147] R. Songmuang, S. Kiravittaya, and O. G. Schmidt, J. Crys. Growth **249**, 416 (2003).

[148] T. Hammerschmidt, *Growth Simulations of InAs/GaAs Quantum-Dots*, PhD thesis, TU Berlin, 2006.

[149] H. Shimizu, K. Kumada, S. Uchiyama, and A. Kasukawa, IEEE Electron. Lett. **36**, 1379 (2000).

[150] T. Matsuura, T. Miyamoto, T. Kageyama, M. Ohta, Y. Matsui, T. Furuhata, and F. Koyama, Jpn. J. Appl. Phys. **43**, L605 (2004).

[151] H. Salemink and O. Albrektsen, J. Vac. Sci. Technol. B **9**, 779 (1991).

[152] Tai-Yang Kim, *Querschnittsrastertunnelmikroskopische Untersuchung von InAs-GaAs-Quantenpunkten mit Sb-Beimischungen*, Diploma thesis, TU Berlin, 2004.

[153] R. Timm, H. Eisele, A. Lenz, T. Y. Kim, F. Streicher, K. Pötschke, U. W. Pohl, D. Bimberg, and M. Dähne, Physica E **32**, 25 (2006).

[154] B. Lita, R. S. Goldman, J. D. Phillips, and P. K. Bhattacharya, Appl. Phys. Lett. **75**, 2797 (1999).

[155] Q. Gong, P. Offermans, R. Nötzel, P. M. Koenraad, and J. H. Wolter, Appl. Phys. Lett. **85**, 5697 (2004).

[156] J. P. Silveira, J. M. Garcia, and F. Briones, J. Crys. Growth **227**, 995 (2001).

[157] T. Brown, A. Brown, and G. May, J. Vac. Sci. Technol. B **20**, 1771 (2002).

[158] K. Pötschke, PL measurements, TU Berlin (2004).

[159] A. E. Zhukov, A. R. Kovsh, N. A. Maleev, S. S. Mikhrin, V. M. Ustinov, A. F. Tsatsul'nikov, M. V. Maximov, B. V. Volovik, D. A. Bedarev, Yu. M. Shernyakov, P. S. Kop'ev, Z. I. Alferov, N .N. Ledentsov, and D. Bimberg, Appl. Phys. Lett. **75**, 1926 (1999).

[160] F. Guffarth, R. Heitz, A. Schliwa, O. Stier, N. N. Ledentsov, A. R. Kovsh, V. M. Ustinov, and D. Bimberg, Phys. Rev. B **64**, 085305 (2001).

[161] P. G. Eliseev, H. Li, A. Stintz, G. T. Liu, T. C. Newell, K. J. Malloy, and L. F. Lester, Appl. Phys. Lett. **77**, 262 (2000).

[162] Y. Qiu, P. Gogna, S. Forouhar, A. Stintz, and L. F. Lester, Appl. Phys. Lett. **79**, 3570 (2001).

[163] J. X. Chen, U. Oesterle, A. Fiore, R. P. Stanley, M. Ilegems, and T. Todaro, Appl. Phys. Lett. **79**, 3681 (2001).

[164] H. Y. Liu, M. Hopkinson, C. N. Harrison, M. J. Steer, R. Frith, I. R. Sellers, D. J. Mowbray, and M. S. Skolnick, J. Appl. Phys. **93**, 2931 (2003).

[165] R. Sellin, *Metalorganic Chemical Vapor Deposition of High-Performance GaAs-Based Quantum-Dot Lasers*, PhD thesis, TU Berlin, 2003.

[166] R. Sellin, F. Heinrichsdorff, Ch. Ribbat, M. Grundmann, U.W. Pohl, and D. Bimberg, J. Crys. Growth **221**, 581 (2000).

[167] G. S. Solomon, J. A. Trezza, A. F. Marshall, and J. S. Harris, Jr. Phys. Rev. Lett. **76**, 952 (1996).

[168] V. Holý, G. Springholz, M. Pinczolits, and G. Bauer, Phys. Rev. Lett. **83**, 356 (1999).

[169] A. Lenz, H. Eisele, R. Timm, S. K. Becker, R. L. Sellin, U. W. Pohl, D. Bimberg, and M. Dähne, Appl. Phys. Lett. **85**, 3848 (2004).

[170] H. A. McKay, R. M. Feenstra, T. Schmidtling, U. W. Pohl, and J. F. Geisz, J. Vac. Sci. Technol. B **19**, 1644 (2001).

[171] L. Ivanova, H. Eisele, A. Lenz, R. Timm, O. Schumann, L. Geelhaar, H. Riechert, and M. Dähne, to be published (2007).

[172] H. Eisele, A. Lenz, Ch. Hennig, R. Timm, M. Ternes, and M. Dähne, J. Crys. Growth **248**, 322 (2003).

[173] N. N. Ledentsov, V. A. Shchukin, M. Grundmann, N. Kirstaedter, J. Böhrer, O. Schmidt, D. Bimberg, V. M. Ustinov, A. Yu. Egorov, A. E. Zhukov, P. S. Kop'ev, S. V. Zaitsev, N. Yu. Gordeev, Zh. I. Alferov, A. I. Borovkov, A. O. Kosogov, S. S. Ruvimov, P. Werner, U. Gösele, and J. Heydenreich, Phys. Rev. B **54**, 8743 (1996).

[174] Z. R. Wasilewski, S. Fafard, and J. P. McCaffrey, J. Crys. Growth **201**, 1131 (1999).

[175] L. G. Wang, P. Kratzer, M. Scheffler, and Q. K. K. Liu, Appl. Phys. A **73**, 161 (2001).

[176] P. Offermans, P. M. Koenraad, J. H. Wolter, D. Granados, J. M. García, V. M. Fomin, V. N. Gladilin, and J. T. Devreese, Appl. Phys. Lett. **87**, 131902 (2005).

[177] R. Blossey and A. Lorke, Phys. Rev. E **65**, 021603 (2002).

[178] H. Y. Liu, pri. communication, University of Sheffield (2007).

[179] L. Ouattara, A. Mikkelsen, E. Lundgren, L. Höglund, C. Asplund, and J. Y. Andersson, J. Appl. Phys. **100**, 044320 (2006).

[180] A. Lenz, H. Eisele, R. Timm, L. Ivanova, H.-Y. Liu, M. Hopkinson, U. W. Pohl, and M. Dähne, Physica E , accepted.

[181] J. He, B. Xu, Z. G. Wang, S. C. Qu, F. Q. Liu, and T. W. Zhu, Physica E **19**, 292 (2003).

[182] M. Hopkinson, pri. communication, University of Sheffield (2007).

[183] D. Gammon, E. S. Snow, B. V. Shanabrook, D. S. Katzer, and D. Park, Phys. Rev. Lett. **76**, 3005 (1996).

[184] K. Matsuda, T. Saiki, S. Nomura, M. Mihara, Y. Aoyagi, S. Nair, and T. Takagahara, Phys. Rev. Lett. **91**, 177401 (2003).

[185] S. Kiravittaya, R. Songmuang, N. Y. Jin-Phillipp, S. Panyakeow, and O. G. Schmidt, J. Crys. Growth **251**, 258 (2003).

[186] A. Rastelli, S. Kiravittaya, L. Wand, C. Bauer, and O. G. Schmidt, Physica E **32**, 29 (2006).

[187] T. C. G. Reusch, M. Wenderoth, A. J. Heinrich, K. J. Engel, N. Quaas, K. Sauthoff, R. G. Ulbrich, E. R. Weber, K. Uchida, and W. Wegscheider, Appl. Phys. Lett. **76**, 3882 (2000).

[188] A. Lenz, R. Timm, H. Eisele, L. Ivanova, D. Martin, V. Voßebürger, A. Rastelli, O. G. Schmidt, and M. Dähne, phys. stat. sol. (b) **243**, 3976 (2006).

[189] V. Mlinar, A. Schliwa, D. Bimberg, and F. M. Peeters, Phys. Rev. B **75**, 205308 (2007).